MINIMUM QUANTITY LUBRICATION GRINDING USING NANOFLUIDS

by

Bin Shen

A dissertation submitted in partial fulfillment
of the requirements for the degree of
Doctor of Philosophy
(Mechanical Engineering)
in The University Of Michigan
2008

Doctoral Committee:

Professor Albert J. Shih, Chair
Assistant Professor Kevin P. Pipe
Assistant Professor Max Shtein
Guoxian Xiao, General Motors Research

ACKNOWLEDGEMENT

First of all, I would like to thank my academic advisor, Prof. Albert J. Shih, for his guidance and help in my PhD program. I also want to thank my committee members Prof. Kevin Pipe, Prof. Max Shtein and Dr. Guoxian Xiao, for their valuable comments and careful review of this dissertation.

My research was primarily sponsored by NSF and General Motors. Support from Saint-Gobain and AMCOL Corporation are greatly appreciated. I am also grateful to Prof. Stephen Malkin and Alan Rakouskas of University of Massachusetts Amherst, Dr. Changsheng Guo of United Technologies Research Center, Dr. Simon Tung and Dr. Jean Dasch of General Motors, and Dr. Mike Hitchiner of Saint-Gobain. I especially thank my friends at The University of Michigan for their supports and encouragements.

Finally, I would like to express my greatest gratitude to my families, especially my parents Gencai Shen and Jinfeng Yang for their selfless love and support.

TABLE OF CONTENTS

LIST OF FIGURES

LIST OF TABLES

LIST OF APPENDICES

CHAPTER 1

INTRODUCTION

Nanofluid is a new class of fluids engineered by dispersing nanometer-size solid particles in base fluids to increase heat transfer and tribological properties. This research studied the synthesis, characterization of nanofluids, and its application in minimum quantity lubrication (MQL) grinding. MQL is to supply a minute quantity of cooling lubricant medium to the tool-workpiece interface, which can tremendously reduce the applied amount of cutting fluid. The goal of this research is to develop a production-feasible and environmentally benign grinding process. Cutting fluids, grinding wheels, and comprehensive understanding of the thermal aspects in grinding are three key technical areas that can enable the success of MQL grinding.

1.1. Nanofluids

Nanofluid is a new class of fluids engineered by dispersing nanometer-size solid particles into base fluids such as water, ethylene glycol, engine oil, cutting fluids, etc.

Research has shown that the thermal conductivity and the convection heat transfer coefficient of the fluid can be largely enhanced by the suspended nanoparticles (Choi, 1995; Xuan and Roetzel, 2000; Choi et al., 2001a, 2001b; Keblinski et al., 2002; Xie et al., 2003; Xuan and Li, 2003; Wen and Ding 2004a; Lockwood et al., 2005). Recently, tribology research shows that lubricating oils with nanoparticle additives (MoS2, CuO, TiO2, Diamond, etc.) exhibit improved load-carrying capacity, anti-wear and friction-reduction properties (Xu et al., 1996; Wu et al., 2006; and Verma et al., 2007). These features make the nanofluid very attractive in some cooling and/or lubricating application in many industries including manufacturing, transportation, energy, and electronics, etc.

1.2. Minimum Quantity Lubrication (MQL)

Minimum Quantity Lubrication (MQL) refers to the use of a precision dispenser to supply a miniscule amount of cutting fluid to the tool-workpiece interface – typically at a flow rate of 50 to 500 ml/hour –which is about three to four orders of magnitude lower than the amount commonly used in a flood cooling condition (Autret et al. 2003).

MQL has been widely studied in many machining processes such as drilling (Braga et al., 2002; Filipovic and Stephenson, 2006; Davim et al., 2006; Heinemann et al., 2006), milling (Rahman et al., 2001, 2002; Lopez de Lacalle et al., 2006; Su et al., 2006; Liao and Lin, 2007), and turning (Wakabayashi et al., 1998; Dhar et al., 2006; Davim et al., 2007; Kamata and Obikawa, 2007; Autret and Liang 2003). However, MQL grinding is still a relatively new research area, and only a few researchers have studied MQL grinding (Baheti et al., 1998; Hafenbraedl and Malkin, 2000; Silva et al., 2005).

The results of these studies showed that with a proper selection of the MQL system and the cutting parameters, it is possible for MQL machining to obtain performances similar to flood lubricated conditions, in terms of lubricity, tool life, and surface finish.

1.3. Heat Transfer in Grinding

The grinding process generates an extremely high input of energy per unit volume of material removed. Virtually all this energy is converted to heat, which can cause high temperatures and thermal damage to the workpiece such as workpiece burn, phase transformations, undesirable residual tensile stresses, cracks, reduced fatigue strength, and thermal distortion and inaccuracies (Malkin, 1989). Numerous studies have been reported on both the theoretical and experimental aspects of heat transfer in grinding. Early research concentrated on predicting workpiece surface temperatures in dry grinding in the absence of significant convective heat transfer (Outwater and Shaw, 1952; Hahn, 1956; Takazawa, 1966; Malkin and Anderson, 1974). Subsequent investigations have provided a detailed understanding of heat transfer to the workpiece, abrasive grains, grinding fluid, and the chips (DesRuisseaux and Zerkle, 1970; Lavine, 1988; Demetriou and Lavine, 2000; Shaw, 1990, Ju et al., 1998; Guo and Malkin, 1996a; 1996b). Thermal models have been developed to estimate the workpiece surface temperature, heat flux distribution in the grinding zone, fraction of energy entering the workpiece, and convective heat transfer coefficient for cooling on the workpiece surface. Experimental investigations of heat transfer in grinding require accurate temperature measurements. Methods for temperature measurement in grinding include thermal imaging (Sakagami et

al., 1990; Hwang et al., 2004), optical fiber (Ueda, 1986; Ueda and Sugita, 1992; Curry et al., 2003), foil/workpiece (single pole) thermocouple (Rowe et al., 1996; Xu et al., 2003; Huang and Xu, 2004; Batako et al., 2005; Lefebvre et al., 2006), and embedded (double pole) thermocouple (Littman and Wulff, 1995; Kohli et al., 1995; Guo et al., 1999; Xu and Malkin, 2001; Upadhyaya and Malkin, 2004; Kim et al., 2006).

1.4. Research Motivations and Goals

Grinding is a precision machining process which is widely used in the manufacture of components requiring fine tolerances and smooth finishes. Cutting fluids are used in grinding for a variety of reasons such as improving wheel life, reducing workpiece thermal deformation, improving surface finish and flushing away chips. Large fluid delivery and cooling systems are evident in production plants. Grinding is recognized as one of the most environmentally unfriendly manufacturing processes. An extensive amount of mist is generated during grinding, and the problem is exacerbated by the use of high wheel speeds. From measurements of the mist concentration and droplet size distribution on the shop floor for grinding reported by Chen et al. (2002a, 2002b), it was concluded that the mist generation rate in grinding is often an order of magnitude higher than that in turning. Millions of workers are engaged in daily manufacturing operations worldwide. However, the health hazards to machine operators and other nearby workers who breathe in this hazardous mist are often overlooked. The inherent high cost of disposal or recycling of the grinding fluid is often accepted as a necessary cost of doing business. As environmental regulations get stricter, the cost of disposal or recycling continues to go up. The Occupational Safety and Health Administration

(OHSA) regulations of mist/aerosol in manufacturing plants are 5 mg/m^3 for an 8-hour time weighted average (TWA) for mineral oil mist and 15 mg/m^3 (8-hour TWA) for Particulates Not Otherwise Classified (PNOC)[1]. The recommended exposure limits by the National Institute for Occupational Safety and Health (NIOSH) is an order of magnitude lower, 0.5 mg/m^3 for the total particulate mass. There is significant pressure to adopt this stricter standard into legislation, so factory mist generation must be reduced. There are also costs involved with workpiece rust and corrosion, skin diseases, and maintenance.

Government regulation, environmental protection, public awareness, and the need for cost-reduction have all promoted the development of new environmentally conscious machining processes. The main obstacle to replace or eliminate cutting fluids is that the energy generated in the machining process and dissipated as heat causes elevated temperatures, thermal damage, and dimensional inaccuracies. Cutting fluids are a critical factor in controlling these undesirable effects, mainly by providing lubrication and cooling. Lubrication reduces the machining power and the associated heat generation, while also enhancing surface quality and reducing wheel wear. Cooling by the fluid removes heat from the tool and the workpiece.

One alternative to large cutting fluids practice is the dry machining, without using any cutting fluid. Research on dry machining was mainly concerned with the development of appropriate tools and coatings (Shen, 1996; Klocke, 1997; Machado et al., 1997; Nouari et al., 2004; Kobayashi et al., 2005; Reddy and Rao, 2006; Su et al., 2006). Although dry machining is possible in some situations, there are still lots of issues

[1] http://www.osha.gov/SLTC/metalworkingfluids/metalworkingfluids_manual.html

regarding lubricity, tool life, thermal damage of workpiece, etc (Sun et al., 2006; Davim et al., 2006; Heinemann et al., 2006; Itoigawa et al., 2006). Therefore, Minimum Quantity Lubrication (MQL) was proposed. The use of MQL is of great significance in conjunction between large cutting fluids application and dry machining. It can reduce the amount of frictional heat generation and provide some cooling in the tool-workpiece interface and hence keep the workpiece temperatures lower than those in a completely dry machining. Another characteristic of this technology is that when properly applied, both parts and chips remain dry and are easier to handle (Itoigawa et al., 2006).

Both General Motors Powertrain Division and Ford Advanced Manufacturing Technical Development (AMTD) are leading the effort to implement MQL processes in production. The most common high volume production application for MQL is cross and oil hole drilling on steel crankshafts (Filipovic and Stephenson, 2006). The total cost-savings due to the reduction of fluid use and disposal, while maintaining the same level of productivity and quality, affirm that both the environment and cost/productivity targets can be met in well-developed MQL machining processes.

Since grinding is an abrasive process, it generates extremely high energy input at the tool-workpiece interface. The application of MQL in grinding is much more challenging than in any other cutting processes, and only a few researchers have studied MQL grinding so far. In previous research at University of Massachusetts, the performance of MQL grinding using non-hazardous ester oil was evaluated relative to conventional 5 vol% soluble oil as well as dry grinding for straight surface grinding and internal cylindrical grinding in terms of specific energy, surface roughness, wheel wear, and cooling (Baheti et al., 1998; Hafenbraedl and Malkin, 2000). Experimental results

showed that MQL provided effective lubrication but insufficient workpiece cooling with conventional abrasive wheels. MQL grinding has also been studied in Europe with similar conclusions (Brinksmeier et al., 1997) regarding workpiece cooling.

On the other hand, the recent development of nanofluids provides alterative cutting fluids which can be used in MQL grinding. The advanced heat transfer and tribological properties of these nanofluids can provide better cooling and lubricating in the MQL grinding process, and make it production-feasible.

In addition, CBN grinding wheel is considered for MQL grinding because CBN grains have very high thermal conductivity, which can enhance heat conduction away from the grinding zone to the wheel (Lavine et al., 1989; Upadhyaya and Malkin, 2004), and therefore can prevent the thermal damage to the workpiece.

The goal of this research is to develop a practical and environmentally benign grinding process by addressing the following four areas: (1) synthesis and characterization of new nanofluids, (2) application of nanofluids in MQL grinding using conventional abrasives (aluminum oxide) wheels and superabrasives (CBN) wheels, (3) thermal analysis of MQL grinding, and (4) heat transfer modeling of the grinding process based on the Finite Difference Method.

1.5. Outline

Chapter 2 presents formation and characterization of nanofluids. The methods of nanofluids synthesis were introduced and several different types of nanofluids were formulated. The transient hot wire method was used to measure the thermal conductivity of nanofluids, and the convection heat transfer coefficient of nanofluid passing through a

microchannel was also investigated.

Chapter 3 presents the experimental work of MQL grinding using conventional abrasive wheels. Both water based and oil based nanofluids were employed in MQL grinding and the performance was evaluated in terms of grinding force, G-ratio, and surface roughness, etc.

Chapter 4 focuses on heat transfer in grinding. A new thermocouple fixating method for grinding temperature measurement was proposed and further utilized to experimentally investigate the energy partition for grinding under dry, wet, and MQL conditions. Thermal analysis of MQL grinding using superabrasives (CBN) wheels was also studied.

Chapter 5 introduced a Finite Difference Method (FDM) based grinding thermal model. The model was developed to better understand the heat transfer problems in grinding. The effects of workpiece dimension, feed rate, and various cooling conditions were investigated using the FDM heat transfer model. It was further applied in the grinding experiments to estimate the energy partition and the convection heat transfer coefficient.

The conclusions and recommendations for future work are presented in Chapter 6.

CHAPTER 2

NANOFLUIDS SYNTHESIS AND CHARACTERIZATION

Nanofluid is a new class of fluids engineered by dispersing nanometer-size solid particles into base fluids such as water, ethylene glycol, lubrication oils, and etc. Nanofluids containing Al_2O_3 nanoparticles and multi-wall carbon nanotubes were synthesized by two-step physical process (Choi et al., 2001a). Diamond nanofluids and high volume fraction nanofluids were acquired from the sponsor companies.

The transient hot wire method was used to measure the thermal conductivity of nanofluids, and high thermal conductivity enhancement of 61% was observed for ZnO nanofluids at 15 vol%.

The convection heat transfer coefficient of nanofluid was also investigated. The nanofluids showed higher Nusselt number than its base fluid at the same Reynolds number. However, there is no significant difference between the nanofluids and the base fluids in terms of convection heat transfer coefficient vs. flow rate. The increase in Nusselt number of nanofluids is mainly due to the higher viscosity, compared to the base fluid.

2.1. Introduction

2.1.1. Nanofluid for Cooling Applications

Heat transfer fluids play an important role for cooling applications in many industries including manufacturing, transportation, energy, and electronics, etc. Developments in new technologies such as highly integrated microelectronic devices, higher power output engines, and reduction in applied cutting fluids continuously increase the thermal loads, which requires advances in cooling capacity. Therefore, there is an urgent need for new and innovative heat transfer fluids to achieve better cooling performance.

Generally, conventional heat transfer fluids have poor heat transfer properties compared to solids. As shown in Table 2.1, most solids have orders of magnitude larger thermal conductivities than those of conventional heat transfer fluids. Therefore, fluids containing suspended solid particles are expected to display significant enhancement in thermal conductivities relative to conventional heat transfer fluids.

Numerous theoretical and experimental studies of the effective thermal conductivity of fluids containing particles have been conducted since Maxwell's theoretical work was published more than 100 years ago. However, these studies were confined to dispersions containing millimeter- or micrometer-sized particles. In developing advanced fluids for industrial applications, it was identified that millimeter- or micrometer-sized sized particles have severe clogging and abrasive problems.

With the development of nanopowder synthesizing techniques, it was proposed that nanometer sized solid particles can be uniformly and stably suspended in industrial heat transfer fluids such as water, ethylene glycol, or engine oil to produce a new class of

engineered fluids with high thermal conductivity. Choi (1995) coined the term "nanofluids" for this new class of engineered heat transfer fluids. Since nanoparticles are small enough that they are expected to behave like molecules of liquid, nanofluids will not clog flow passages, but can improve the thermal properties.

Table 2.1. Thermal conductivity of matters (data summarized from Incropera and DeWitt, 2001)

Material	Thermal conductivity (W/m-K) @ 300K
Metallic solids	
Copper	401
Aluminum	237
Titanium	22
Nonmetallic solids	
Diamond	2300
Silicon	148
Aluminum Oxide	36
Conventional heat transfer fluids	
Water	0.613
Ethylene Glycol	0.252
Engine Oil	0.145

2.1.1.1. Metallic nanofluids vs. non-metallic nanofluids

Nanofluids can be generally classified into two categories, i.e. metallic nanofluids and non-metallic nanofluids (Eastman et al., 2004). Metallic nanofluids often refer to those containing metallic nanoparticles such as copper (Cu), ferrum (Fe), gold (Au) and silver (Ag), while nanofluids containing non-metallic nanoparticles such as aluminum oxide (Al_2O_3), copper oxide (CuO) and silicon carbide (SiC) are often considered as non-metallic nanofluids.

2.1.1.2. Thermal conductivity of nanofluids

Conventional heat conduction models for solid-liquid mixtures have long been established such as Maxwell model (Maxwell, 1904), Hamilton–Crosser model (Hamilton and Crosser, 1962) and Jeffrey model (Jeffrey, 1973). However, these conventional heat conduction models were confined to dispersions containing millimeter- or micrometer-sized particles. When applying to nanofluids, they usually underestimate the thermal conductivity (Wang et al., 1999; Choi, et al., 2001a; Jang and Choi, 2004).

Thus, thermal conductivity of nanofluids has been widely studied since 1993 (Masuda et al., 1993), although the term "nanofluids" was later on coined by Choi (1995). Transient hot wire method is well developed to experimentally measure the thermal conductivity of nanofluids (Nagasaka and Nagashima, 1981). Table 2.2 summaries the literature review for thermal conductivity of nanofluids.

Metallic nanofluids have been widely studied. Choi et al. (2001a) found that the effective thermal conductivity of ethylene glycol was improved by up to 40% through the dispersion of 0.3 vol% Cu nanoparticles of 10 nm mean diameter, while Xuan and Li. (2000) demonstrated that the effective thermal conductivity of water was increased by up to 78% with 7.5 vol% Cu nanoparticles of 100 nm mean diameter. Hong et al. (2005) reported that the thermal conductivity of Fe nanofluids is increased nonlinearly up to 18% as the volume fraction of particles is increased up to 0.55 vol%. Patel et al. (2003) studied behavior of Au and Ag nanoparticles dispersed in water and found that the water soluble Au nanoparticles, 10–20 nm in mean diameter, made with citrate stabilization showed thermal conductivity enhancement of 5–21% in the temperature range of 30–60ºC at a loading of 0.026 vol%, however, comparatively lower thermal conductivity

enhancement was observed for larger diameter Ag particles for higher loading (average diameter of 60-80 nm).

Non-metallic nanofluids such as Al_2O_3, CuO, SiC, TiO_2 and carbon nanotubes also have been studied. The early research work by Masuda et al. (1993) reported 30% increases in the thermal conductivity of water with the addition of 4.3 vol% Al_2O_3 nanoparticles (average diameter of 13 nm). A subsequent study by Lee et al. (1999), however, observed only a 15% enhancement in thermal conductivity at the same nanoparticle loading (average diameter of 33 nm). Xie et al. (2002a) found an intermediate result, that is, the thermal conductivity of water is enhanced by approximately 21% by a nanoparticle loading of 5 vol% (average diameter of 68 nm). These differences in behavior were probably attributed to differences in average particle size in the samples. Nanofluids consisting of CuO nanoparticles dispersed in water and ethylene glycol seem to have larger enhancements in thermal conductivity than those containing Al_2O_3 nanoparticles (Lee et al., 1999). The early research by Eastman et al. (1997) showed that increase in thermal conductivity of approximately 60% can be obtained for the nanofluid consisting of water and 5 vol% CuO nanoparticles with average grain size of 36 nm. While Lee et al. (1999) observed only a modest improvement of nanofluids containing CuO compared with those containing Al_2O_3, Zhou and Wang (2002) observed a 17% increase in thermal conductivity for a loading of only 0.4 vol% CuO nanoparticles in water. Xie et al. (2002b) studied SiC (average diameter of 26 nm) in water suspension and reported that the thermal conductivity can be increased by about 15.8% at 4.2 vol%. Murshed et al. (2005) showed that the measured thermal conductivity for water based TiO_2 nanofluids (average diameter of 15 nm) has a

maximum enhancement 30% for 5 vol% of particles.

Carbon nanotube nanofluids, is of special interests to researchers because of the novel properties of carbon nanotubes -extraordinary strength, unique electrical properties, and efficient conductors of heat. Carbon nanotubes (CNTs) are fullerene-related structures that consist of either a grapheme cylinder (the so-called single-wall carbon nanotubes, SWCNTs) or a number of concentric cylinders (the so-called multiwalled carbon nanotubes, MWCNTs) (Wen and Ding, 2004b). Choi et al. (2001b) measured the effective thermal conductivity of MWCNTs dispersed in synthetic (poly-α-olefin) oil and reported the enhancement up to a 150% in conductivity at approximately 1 vol% CNT, which is by far the highest thermal conductivity enhancement ever achieved in a liquid (Lockwood et al., 2005). However, this huge enhancement was not observed by Xie et al. (2003) for water/ ethylene glycol/decene based MWCNTs nanofluids, nor by Assael et al. (2004) for water based MWCNTs nanofluids. The maximum thermal conductivity enhancements observed by Xie et al. (2003) are 19.6%, 12.7%, and 7.0% for MWCNTs suspension at 1.0 vol% in decene, ethylene glycol, and water, respectively, and that observed by Assael et al. (2004) was 38% for MWCNTs suspension at 0.6 vol% in water.

As shown in Table 2.2, the reported measurement results are not very consistent. This is probably because different researchers may have different experimental procedure and there is uncertainty in the thermal conductivity measurement using hot wire method.

2.1.1.3. Particle size dependent thermal conductivity of nanofluids

There has not been a systematic experimental investigation of size-dependent conductivity reported (Jang and Choi, 2004). However, Wang et al. (1999) compared

their experimental data with those of other investigators, and concluded it is possible that the thermal conductivity of nanoparticle fluid mixtures increases with the decreasing particle size. How the particle size affect the thermal conductivity of nanofluids will be studied in our research.

Table 2.2. Summary of literature review for thermal conductivity of nanofluids

	Particle	Base fluid	Average particle size	Volume fraction	Thermal conductivity enhancement	Reference
Metallic nanofluids	Cu	Ethylene glycol	10 nm	0.3%	40%	Choi et al. (2001a)
	Cu	Water	100 nm	7.5%	78%	Xuan and Li (2000)
	Fe	Ethylene glycol	10 nm	0.55%	18%	Hong et al. (2005)
	Au	Water	10–20 nm	0.026%	21%	Patel et al. (2003)
	Ag	Water	60-80 nm	0.001%	17%	Patel et al. (2003)
Non-metallic nanofluids	Al_2O_3	Water	13 nm	4.3%	30%	Masuda et al. (1993)
	Al_2O_3	Water	33 nm	4.3%	15%	Lee et al. (1999)
	Al_2O_3	Water	68 nm	5%	21%	Xie et al. (2002a)
	CuO	Water	36 nm	5%	60%	Eastman et al. (1997)
	CuO	Water	36 nm	3.4%	12%	Lee et al. (1999)
	CuO	Water	50 nm	0.4%	17%	Zhou and Wang (2002)
	SiC	Water	26 nm	4.2%	16%	Xie et al. (2002b)
	TiO_2	Water	15 nm	5%	30%	Murshed et al. (2005)
	MWCNT(1)	Synthetic oil	25 nm in diameter 50 μm in length	1%	150%	Choi et al. (2001b)
	MWCNT	Decene/ Ethylene glycol/ Water	15 nm in diameter 30 μm in length	1%	20%/13%/7%	Xie et al. (2003)
	MWCNT	Water	100 nm in diameter 70 μm in length	0.6%	38%	Assael et al. (2004)

(1) MWCNT: multi-walled carbon nanotube

2.1.1.4. Temperature dependent thermal conductivity of nanofluids

Das et al. (2003) studied Al_2O_3 nanoparticles in water and showed the temperature dependent behavior of nanofluids — an increase of enhancement characteristics with temperature, which indicates that nanofluids could be particularly attractive for applications at elevated temperatures. The experimental data from my colleague White (2006) also showed the temperature dependent thermal conductivity of nanofluids, as shown in Figure 2.1. For water-based Al_2O_3 nanofluids with 1–4 vol% of particles, the thermal conductivity increases with increasing temperature.

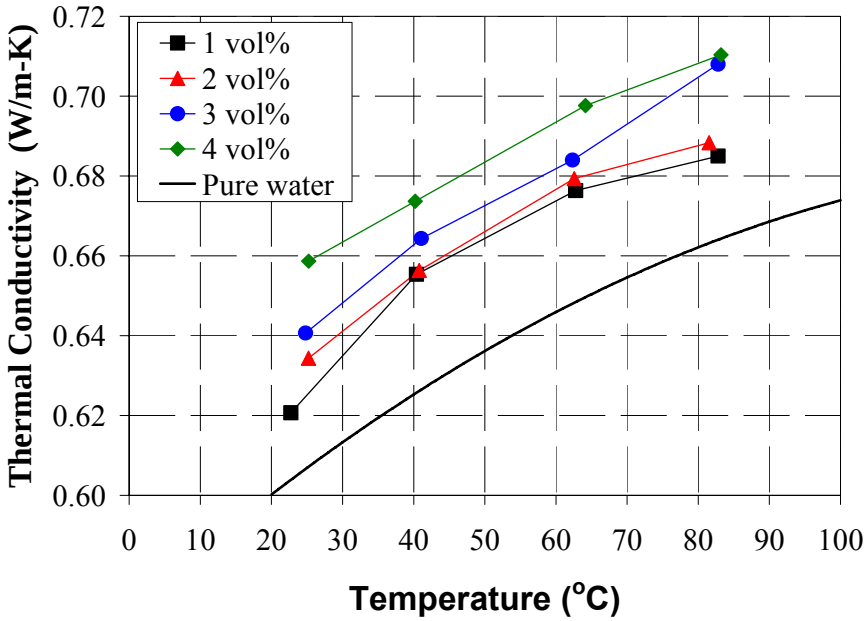

Figure 2.1. Temperature dependent thermal conductivity of Al_2O_3 nanofluids (White, 2006)

2.1.1.5. Convection heat transfer performance of nanofluids

Some researchers have investigated the heat transfer coefficients of nanofluids in convective flows (Pak and Cho, 1998; Wen and Ding, 2004a ; Xuan and Roetzel, 2000; Xuan and Li, 2000; 2003). These studies showed that nanofluids exhibited higher heat

transfer coefficient than base fluids, and the Nusselt number of nanofluids increased with increasing volume fraction of the suspended nanoparticles and the Reynolds number.

Nanofluids are multicomponent systems, and the morphology and orientation of the dispersed solids is complex (Yang et al., 2005). Experimental data have shown that both classical correlations, Shah equation (for laminar flows) and Dittus–Boelter equation (for turbulent flows) fail to predict convection heat transfer behavior of nanofluids (Wen and Ding, 2004a ; Xuan and Li, 2003). Currently, there are very few correlations developed for convection heat transfer coefficients of nanofluids (Xuan and Li, 2000; 2003).

Wen and Ding (2004a) studied convective heat transfer of nanofluids made of Al_2O_3 nanoparticles and water in the laminar flow regime, and showed that for nanofluids containing 1.6 vol% Al_2O_3 nanoparticles the local heat transfer coefficient was increased by 15 – 45% (depending on the distance from entrance region). Xuan and Li (2000; 2003) measured the convective heat transfer coefficient of nanofluids for turbulent flow and found that compared with water, the Nusselt number was increased more than 39% for the nanofluids with 2.0 vol% of Cu nanoparticles.

2.1.2. Nanofluid for Lubrication Application

On the other hand, as we know, solid lubricants are useful for conditions when conventional liquid lubricants are inadequate such as high temperature and extreme contact pressures. Their lubricating properties are attributed to a layered structure on the molecular level with weak bonding between layers. Such layers are able to slide relative to each other with minimal applied force, thus giving them their low friction properties.

Graphite and molybdenum disulfide (MoS2) are the predominant materials used as solid lubricant. Other useful solid lubricants include boron nitride, tungsten disulfide, polytetrafluorethylene (PTFE), etc, as listed in Table 2.3.

To improve the tribological properties of lubricating oils by dispersing nanoparticles, especially nanoparticulate solid lubricants, becomes of interest to people. Recent research has shown that lubricating oils with nanoparticle additives exhibit improved load-carrying capacity, anti-wear and friction-reduction properties. Xu et al. (1996) investigated tribological properties of the two-phase lubricant of paraffin oil and diamond nanoparticles, and the results showed that, under boundary lubricating conditions, this kind of two-phase lubricant possesses excellent load-carrying capacity, anti-wear and friction-reduction properties. According to Verma et al. (2007), MoS_2 in its nanoparticulate form has exceptional tribological properties, which can reduce friction under extreme pressure conditions. Wu et al. (2006) examined the tribological properties of lubricating oils with CuO, TiO2, and diamond nanoparticles additives. The experimental results show that nanoparticles, especially CuO, added to standard oils exhibit good friction-reduction and anti-wear properties.

Table 2.3. Solid lubricant [1]

Solid Lubricant	Formula	Temperature resistance (oxidizing atmosphere) [2]
Graphite	C	450 ºC
Molybdenum disulfide	MoS_2	400 ºC
Boron nitride	BN	1200 ºC
Tungsten disulfide	WS_2	450 ºC
PTFE	--	260 ºC

[1]Reference: http://www.tribology-abc.com/sub15.htm

[2]Temperature resistance is even higher in reducing/non-oxidizing environments (for example, MoS_2 up to 1100°C)

2.2. Nanofluids Synthesis

2.2.1. Overview

There are three ways to fabricate nanofluids, two-step physical process (Choi et al., 2001a), one-step physical process (Choi et al., 2001a; Choi and Eastman, 2001), and one-step chemical process (Zhu et al., 2004).

2.2.1.1. Two-step physical process

Nanoparticles are first produced as a dry powder, typically by inert gas–condensation, which involves the vaporization of a source material in a vacuum chamber and subsequent condensation of the vapor into nanoparticles via collisions with a controlled pressure of an inert gas such as helium. The resulting nanoparticles are then dispersed into a fluid in a second processing step. An advantage of this technique in terms of eventual commercialization of nanofluids is that the inert-gas condensation technique has already been scaled up to economically produce tonnage quantities of nanopowders (Wagener and Gunther, 1999).

2.2.1.2. One-step physical process

This technique synthesizes nanoparticles and disperses them into a fluid in a single step. It was originally used to prepare extremely fine particles of Ag by vacuum evaporation onto a running oil substrate, which was developed by Yatsuya and coworkers (Yatsuya et al., 1978) and later improved by Wagener and coworkers (Wagener et al., 1997; Wagener and Gunther, 1999). Choi and Eastman (2001) used this technology to

produce nanofluids. As shown in Figure 2.2 (Choi and Eastman, 2001), the technique involves vaporization of a source material under vacuum conditions, and condensation of the vapor occurs via contact between the vapor and a flowing liquid. Nanoparticle agglomeration is minimized by flowing the liquid continuously, which results in good dispersion. However, the one-step physical process is very expensive and at present the volume of nanofluids that can be produced via this direct-evaporation technique is much more limited than with two-step physical process because of the limited space in the vacuum chamber (Eastman et al., 2004).

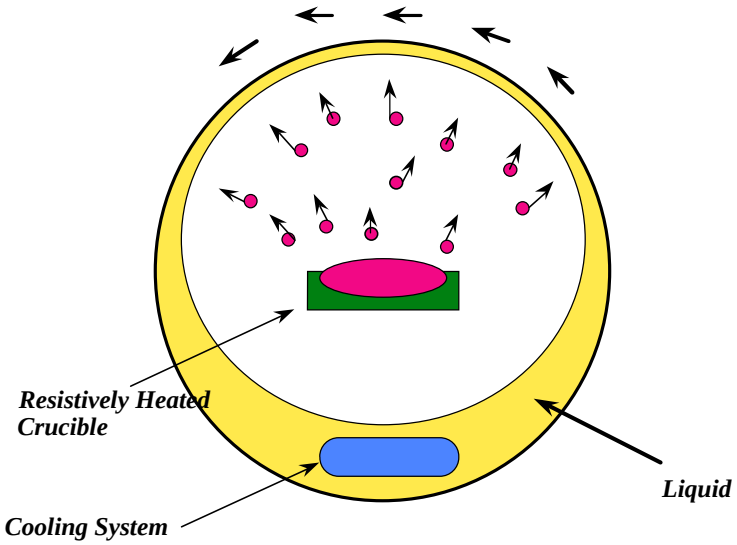

Figure 2.2. Schematic drawing of the one-step physical process (Choi and Eastman, 2001).

2.2.1.3. One-step chemical process

Zhu et al. (2004) developed a one-step chemical process for producing stable Cu in ethylene glycol nanofluids by reducing copper sulfate pentahydrate ($CuSO_4 \cdot 5H_2O$) with sodium hypophosphite ($NaH_2PO_2 \cdot H_2O$) in ethylene glycol under microwave

irradiation. The thermal conductivity enhancement approaches that of the Cu nanofluids prepared by a one-step physical method. It is found to be a fast, efficient one-step chemical method to prepare Cu nanofluids. However, this method is still in the research stage and the types of nanofluids it can produce are limited. Thus, we will not use one-step chemical process to produce nanofluids in our research.

2.2.2. Preparation of Nanofluids

Two-step physical process (Choi et al., 2001) has been adopted to synthesize Al_2O_3 and CNT nanofluids as it is the cheapest and easiest process. Some other nanofluids were acquired from sponsor companies. The material used for nanofluids synthesis is listed in Table 2.4, along with their thermal conductivity properties.

Table 2.4. List of materials of interest to nanofluids synthesis

Material	Thermal conductivity (W/m-K)	Reference
Aluminum oxide (Al_2O_3)	36	Incropera and DeWitt (2001)
Carbon nanotube (CNT)	3000	Che et al. (2000)
Diamond (C)	2300	Incropera and DeWitt (2001)
Zinc oxide (ZnO)	100	Florescu et al. (2000))

2.2.2.1. Aluminum oxide nanofluids

Two sample Al_2O_3 dry powders with mean diameter of 30 nm and 40 nm were provided by Nanotechnologies, Inc. These Al_2O_3 dry powders can be directly dispersed into water without surfactant. The Al_2O_3 nanofluids with different volume fractions from 1% to 4% were prepared and all the mixtures remain stable for weeks.

2.2.2.2. Carbon nanotube nanofluids

Four multi-wall carbon nanotubes (MWCNTs) samples were purchased from Shenzhen Nanotech Port Co., China. The speciation of the MWCNTs is listed in Table 2.5.

Table 2.5. Specification of multi-wall carbon nanotubes

Multi-wall carbon nanotubes	Main range of external diameter	Length
L-MWCNT-1020	10-20 nm	5-15 μm
S-MWCNT-1020	10-20 nm	1-2 μm
L-MWCNT-60100	60-100 nm	5-15 μm
S-MWCNT-60100	60-100 nm	1-2 μm

Carbon nanotubes (CNTs) as produced are usually entangled and not ready to be dispersed into fluids. Therefore, chemical surfactant is needed to disperse CNTs. With surfactant Sodium Dodecyl Sulfate (SDS) along with ultrosonic bathing, multi-wall carbon nanotubes are being able to be dispersed in distilled water or ethylene glycol. CNTs nanofluids with different volume fractions from 0.1% to 1% were prepared and all the mixtures remain stable for weeks.

2.2.2.3. Diamond nanofluids

Two samples of diamond nanofluid were directly provided by Saint-Gobain. One of them contains 100 nm mono-crystalline diamonds with no coating (Diamond nanofluid #1) and the other contains 200 nm carbon outer coated diamonds (Diamond nanofluid #2). Both samples have 1.5% volume fraction of diamonds. The fluid appears grey and remains stable for weeks.

2.2.2.4. High volume fraction nanofluids

Six samples of water based nanofluid with high volume fraction were provided by Nanophase Technologies (Romeoville, Illinois), as listed in Table 2.6. Three of the samples contain Al_2O_3 nanoparticles with average particle sizes of 20, 46 and 80nm. The other three contain ZnO nanoparticles with average particle sizes of 20, 40 and 60nm. The stable high volume fraction dispersions were obtained by the addition of chemical dispersants which is not disclosed by the company. As shown in the table, the volume fraction of nanofluids ranges from 10.6% to 22.1%. These concentrations are significantly higher than those of nanofluids studied in previous literature.

Table 2.6. List of nanofluids provided by Nanophase

Molecular formulation	Particle size	Volume fraction
Al_2O_3	20 nm	10.6%
	46 nm	21.7%
	80 nm	22.1%
ZnO	20 nm	10.9%
	40 nm	11.0%
	60 nm	15.0%

2.3. Thermal Conductivity Measurements

The thermal conductivity of nanofluids were measured using transient hot wire method, as described in Appendix A.1 in detail.

2.3.1. Aluminum Oxide Nanofluids

Al_2O_3 Al_2O_3fraction from 1% to 4% were prepared using two-step physical process as described in Chapter 2. The thermal conductivity of these Al_2O_3 nanofluids

were measured by long wire probe and the results are presented in Figure 2.3 along with some literature data (Lee et al., 1999; Xie et al., 2002; Wen and Ding, 2004a). In these literatures, Al_2O_3 nanofluids are all produced by two-step physical process, but the size of Al_2O_3 nanoparticle being studied is a little different.

As shown in Figure 2.3 the thermal conductivity enhancement increases with increasing volume fraction of Al_2O_3 nanoparticles. However, the size effect on the thermal conductivity is not conclusive here. This is because different researchers may have different experimental procedure and even though all the Al_2O_3 nanofluids are prepared by two-step physical process, the efficiency of dispersion could still be different, which results in the variation of thermal conductibility.

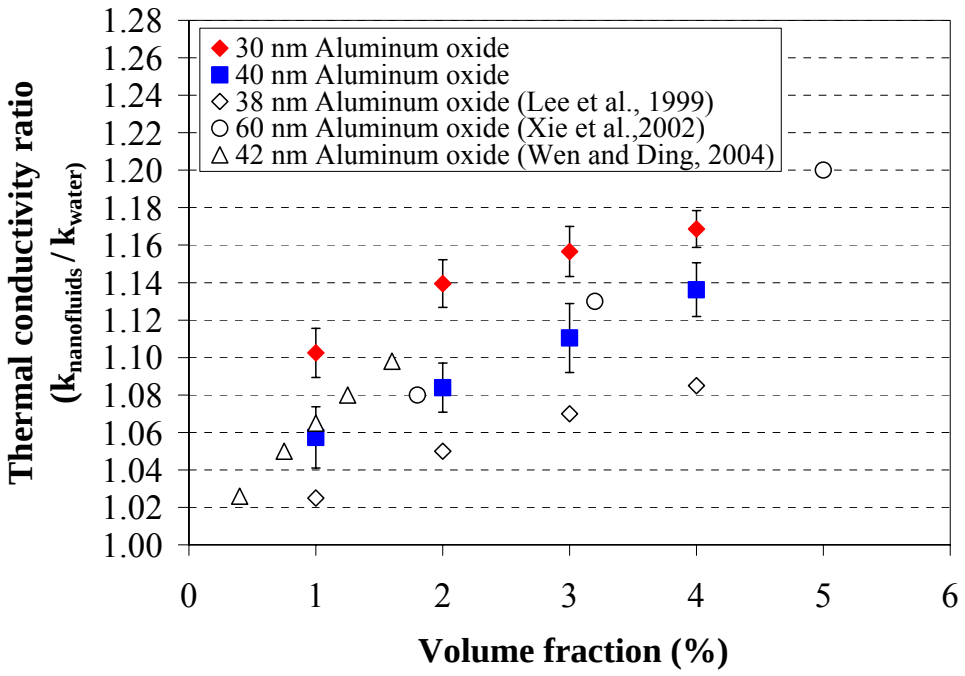

Figure 2.3. Thermal conductivity of Al_2O_3 nanofluids

For our experimental data, it is obvious that the 30 nm Al_2O_3 nanofluids have

larger thermal conductivity enhancement than 40 nm ones. Only 4 vol% loading of Al_2O_3 nanoparticles can increase the thermal conductivity by 17% for 30 nm particles and 14% for 40 nm particles.

2.3.2. Diamond Nanofluids

Two diamond nanofluid samples received from Saint-Gobain (Warren/Amplex Superabrasives were also tested. Both samples were formulated to have a volume fraction of 1.5% diamond:

- Diamond nanofluid #1: 100 nm mono-crystalline diamond with no coating.
- Diamond nanofluid #2: 200 nm carbon outer coated diamond.

The thermal conductivity of both diamond nanofluid samples was measured by short wire probe and the results are presented in Table 2.7. Diamond nanofluid # 1 has an enhancement of 13% in thermal conductivity and diamond nanofluid # 2 has an enhancement of 8%.

Table 2.7. Thermal conductivity measurement results of diamond nanofludis

	Diamond nanofluid #1	Diamond nanofluid #2
Thermal conductivity (W/m-K)	0.687	0.657
Thermal conductivity enhancement (relative to deionized water)	13%	8%

2.3.3. Carbon Nanotube Nanofluids

Stable multi-wall carbon nanotubes (MWCNT) suspension in pure water was obtained using 0.1 wt% sodium dodecyl sulfate (SDS) as surfactant and subjected to 30

min of ultrasonic homogenization, as described in Chapter. The test nanotubes were purchased from Shenzhen Nanotech Port Co., which has mean diameter of 10-20 nm and length of 5-15 μm. Thermal conductivities at different volume fraction were measured by short-wire probe. However, as shown in Figure 2.4, the thermal conductivity enhancements are only 1.9%, 2.5%, and 3.4%, respectively for the volume fraction of 0.2%, 0.4%, and 0.6%, which is not as high as expected. This is probably attributed to the dispersion method as well as the quality of nanotubes.

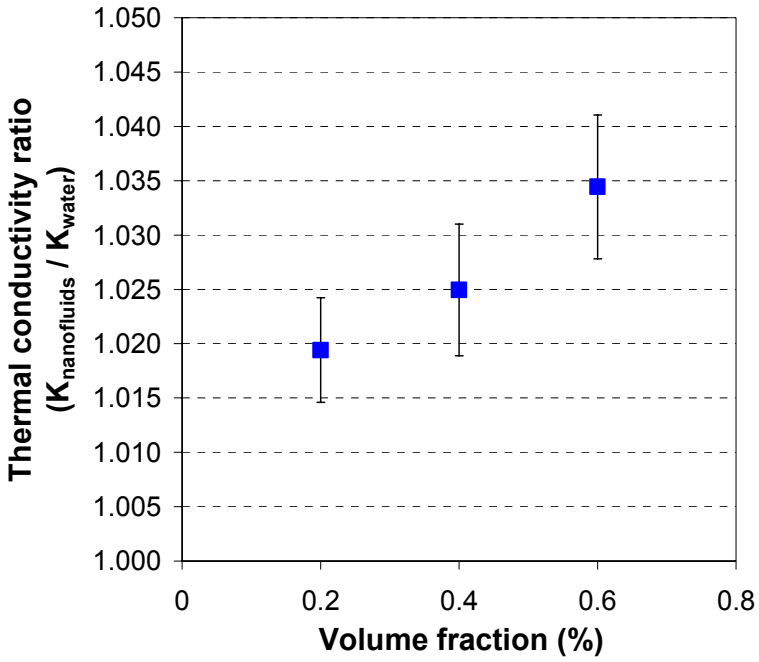

Figure 2.4. Thermal conductivity of MWCNT nanofluids

2.3.4. High Volume Fraction Nanofluids

Six samples of high volume fraction nanofluids are provided by Nanophase, as discussed in Section 2.2.2. Nanofluids with various volume fractions can be further obtained by dilution with deionized water.

The thermal conductivity measurement of water-based Al_2O_3 nanofluids with particle sizes of 20, 46, and 80 nm is shown in Figure 2.5. The thermal conductivity enhancement increases with increasing volume fraction of nanoparticles. The improvement of thermal conductivity reaches 43% with 22 vol% of 80 nm Al_2O_3 nanoparticles. It also indicates that the larger particle size has larger enhancement in thermal conductivity.

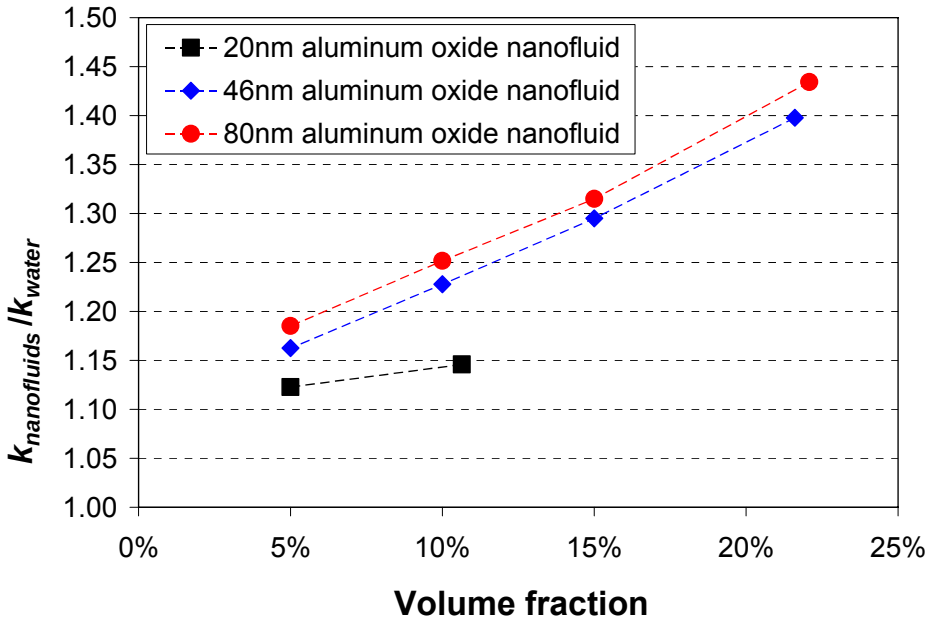

Figure 2.5. Thermal conductivity of high volume fraction Al_2O_3 nanofluids

The thermal conductivity of water-based ZnO nanofluids with particle sizes of 20, 40, and 60 nm was also characterized and plotted in Figure 2.6. The results are very similar to those of Al_2O_3 nanofluids. The thermal conductivity enhancement increases with increasing volume fraction of nanoparticles, as well as the increasing particle size. For the ZnO nanofluid with a particle size of 60 nm, the increase in thermal conductivity is about 61% at the 15 vol%.

In addition, the experimental results indicated that the ZnO nanofluids have better thermal conductivity improvement than Al_2O_3 nanofluids. This is probably because the thermal conductivity of ZnO is about three times higher than that of Al_2O_3.

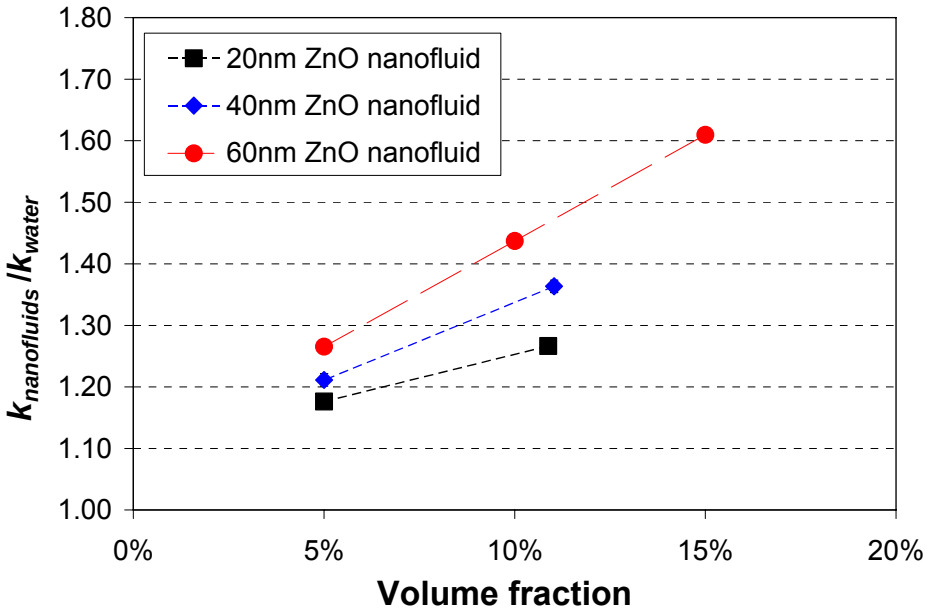

Figure 2.6. Thermal conductivity of high volume fraction ZnO nanofluids

Thermal conductivity is a critical to the heat conduction, but when it comes to the cooling application of fluids, convection becomes more of significant. Moreover, since there is increasing demand for more efficient microchannel cooling in microelectronics and fuel cell application, it is necessary to study cooling behavior of nanofluids in microchannels. Therefore, convection heat transfer of nanofluids in microchannels was investigated in this research.

2.4. Convection Heat Transfer Coefficient Measurements

The internal pipe flow convection coefficient of nanofluids was measured experimentally. The principle, experimental setup and the calibration can be found in Appendix A.2.

The water-based Al_2O_3 nanofluid from Nanophase was diluted to various volume fractions for convection heat transfer coefficient study. The suspended Al_2O_3 particle has an average size of 46 nm. The high volume fraction results in the high viscosity of the fluid and a tendency for the nanoparticles to stick on the walls of tubing and containers. It also requires large pumping power. Therefore, the highest concentration of the testing fluid in this study was 5 vol%. The thermal conductivity of these testing fluids were measured and summarized in Table 2.8.

The Nusselt number versus Reynolds number from the experiments are plotted in Figure 2.7. All the Al_2O_3 nanofluids have higher Nusselt number than water under the same Reynolds number. In general, the Nusselt number increases with increasing Reynolds number as well as the volume fraction of the suspended Al_2O_3 nanoparticles.

However, when interpreting the experimental results in terms of flow rate and convection heat transfer coefficient, as seen in Figure 2.8, there is no significant difference between the Al_2O_3 nanofluids and water.

The reason why we saw higher Nusselt number in Figure 2.8 is because of the higher viscosity of the nanofluids. The viscosity of the testing fluid is measured using a Brookfield Engineering LV-DV-II + PRO Digital Viscometer, as listed in Table 2.8. Given the same flow rate, the Reynolds number would be lower if the fluid has a higher viscosity. Therefore, the nanofluids with higher viscosity have the higher Nusselt number

under the same Reynolds number, which is actually corresponding to a higher flow rate.

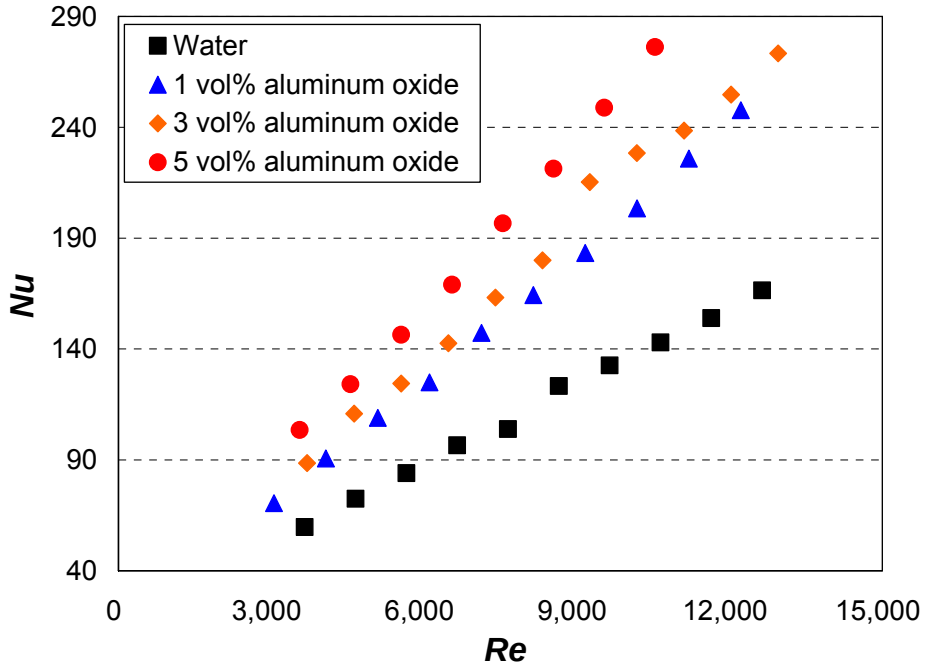

Figure 2.7. Nusselt number versus Reynolds number

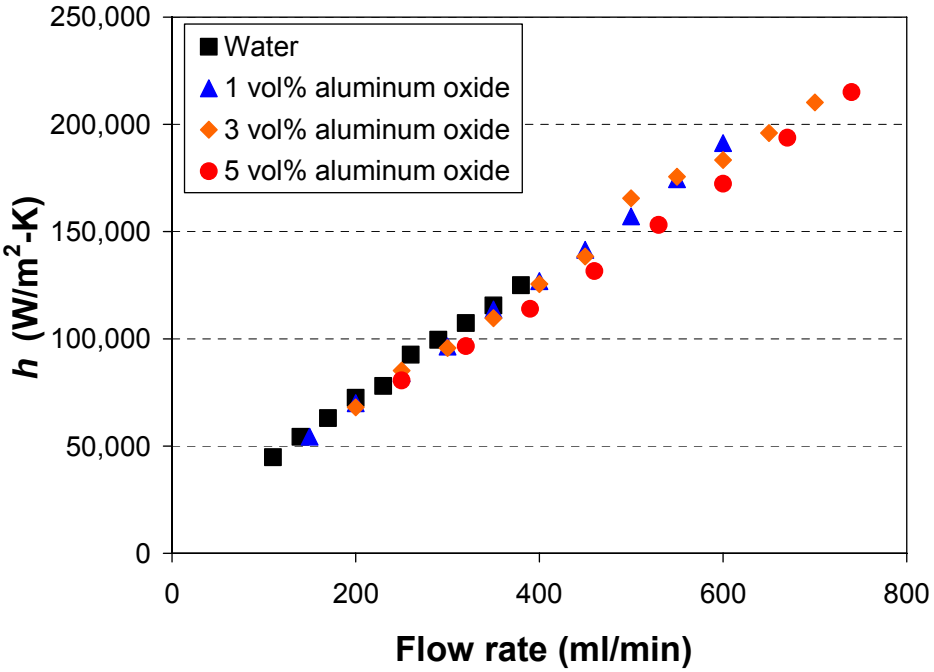

Figure 2.8. Convection heat transfer coefficient flow rate

Table 2.8. Physical properties of testing fluids (room temperature)

Fluid	Volume Fraction	Thermal Conductivity (W/m-K)	Density (kg/m^3)	Viscosity (Ns/m^2)
Water	--	0.61	997	8.55×10^{-4}
Al_2O_3 nanofluids (NanoDur X1121W)	1%	0.62	1030	1.30×10^{-3}
	3%	0.63	1080	1.50×10^{-3}
	5%	0.66	1130	2.04×10^{-3}

2.5. Concluding Remarks

Two-step physical process was used to synthesize nanofluids containing Al_2O_3 nanoparticles and multi-wall carbon nanotubes. Diamond nanofluids and high volume fraction nanofluids were also acquired from Saint-Gobain Warren Amplex Superabrasives and Nanophase, respectively.

Both the long and short hot wire probes were developed to measure the thermal conductivity of nanofluids based on transient hot wire method. For Al_2O_3 nanofluids, the thermal conductivity enhancement increases with increasing volume fraction of nanoparticles. Only 4 vol% loading of Al_2O_3 nanoparticles can increase the thermal conductivity by 17% for 30 nm particles and 14% for 40 nm particles. Diamond nanofluids also show some enhancement in thermal conductivity (13% for 100 nm diamond particles and 8% for 200 nm diamond particles at 1.5 vol%). However, carbon nanotube nanofluids only have little enhancement in thermal conductivity. This is probably attributed to the dispersion method as well as the quality of nanotubes. High volume fraction water-based Al_2O_3/ZnO nanofluids were also tested. Much higher thermal conductivity enhancement of 61% was observed for ZnO nanofluids at 15 vol%.

The convection heat transfer coefficient measurement apparatus was also

developed. The calibration was conducted on pure water and the results are consistent with the literature. The water-based Al_2O_3 nanofluid (average particle size of 46 nm) of various volume fractions was used for convection heat transfer study. The nanofluids showed higher Nusselt number than its base fluid at the same Reynolds number; however, in terms of convection heat transfer coefficient vs. flow rate, there is no significant difference between the nanofluids and the base fluid. The increase in Nusselt number of nanofluids is mainly due to the higher viscosity, compared to the base fluid.

CHAPTER 3

MINIMUM QUANTITY LUBRICATION (MQL) GRINDING USING NANOFLUIDS

MQL grinding (conventional abrasive wheels) of cast iron using water based and oil based nanofluids was investigated. Grinding performance is evaluated and compared in terms of grinding force, G-ratio, and surface roughness, etc.

Water-based Al_2O_3 and diamond nanofluids were applied in MQL grinding process and the grinding results were compared with those of pure water. During the nanofluid MQL grinding, a dense and hard slurry layer was formed on the wheel surface and could benefit the grinding performance. Experimental results showed that G-ratio, defined as the volume of material removed per unit volume of grinding wheel wear, could be improved with high concentration nanofluids. However, water based nanofluids are not able to provide superior cooling capacity in MQL grinding process. Thus, the research of MQL grinding using nanofluids focuses on the advanced lubrication properties hereafter.

Oil-based nanofluids were also applied in MQL grinding. Active MoS_2 nanoparticles were added in low and high concentrations, to three commercially available

base oils. To test value addition due to nanoparticles, their MQL grinding performances were compared with that of the pure base oils (without MoS_2 nanoparticles) and with regular water based grinding fluid using flood cooling (wet) application. The results showed that lubricants with novel MoS_2 nanoparticles significantly reduces the tangential grinding force and friction between the wear flats and the workpiece, increases G-ratio and improves the overall grinding performance in MQL applications.

3.1. Background

Grinding is widely used as the finishing machining process for components that require smooth surfaces and precise tolerances. Large fluid delivery and cooling systems are evident in production plants. As mentioned in Chapter 1, from both environmental and economical points of view, there are critical needs to reduce the use of cutting fluid in grinding process, and MQL grinding is a promising solution.

MQL grinding using conventional abrasive wheel has been investigated (Brinksmeier et al., 1997; Baheti et al., 1998; Hafenbraedl and Malkin, 2000), and it was concluded that MQL has shortcomings of insufficient workpiece cooling with conventional abrasives.

The fluid and the grinding wheel are the key technical areas that can enable the success of MQL grinding processes. The advanced heat transfer and tribological properties of nanofluids may provide better cooling and lubricating in the MQL grinding process, and make it production-feasible.

3.2. MQL Grinding using Water Based Nanofluids

3.2.1. Experimental Setup

The grinding experiments were conducted in an instrumented Chevalier Model Smart-B818 surface grinding machine. The setup of the grinding experiment is shown in Figure 3.1. A vitreous bond aluminum oxide grinding wheel (Saint-Gobain/Norton 32A46-HVBEP) with 508 μm average abrasive size was used. The initial diameter and the width of wheel were 177.8 mm and 12.7 mm, respectively. The workpiece material was Dura-Bar 100-70-02 ductile iron with a carbon content of 3.5-3.9% and hardness of 50 Rockwell C. The width and length of the workpiece surface for grinding are 6.5 mm and 57.5 mm, respectively. MQL grinding utilized a special fluid application system shown in Figure 3.1(b) provided by AMCOL (Hazel Park, Michigan). In this system, biaxial hose is used to independently transport liquid and air to the point of use and then the liquid is surrounded with air (coaxial) and propelled onto the tool or workpiece by air pulse. For flood cooling, Cimtech 500 synthetic grinding fluid at 5 vol% concentration was used and the flow rate was measured 5400 ml/min. For MQL grinding, the flow rate was set to 5 ml/min for all grinding fluids including water-based nanofluids.

The surface grinding parameters were kept constant throughout the experiment – 30 m/s wheel surface speed, 10 μm depth of cut and 2400 mm/min workpiece velocity (feed rate). Before every test, the grinding wheel was dressed at 10 μm down feed, 500 mm/min traverse speed and −0.4 speed ratio using a rotary diamond disk with 96 mm diameter and 3.8 mm width.

The normal and tangential grinding forces were measured using a Kistler Model 9257A piezoelectric dynamometer. The grinding temperatures were measured by the

embedded thermocouple method (Shen et al., 2009), which will be discussed in detail in Chapter 4. After each grinding pass, the workpiece was allowed to cool to the initial temperature before the next pass was taken. The wheel wear measurement method is the same as described in (Shih et al., 2003). The wheel was 12.7 mm wide. The width of the part was narrower, 6.5 mm. A worn groove was generated on the wheel surface after grinding. A hard plastic part was ground to produce a replica of the worn grinding wheel. A Taylor Hobson Taylorsurf profilometer was used to measure the depth of wheel wear on the replica. Each G-ratio grinding test had to wear out at least 6 μm of the wheel to ensure the accuracy of G-ratio. The same profilometer was used to measure the surface roughness of ground surfaces. Three measurement traces parallel and perpendicular to the grinding direction were measured. The average of the three arithmetic average surface roughness (R_a) measurements along and across the grinding direction was used to represent the roughness of a ground surface.

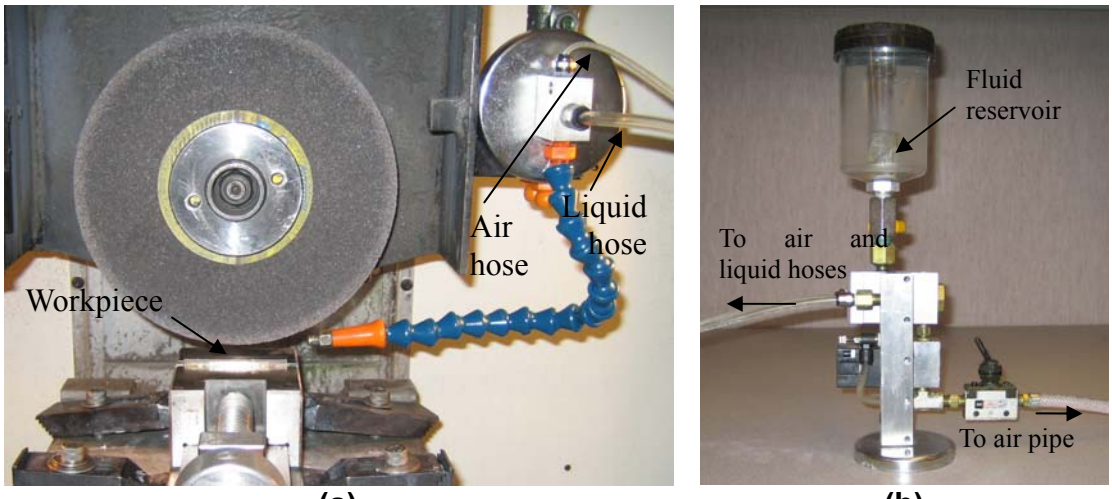

Figure 3.1. Experimental setup: (a) Experiment layout and (b) MQL fluid delivery device

3.2.2. Grinding Fluids

Four types of fluids were used in grinding tests, water-based Cimtech 500 (Milacron, Cincinnati, OH) synthetic grinding fluid at 5 vol% concentration, pure water, water-based Al_2O_3 nanofluids, and water-based diamond nanofluids. The Al_2O_3 nanofluids were prepared by dispersing 40 nm Al_2O_3 nanoparticles (NovaCentrix, Austin, Texas) to the deionized water. Three volume fractions of Al_2O_3 nanofluids at 1.0%, 2.5% and 4.0% were tested. The 4.0 vol% is already on the high side of concentration for Al_2O_3 nanofluids because of the noted increase in viscosity. Two diamond nanofluids samples are provided by Warren/Amplex Superabrasives of Saint-Gobain. Both samples are formulated to have weight fraction of 250 carats/1000 ml, which have an equivalent volume fraction of 1.5% diamond. One sample contains 200 nm carbon coated diamonds and the other contains 100 nm non-coated mono-crystalline diamonds.

Table 3.1. Fluid thermal conductivity

Fluids		Thermal conductivity (W/m-K)	Thermal conductivity enhancement
Deionized water		0.603	--
Cimtech 500 synthetic fluid (5 vol%)		0.593	--
Al_2O_3 nanofluids (40 nm diameter)	1.0 vol%	0.645	7%
	2.5 vol%	0.670	11%
	4.0 vol%	0.693	5%
Diamond nanofluids (200 nm carbon coated)	1.5 vol%	0.654	6%
Diamond nanofluids (100 nm non-coated)		0.684	10%

The thermal conductivity of fluids involved are all measured at room temperature using transient hot wire method as described in Chapter 3. The results are summarized in Table 3.1. All the nanofluids show some enhancement in thermal conductivity. Al_2O_3

nanofluids have thermal conductivity enhancement of 7%, 11% and 15% for 1.0%, 2.5% and 4.0% volume fraction concentration, respectively. Diamond nanofluids at 1.5 vol% have thermal conductivity enhancement of 6% for 200 nm carbon coated diamond and 10% for 100 nm non-coated diamond. The 5% concentration Cimtech 500 synthetic grinding fluid causes the thermal conductivity drop to 0.593 W/m-K.

3.2.3. Grinding Forces

The specific grinding forces, which is defined as the forces divided by the width of grinding, vs. passes are shown in Figures 3.2 and 3.3. These forces are the average values in each grinding pass. The grinding forces for every 5 passes are plotted. As shown in Figure 3.2, flood cooling and MQL grinding using Cimtech 500 generate similar normal and tangential forces during the entire process. These forces are lower than MQL grinding using pure water, which is expected because of the better lubricating properties of Cimtech 500 cutting fluid. Dry grinding without lubrication generates the highest forces. On the other hand, the forces increase with the number of passes, which contributes to the wheel wear. Notice that the forces for dry grinding increase exponentially after 110 passes. These large forces generate excessive heat and lead to visible burning of the workpiece, which can be identified by discoloration on the ground workpiece surface.

MQL grinding force results using pure water (considered as the datum) and water based nanofluids are compared in Figure 3.3. In the beginning (before 35 passes), all the forces are comparable. With increasing passes, MQL grinding using different fluids exhibit different performance. For Al_2O_3 nanofluids, at 1.0 vol% low concentration, the

grinding forces increase progressively which is similar to the case of pure water. At higher concentration (2.5 and 4.0 vol%), the grinding forces remain flat after increasing in the beginning. This may be due to the hard and dense slurry layer observed on the grinding wheel. However, compared with Al_2O_3 nanofluid of 2.5 vol%, the one with 4.0 vol% gives much higher forces. The possible explation is that the high concentration of Al_2O_3 (4.0 vol%) leads to excessive loading of the vitreous bond grinding wheel, resulting in higher grinding forces.

For diamond nanofluids, the grinding forces become flat after about 45 passes. Again, the slurry layer is readily observed when using 200 nm carbon coated diamond nanofluids, but not for 100 nm non-coated diamond nanofluids. Intense loading on the wheel is likely why the grinding forces are higher with 200 nm carbon coated diamond nanofluid than with 100 nm non-coated diamond nanofluid. In general, the slurry layer can reduce the grinding forces by reducing the wheel wear, which is supported by the G-ratio measurement results.

The force ratio F_t / F_n indicates the combination of abrasive cutting and friction between the wear flats and the workpiece. In all the experiments, this ratio decreases from the beginning and then reaches a relatively steady state value. As shown in Figure 3.2, the force ratio is 0.15 for dry, 0.2 for pure water and Cimtech 500 MQL, and 0.25 for Cimtech 500 flood cooling grinding. For nanofluid MQL grinding, as shown in Figure 3.3, the force ratio is 0.25 for all three Al_2O_3 based nanofluids and about 0.27 and 0.2 for the 100 and 200 nm diamond nanofluids grinding, respectively. The initial drop is probably due to the rise of workpiece temperature during grinding. In dry grinding, the ratio is very low, which is attributed to the workpiece burning and associated phase

changes (Malkin, 1989).

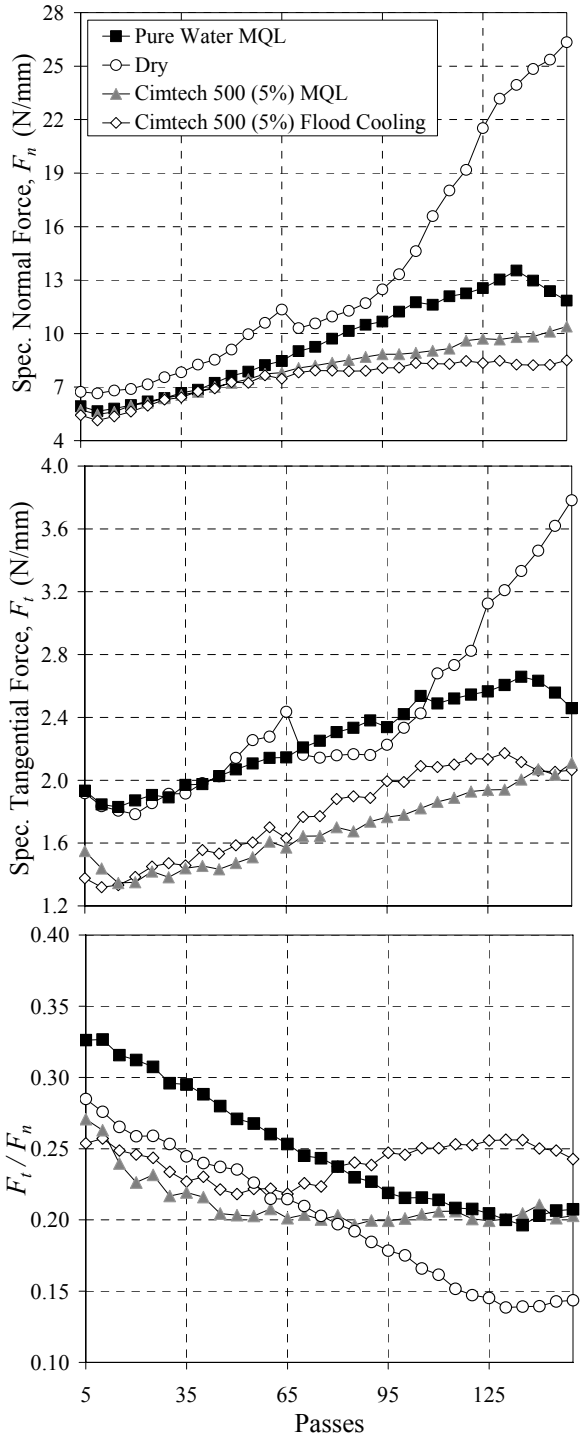

Figure 3.2. Specific grinding forces and force ratio for wet, dry and MQL grinding using Cimtech 500 and pure water

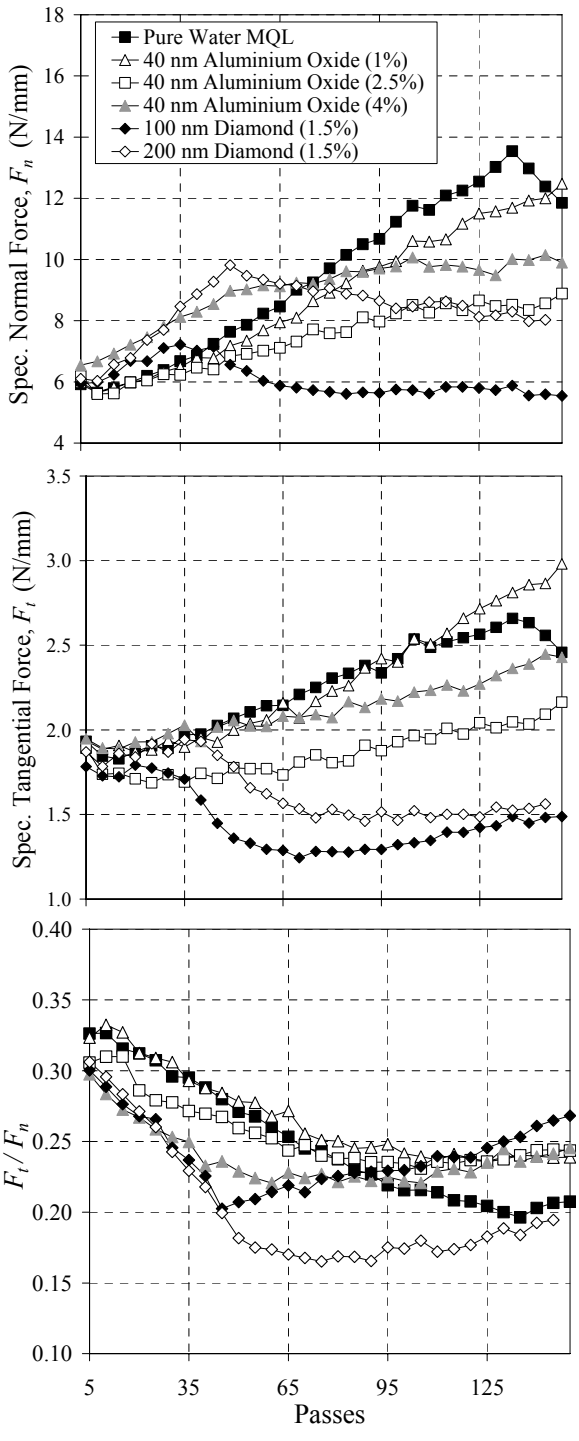

Figure 3.3. Specific grinding forces and force ratio for water based nanofluids MQL grinding

The specific tangential versus specific normal force for all grinding conditions are illustrated in Figure 3.4. For given grinding conditions, a plot of tangential versus normal force component per unit width should yield a straight line with a slope equal to the friction coefficient between the wear flats and the workpiece. According to Malkin's analysis (Malkin, 1989), above the burn limit, the slope gets steeper which suggests a decrease in friction coefficient associated with workpiece burn. The phase changes and the formation of oxides on cast iron workpiece cause the reduction in friction coefficient. This change in slope or friction coefficient is also observed in this study. As shown in Figure 3.4, the specific tangential grinding force of about 2.2 N/mm is the transition point for grinding burn and change of slope. This corresponds to a specific energy of 165 J/mm^3, which is a little higher than 135 J/mm^3 burning limit for low carbon and low alloy steels (Malkin, 1989).

Linear curve fitting was applied to data points above and below 2.2 N/mm specific tangential grinding force. In the absence of workpiece burn, below the specific tangential grinding force of 2.2 N/mm, the slope is 0.33, which implies a friction coefficient of 0.33 between the wear flats and the workpiece. With grinding burn, the slope is much lower, 0.09. This indicates a much smaller friction coefficient beyond this grinding burn point. This observation is consistent with the findings in previous grinding studies (Malkin, 1989). Workpiece burning, evidenced by visible discoloration, is apparent in three grinding conditions: dry, pure water MQL, and 1.0 vol% Al_2O_3 nanofluids MQL grinding. For dry grinding, except for several initial passes, most of the data points are above the burn limit. This has also been observed on the discoloration of the ground surface. In dry grinding the first few passes has no discoloration. After that,

severe discoloration was observed. The experimental observations of discoloration match to the burn limit prediction in Figure 3.4. Slight discoloration was observed for pure water and 1.0 vol% Al_2O_3 nanofluids MQL grinding. As shown in Figure 3.4, some data from these experiments also locate above the burn limit. For pure water, the lack of lubricity contributes to the workpiece burning. For 1.0 vol% Al_2O_3 nanofluid, it is likely attributed to the relatively high grinding force than the other nanofluids, as shown in Figure 3.3. No burning marks were observed for 2.5 vol% Al_2O_3 nanofluids, diamond nanofluids, flood cooling, and MQL grinding with Cimtech 500 as the specific tangential forces in these experiments are all below 2.2 N/mm.

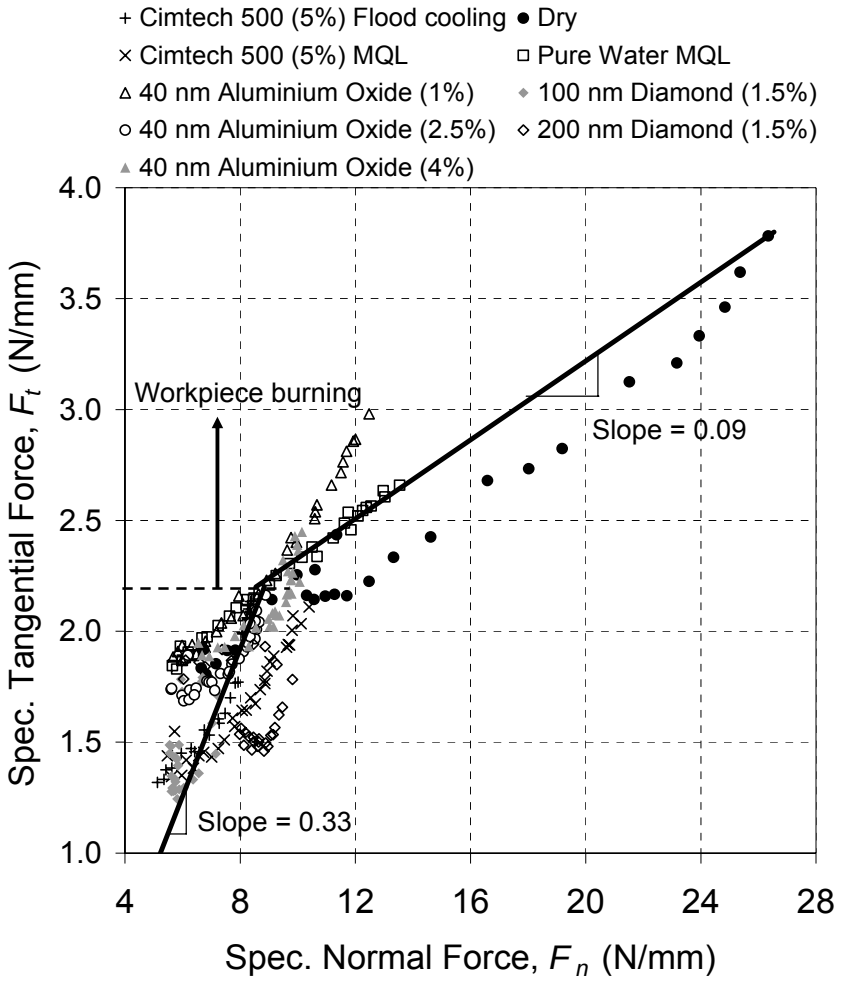

Figure 3.4. Specific tangential force vs. specific normal force

3.2.4. G-ratio

G-ratio is defined as the volume of work-material removed divided by the volume of wheel wear. A high G-ratio indicates low wheel wear rate. Nanofluid MQL grinding generally exhibits the high G-ratio, ranging from 16 to 33, as shown in Figure 3.5. Flood cooling and MQL grinding using Cimtech 500 provides similar G-ratio, about 17. Dry grinding exhibits the worst wheel wear, i.e., the lowest G-ratio, about 12, while MQL using pure water has only a slightly higher G-ratio than that of dry grinding.

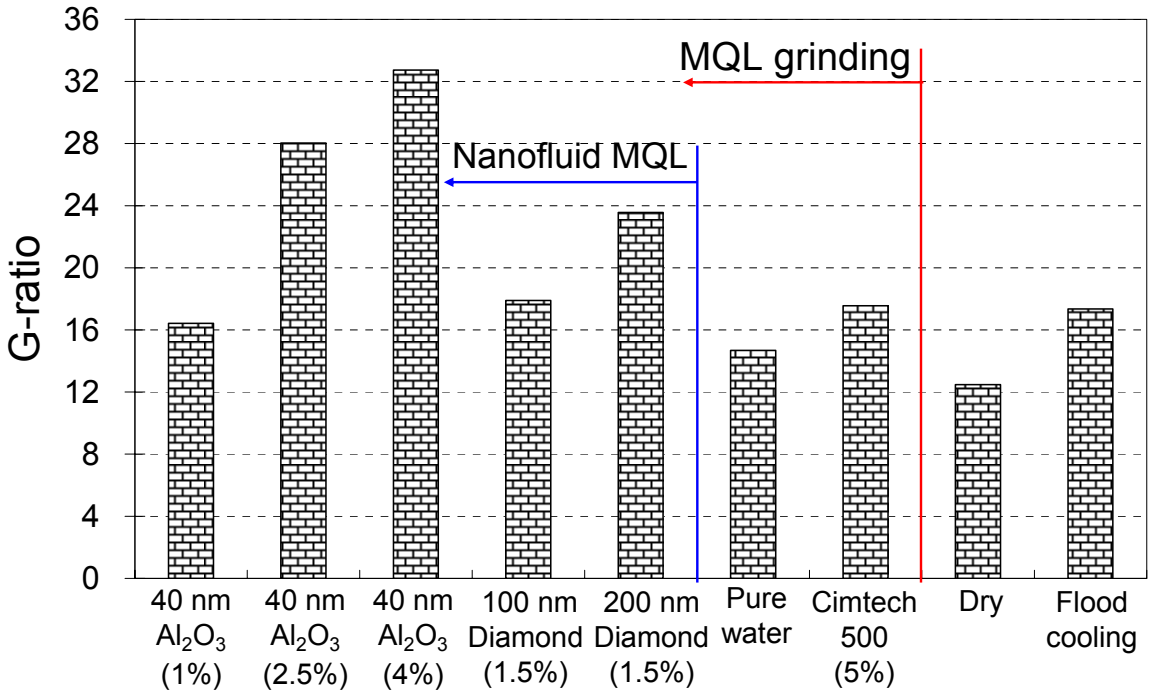

Figure 3.5. G-ratio results

For MQL grinding with Al_2O_3 nanofluids, the G-ratio increases with increasing volume fraction of Al_2O_3 nanoparticles. The two highest G-ratio results are observed in MQL grinding with 2.5 and 4.0 vol% Al_2O_3 nanofluids. This is attributed to the formation of the slurry layer which can protect the grinding wheel from grain/bond

fracture. High concentration nanofluid has better protection and improves the G-ratio. The slurry layer is not observed in MQL grinding with 1.0 vol% Al_2O_3 nanofluid, which has a low G-ratio. In early research (Komanduri and Reed, 1980), it was found that a thin slurry layer of silicon carbide on the wheel surface can protect the bonding material from thermal and/or mechanical degradation or damage, thereby causing a high G-ratio. This research further validates this observation.

For MQL grinding with diamond, the same phenomenon of slurry formation and high G-ratio was observed in the 200 nm diamond nanofluid. For the 100 nm diamond nanofluid, no slurry layer was observed and the G-ratio is lower than that of the 200 nm diamond nanofluids. Compared to the 100 nm diamond nanofluid, it should also be noted that the 200 nm diamond nanofluid is more viscous and more readily to form the slurry layer.

3.2.5. Surface Roughness

The surface roughness (R_a) of the ground workpiece are presented in Figure 3.6. Flood cooling has the best surface finish (lowest surface roughness). In general, MQL grinding using nanofluids has better surface finish than pure water but worse than the flood cooling and MQL grinding using Cimtech 500. Cimtech 500 synthetic grinding fluid provides good lubrication, while pure water has poor lubricating capability. The flood cooling also provides efficient chip flushing. The fact that the nanofluids outperform the pure water can be partly due to the reduction in grinding forces and friction. Dry grinding has the worst surface finish, which is expected.

For Al_2O_3 nanofluids, 2.5 vol% has better surface roughness than that of 1.0 and

4.0 vol%. The 2.5 vol% Al_2O_3 nanofluid has the lowest specific tangential grinding forces (see Figure 3.3) among the three. The 4.0 vol% Al_2O_3 nanofluid has lower specific tangential grinding forces than the 1.0 vol% Al_2O_3 nanofluid. As a result, the 4.0 vol% Al_2O_3 nanofluid has better surface finish across the grinding direction. However, along the grinding direction, it has worse surface finish than the 1.0 vol% Al_2O_3 nanofluid. This is likely due to the thicker slurry layer in 4.0 vol% Al_2O_3 nanofluid MQL grinding, which may scratch the workpiece along the grinding direction.

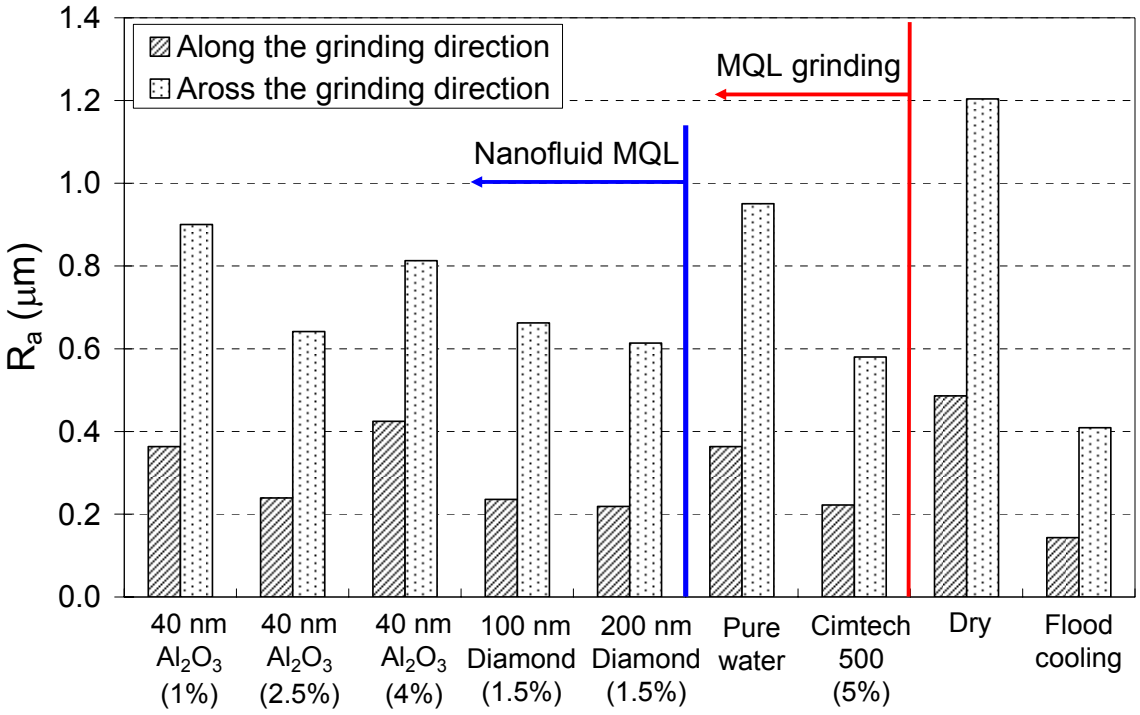

Figure 3.6. Surface roughness results

The 200 nm coated diamond nanofluids have slightly better surface finish than the 100 nm non-coated diamond nanofluid. Although the former has slightly higher tangential forces, it has lower force ratio (friction coefficient). In general, diamond nanofluids perform better than Al_2O_3 nanofluids in terms of surface roughness due to of

the lower specific tangential grinding forces, as seen in Figure 3.3.

3.2.6. Grinding Temperature

The comparison of wet, dry, and MQL grinding temperature at the workpiece surface was plotted in Figure 3.7. Flood cooling has the lowest temperature and dry grinding has the highest, which is expected. In Figure 3.7, all the MQL grinding experiments have the same flowrate (5 ml/min). By applying MQL, the peak temperature is about 100-150°C lower than that in dry grinding. This is due to both cooling and lubrication effects of the fluids provided by MQL, as lubrication reduces the cutting forces and cutting energy, while convection heat transfer and/or boiling carries away some of the heat.

There is no significant difference in grinding temperature among the experiments using different types of fluids for MQL grinding. The Cimtech 500 synthetic grinding fluid has slightly lower grinding temperature. This is probably attributed to the better lubrication properties of Cimtech 500 synthetic grinding fluid. The 4.0 vol% aluminum oxide nanofluids also has a slightly lower workpiece surface grinding temperature. This is probably due to the dense slurry layer formed during grinding, which may cause more heat to enter the grinding wheel rather than the workpiece.

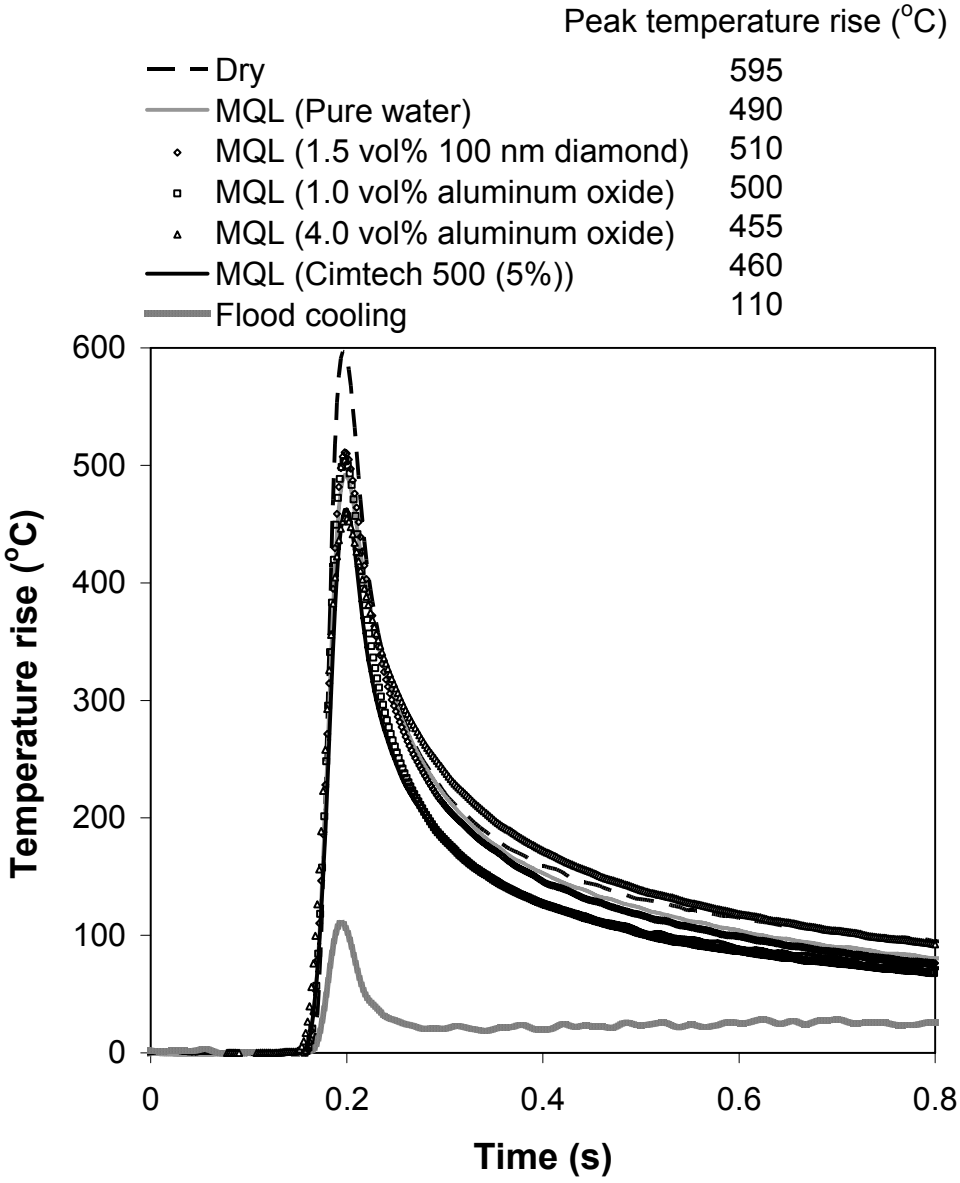

Figure 3.7. Comparison of wet, dry, and MQL grinding temperature at the workpiece surface (5 ml/min flowrate for MQL grinding)

3.2.7. Summary

Grinding of cast iron under different lubrication conditions was studied. Grinding performance was investigated and compared in terms of grinding forces, G-ratio, and surface roughness. Dispersion of solid particles was found to play an important role,

especially when a slurry layer was formed. The slurry layer generated higher G-ratio (less wheel wear), smaller grinding forces and better surface finish. To elucidate how the slurry layer forms and how the dispersed solid particles and the slurry layer affect the grinding performance, further research is needed.

The preliminary study of MQL grinding showed that it could significantly reduce the grinding temperature compared to dry grinding. However, there is no significant difference in grinding temperature when using nanofluids. This is probably because that the amount of the nanofluids applied in MQL grinding is too small to make any difference even though they have better thermal conductivity. In addition, convection is probably the dominant cooling phenomenon for cutting fluids in grinding processes rather than conduction. According to the previous convection heat transfer study of nanofluids (Chapter 2), Al_2O_3 nanofluids virtually showed no improvement in the convection heat transfer coefficient compared to the base fluid.

From above, it is concluded that nanofluids are not able to provide superior cooling capacity in MQL grinding process. Therefore, the future research of application of nanofluids in MQL grinding should focus on the advanced lubrication properties.

3.3. MQL Grinding using Oil Based Nanofluids

The core functionalities of cutting fluids are to cool and lubricate the grinding zone. The water based fluids are used mainly where good cooling properties are required, while the oil based fluids are used mainly where good lubricating property is a major requirement.

Although the nanofluid has showed enhanced thermal conductivity, it was unable

to improve the convection heat transfer properties. The experimental results in the previous section further confirmed that there is no advantage of applying nanofluids in MQL grinding in terms of workpiece cooling (Shen et al., 2008a). On the other hand, the suspension of nanoparticles can also improve the tribological properties of the base fluids, which can help lubricate the grinding zone. Therefore, the oil based nanofluids with advanced tribological properties are now considered for MQL grinding.

Molybdenum disulphide MoS_2 is a predominant material used as solid lubricant, due to their hexagonal closed pack (HCP) lamellar structure. The lamellas orient parallel to the surface in the direction of motion (Wu et al. 2006). According to Verma et al. (2007) and others, MoS_2 in its nanoparticulate form has exceptional tribological properties, showing that MoS_2 nanostructured additive in paraffin oil reduces friction under extreme pressure conditions. Malshe and Verma (2006) proposed for the first time that nanoparticles of MoS_2 suspended in the grinding fluid could navigate in the grinding wheel – workpiece contact zone and provide significant lubrication.

In this section, MQL grinding performance of different lubricants with MoS_2 nanoparticles additives was evaluated and compared with that of conventional flood application.

3.3.1. Experimental Setup

The experimental setup is exactly the same as in Section 3.2.1, as is the grinding parameter. The flow rate was selected at 5400 ml/min for flood cooling (wet) application and 5 ml/min for MQL.

3.3.2. Grinding Fluids

For flood cooling application, water based synthetic grinding fluid Cimtech 500 (5 vol% concentration) was used. For MQL application, three commercially available oils; namely: paraffin oil (mineral based oil), soybean oil (vegetable based oil) and commercial MQL metal working fluid CANMIST (high purity fatty alcohol based oil, AMCOL Corp.) were chosen as the base fluids, as listed in Table 3.2.

Table 3.2. Summary of base fluids

Name	Type	Application
Cimtech 500	Water based synthetic grinding fluid (5 vol%)	Flood
Paraffin oil	Mineral based	MQL
Soybean oil	Vegetable based	MQL
CANMIST oil	High purity fatty alcohol based	MQL

MoS_2 nanoparticles based grinding lubricant additive consisted of molybdenum disulphide nanoparticles (<100nm) intercalated with triglyceride chemistry plus emulsifier (Alcolec) lecithin. This additive was dispensed in the three base oils. These control media were selected based upon published literature and authors' prior experience. Soybean and paraffin oil is used as base oil in a number of commercially available grinding fluids, for example, "Tru Cut 203NC" a paraffin oil based grinding fluid and **"**ELM SoyEasy UNI-Cut™", a soybean oil based grinding fluid.

To prepare the described nanoengineered molybdenum disulphide additive (Malshe et al., 2006), first, MoS_2 in powder form (Alfa Aesar, 98% pure, 3-5 μm average particle size) was ball milled in SPEX 8000D mixer mills using hardened steel vials (with a constant ball to powder ratio of 2:1) for 48 hours. This dry milled MoS_2 was then added to pure canola oil (Crisco) with a ratio of 1:1.5 (dry milled MoS_2: Canola oil) % by weight and again ball milled for 48 hours using the same equipment.

From high resolution transmission electron microscope (TEM) analysis, it was found that the resultant nanoengineered MoS_2 particles shaped like "elongated coconut" as shown in Figure 3.8. The average size of MoS_2 particle repetitively measured by HRTEM was about 70 nm along major axis and 40 nm along minor axis.

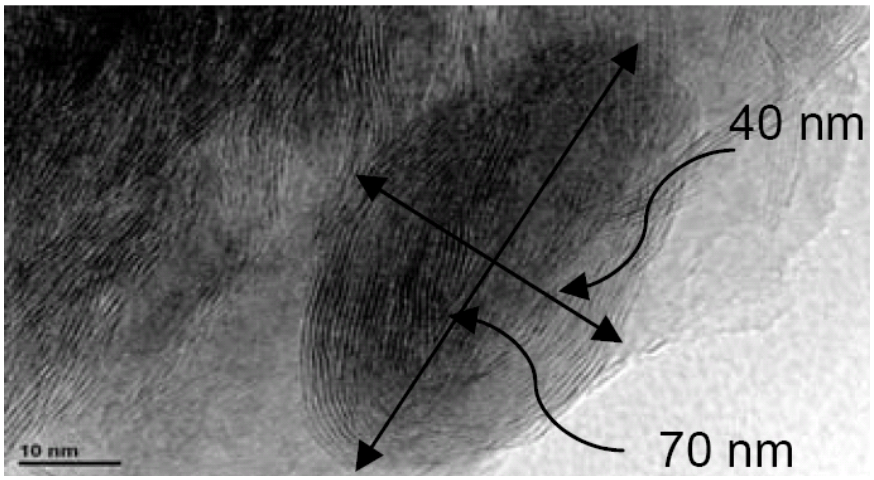

Figure 3.8. TEM image of nanoengineered MoS_2 particle (Shen et al., 2008b).

Particle size analysis was done on nanoengineered MoS_2 ($nMoS_2$) additive to determine the domain size of the particles using HORIBA laser scattering particle size distribution analyzer, LA950 model. The particle size distribution is shown in Figure 3.9.

The average size of agglomeration of $nMoS_2$ particles was found to be 250 nm, using particle size analyzer. Therefore, comparing both HRTEM results and particle size analysis results, it can be concluded that the MoS_2 particles present in the dispersions are nanosized particles.

Dispersions were prepared by mixing hybrid MoS_2 additive and base oil. Considering the severe challenge of deagglomeration with respect to nanoparticles, an emulsifier (lecithin) was added to $nMoS_2$ additive (additive: emulsifier, 1:2) before

adding to base oil. The dispersions were physically agitated followed by ultrasonication (BRANSONIC ultrasonic cleaner) for four hours to ensure homogeneity of the dispersions used in MQL grinding.

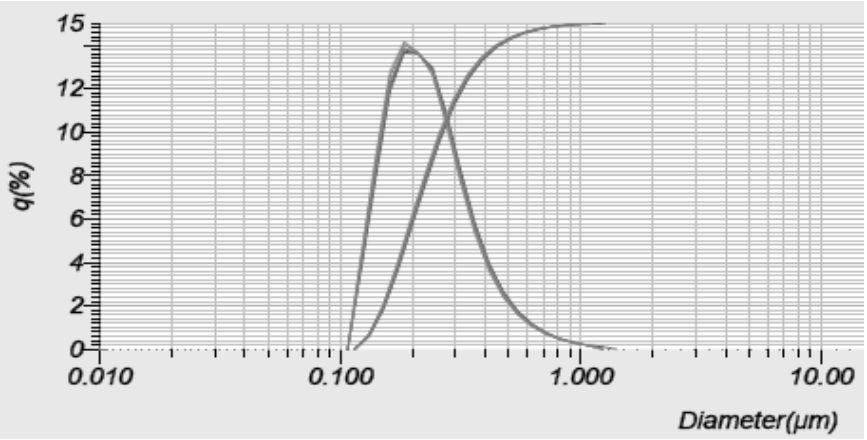

Figure 3.9. Particle size distribution of nanoengineered MoS_2

Nanoengineered MoS_2 additive, in MQL dispersions, was added in two concentrations, referred as high concentration (20% by weight of $nMoS_2$) and low concentration (5% by weight of $nMoS_2$). A total of nine samples, including the base fluids and the base oils with MoS_2 nanoparticle additives, were used in MQL application, as summarized in Table 3.3.

The nanoparticle design used in the present study consisted of three multilayers of chemistry at the nanoscale, particularly (1) MoS_2, (2) overlayer of Canola Oil (triglyceride molecules) and (3) lecithin. ApNano Materials, Inc. New York, has carried out an extensive research on health and safety aspects of fullerene type MoS_2 nanoparticles based lubricants. They found it to be non-toxic and an environmentally friendly material. Further, MoS_2 is extensively used as solid lubricant in various manufacturing and application sectors using proper safety precautions stated in MSDS

(CAS no.1317-33-5). Canola oil and lecithin (emulsifier) are traditionally, environmental and human friendly chemistries used as edible oil and common ingredient of food respectively.

Table 3.3. Summary of samples for MQL application

Samples	MoS_2 (weight %)	Emulsifier (Lecithin) (weight %)
Paraffin oil	--	--
Paraffin oil (Low)	2%	10%
Paraffin oil (High)	8%	40%
Soybean oil	--	--
Soybean oil (Low)	2%	10%
Soybean oil (High)	8%	40%
CANMIST	--	--
CANMIST (Low)	2%	10%
CANMIST (High)	8%	40%

3.3.3. Grinding Forces

According to Malkin et al. (2007), the forces generated in grinding are directly proportional to the grinding energy, which depends on chip formation, plowing effect and sliding of grains over the surface of workpiece. The specific tangential grinding forces and force ratio, F_t/F_n (F_t: specific tangential grinding force, F_n: specific normal grinding force) vs. passes for all the grinding fluids are shown in Figures 3.10-3.13. The plotted forces are the average value of every 5 grinding passes. MQL grinding with pure base oils (without $nMoS_2$) generate lower tangential forces than flood cooling as shown in Figure 3.10. This clearly demonstrates that, MQL system was able penetrate into the region of contact between the grinding wheel and the workpiece more effectively than flood cooling. Among the base oils, soybean oil seemed to generate lowest tangential

grinding force while the other two oils performed likely, although paraffin oil has slightly lower tangential grinding forces than CANMIST oil at the beginning. The force ratio is 0.23 for flood cooling with Cimtech 500, 0.20 for MQL with both CANMIST and paraffin oil, and 0.16 for MQL with soybean oil. This indicates the lubrication properties of each base fluid. It is apparent that the water-based Cimtech 500 has the least lubrication, while soybean oil has the best among the three offered base oils.

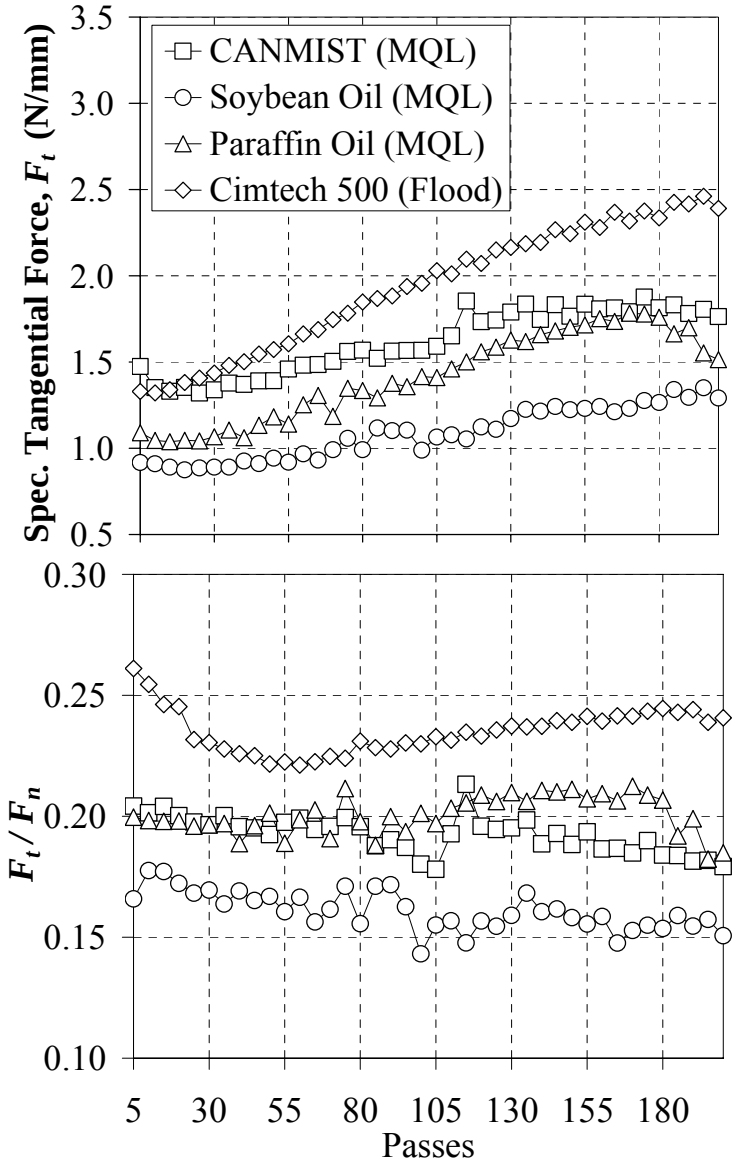

Figure 3.10. Specific tangential grinding forces and force ratio for base fluids and flood cooling

The comparison of specific tangential grinding forces and force ratio (F_t/F_n) for CANMIST and paraffin oil based lubricant group is shown in Figures 3.11 and 3.12, respectively. The lubricants with above described $nMoS_2$ showed significant improvement in grinding performance by lowering the grinding forces and the force ratio. CANMIST and paraffin oils with $nMoS_2$ significantly reduced the grinding forces as well as the friction between the wear flats and the workpiece as compared to the base fluids. This significant reduction can be attributed to the enhanced penetration of MoS_2 nanoparticles and their entrapment at the grinding interface. This action results in the formation of a durable tribofilm that effectively improves the slipping of grains between the wheel and the workpiece offering advanced "on-site" lubrication under extreme pressure. Although the fluids with high $nMoS_2$ concentration (20%) showed lowest tangential force and grinding force ratio, the reduction was not very significant compared to that of fluids with low $nMoS_2$ concentration (5%). This shows that by adding a small quantity of $nMoS_2$ additive, the grinding performance can improve significantly.

For soybean oil based fluids, as shown in Figure 3.13, the improvement with the $nMoS_2$ is relatively less as compared to the other two groups. The reduction in grinding forces with $nMoS_2$ additive (both low and high concentration) is less, and there is virtually no improvement of friction between the wear flats and the workpiece compared to that of pure soybean oil (without $nMoS_2$). This indicates that the improvement of lubrication with $nMoS_2$ additive could also depend on the base fluid chemistry which will guide their interaction (teaming) with the molecules of emulsifier and canola oil present along with the MoS_2 nanoparticles. Thus the selection of appropriate base fluid is also critical in the application of $nMoS_2$ based lubricants in MQL grinding and requires

further course of research in this field.

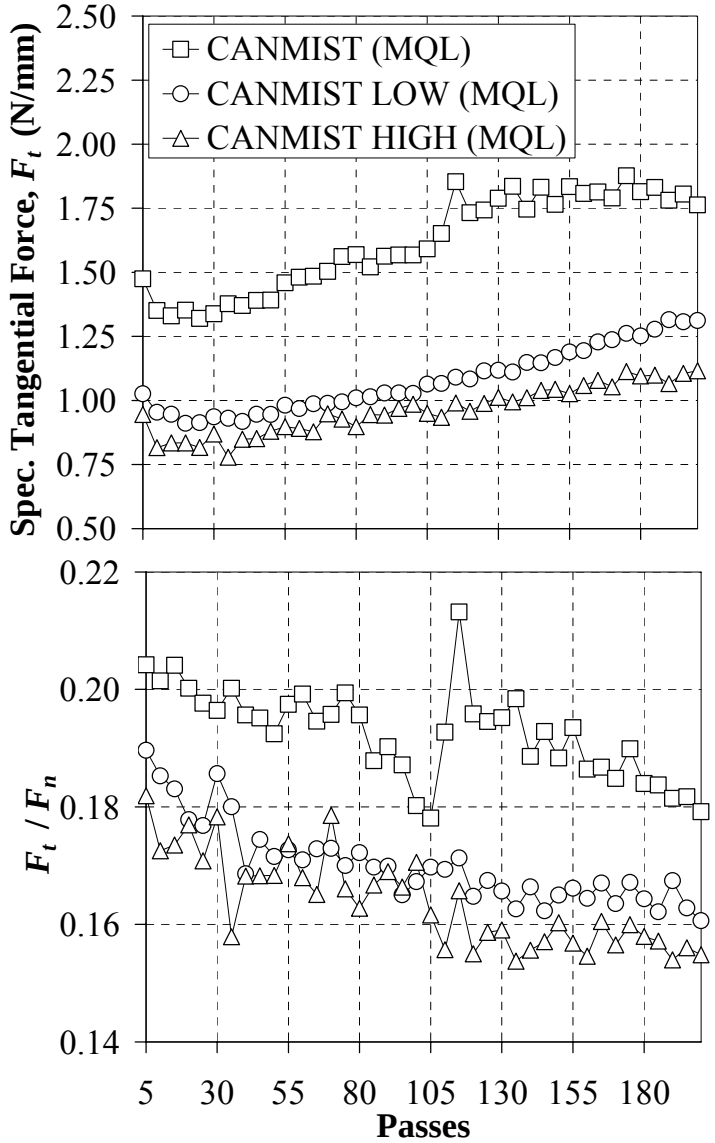

Figure 3.11. Specific tangential grinding forces & force ratio for CANMIST oil group

In the plots of specific tangential force vs. passes for all lubricants, it can be seen that the value of the force increases with increased number of passes except for pure paraffin oil. This variation in data was caused by the increased wheel wear with increased number of grinding passes. The decrease in force values for pure paraffin oil after 170 passes seems to be unusual and will be subjected to further tests for verification,

in future research. High pressure and temperature, generated during surface grinding, do not allow lubricants to flow smoothly and uniformly in the interface. Penetration of liquid (and thus, nanoparticles of MoS_2) and trapping of debris at machining interface are stochastic processes and vary as the wheel wears. We believe, this stochastic behavior is reflected in the variation of the presented data. Further research will take this into the account for in depth analysis.

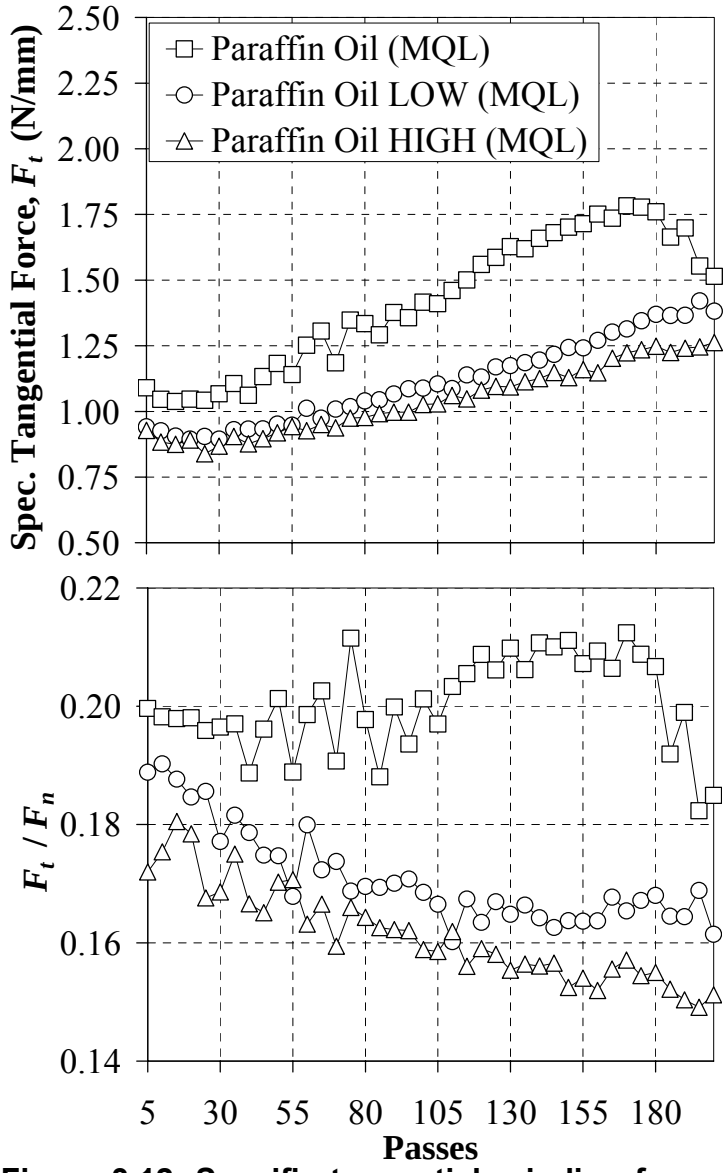

Figure 3.12. Specific tangential grinding forces & force ratio for paraffin oil group

It should also be noted that the number of grinding passes throughout the experiment was quite large (200 passes). Under such conditions, tangential grinding force and force ratio values of MQL grinding with $nMoS_2$ based lubricants seems to be far better than those of base fluids and flood lubrication.

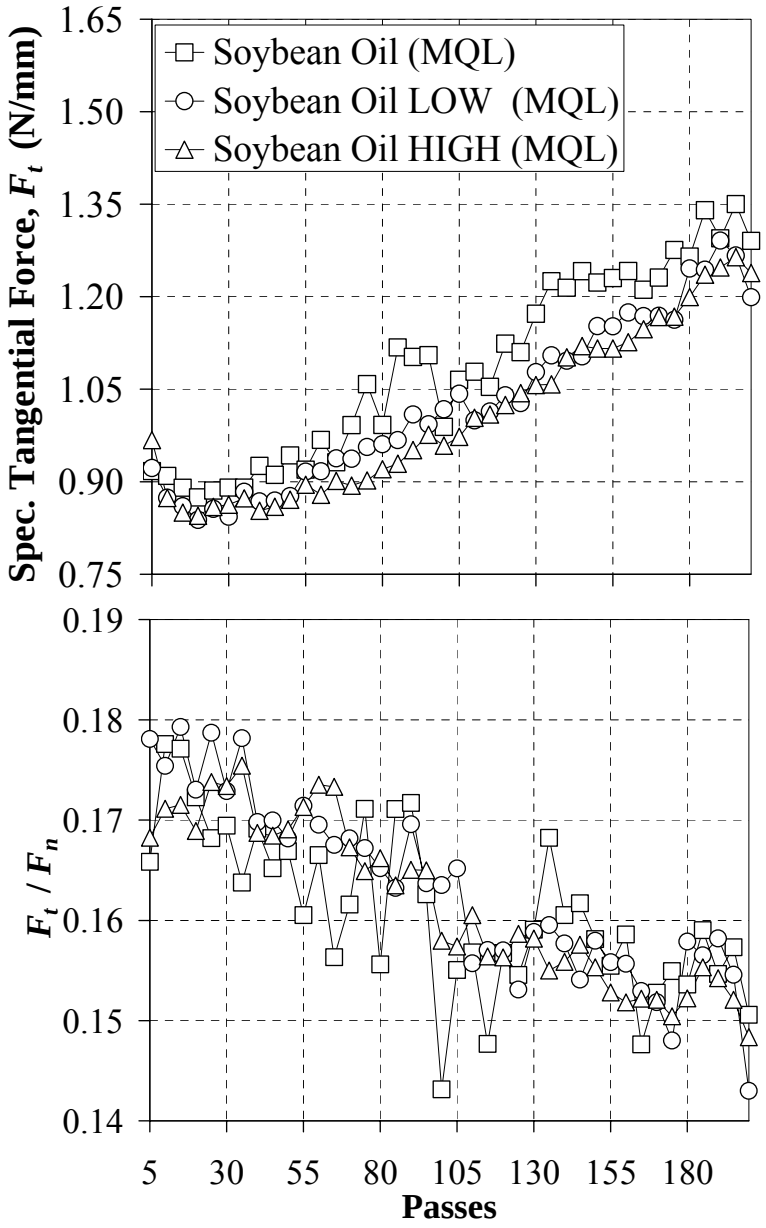

Figure 3.13. Specific tangential grinding forces & force ratio for soybean oil group

The above observed characteristic behaviors of $nMoS_2$ based lubricants, namely, enhanced penetration and entrapment at grinding interface, formation of tribofilm, base fluid chemistry and effects of concentration of MoS_2 nanoparticles on MQL grinding performance will be analyzed in depth in future research.

3.3.4. G-ratio

Wheel life in grinding process is expressed in terms of grinding ratio or G-ratio and is defined as the volume of material removed per unit volume of grinding wheel wear. Wheels with a high G-ratio last longer than those with lower G-ratios (Krueger et al., 2000). The grinding wheel wear occurs due to the friction between the abrasive grains and the workpiece. High fluid lubricating capacity reduces the wear on the grinding wheel by decreasing grain-workpiece friction, allowing the abrasive grains to remain bound to the binder for longer periods and leading to lower wear of the tool (Silva et al., 2005).

The G-ratio results for all the grinding experiments are shown in Figure 3.14. All the MQL grinding operations with pure oil based fluids have much higher G-ratio (ranging from 28 to 42) than flood cooling with water-based Cimtech 500 synthetic grinding fluid. This can be attributed to the excellent lubricating capacity of oil based fluids and to the good lubricating conditions provided by MQL, which give much lower grinding forces as discussed in previous section.

It is important to note that G-ratio is higher for high concentration of $nMoS_2$ additive conditions for all the base oils, including soybean oil. We believe that this can be explained by the reduction in grinding forces with $nMoS_2$ additives, thereby, ensuring

the retention of grit sharpness due to less wear and lower plastic deformation at reduced temperature. The most significant improvement can be seen in CANMIST oil based fluids. Both the CANMIST oil based lubricants, with high and low concentration of $nMoS_2$ gave a high G-ratio value compared to that of pure CANMIST oil. It is important to bring out that the effect on tangential grinding forces for pure versus additive contained soybean oil are miniscule, however G-ratios are distinctively higher and we continue to believe that this will be one of the future areas of research.

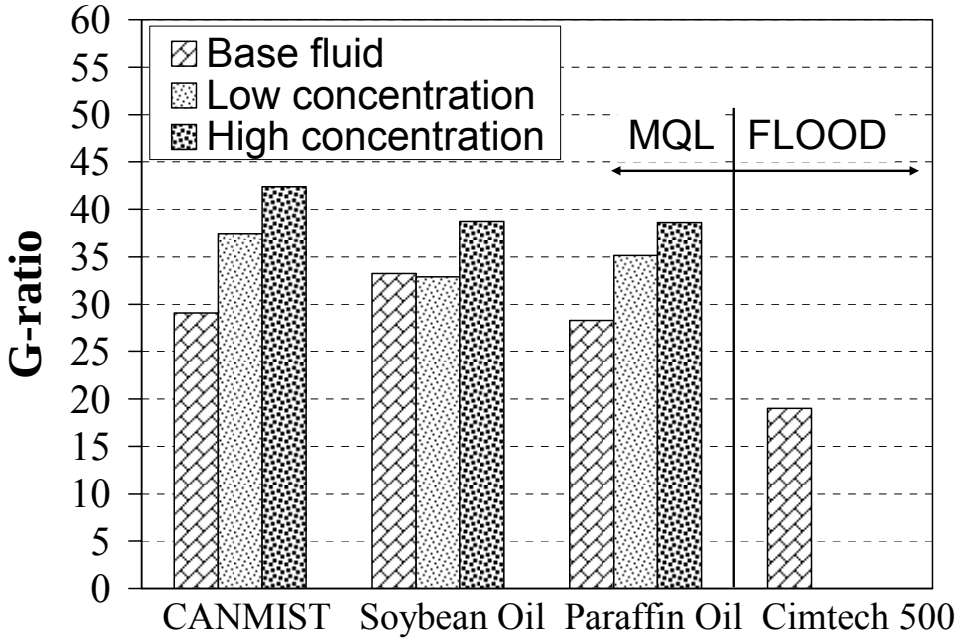

Figure 3.14. G-ratio results

3.3.5. Surface Finish

The arithmetic average surface roughness (R_a) results for all the grinding experiments are presented in Figure 3.15. Flood cooling has the lowest surface roughness. This is probably due to the chip flushing nature of food cooling, which reduces the grinding wheel and prevents the scratching of the workpiece surface. Among

all the pure oils, soybean oil has the best surface finish, possibly due to the lower tangential grinding forces (less rubbing and plowing).

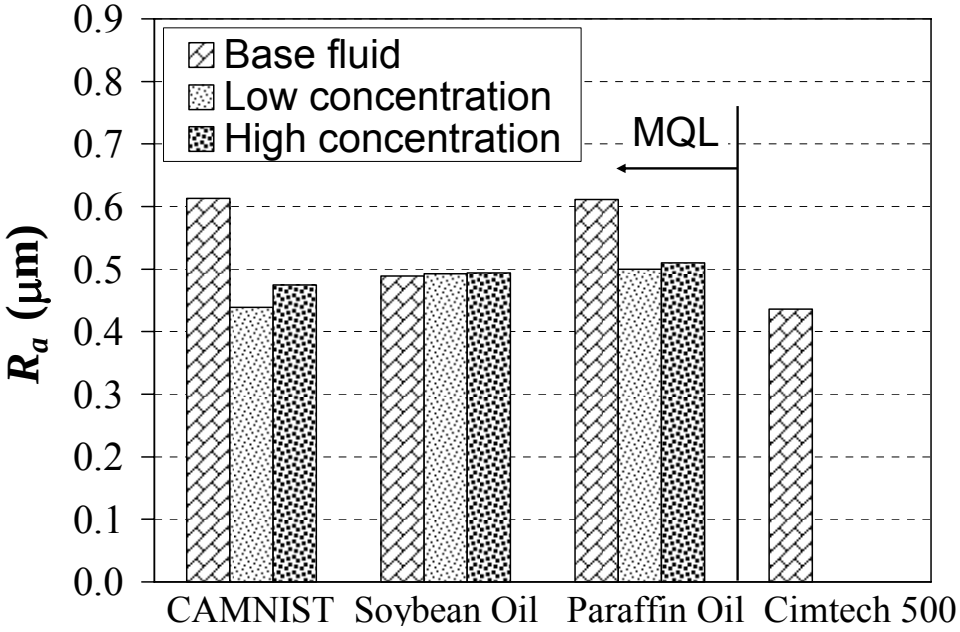

Figure 3.15. Surface finish results

For both groups of CANMIST and paraffin oils, MoS_2 nanoparticle additives can significantly improve the surface finish. This is because CANMIST and paraffin oil based nano-lubricant can achieve lower tangential grinding forces, less friction between the wear flats and the workpiece, and less wheel wear (higher G-ratio). However, the high concentration MoS_2 nanoparticles affect the surface finish negatively compared to low concentration ones, probably due to the increasing wheel loading.

For the group of soybean oil, the MoS_2 nanoparticle additives virtually have no influence on the surface finish. This is actually consistent with grinding forces, force ratio and G-ratio results presented in the previous sessions. The only noticeable improvement in G-ratio with the high concentration MoS_2 nanoparticles is offset by the possible higher wheel loading, leading to hardly any changes in workpiece surface finish.

3.3.6. Summary

It is shown for the first time that nanoparticles of MoS_2 could provide key value addition in MQL grinding, when using various off the shelf base fluids such as paraffin oil, soybean oil and CANMIST oil. Also, it is reported that the nanoparticles of MoS_2 offer unique advantages in MQL when they present the possibility of navigating in the grinding zone and delivering reduction of grinding forces (27% for CANMIST oil group, 21% for paraffin oil based group and 9% for soybean oil group), and most distinctively increase life of expensive grinding wheels by increasing G-ratio (46% for CANMIST oil group, 35% in paraffin oil group and 15% in soybean oil group). Superior grinding performance with minimum application of MoS_2 based lubricants (5 ml/min compared to 5400 ml/min application in flood cooling) shows its cost-effectiveness. In addition, MoS_2 nanoparticle additives can improve the surface roughness (except for soybean oil group). However, compared to flood cooling, MQL still has problems of inefficient ship flushing, resulting in poorer surface finish.

Overall, this research presents a significant opportunity for fundamental science and sustainable engineering solution for MQL grinding and needs further investigation.

3.4. Micro-scale Mechanism of MQL Grinding using Nanofluids

Material removal during grinding occurs as abrasive grains interact with the workpiece material. Malkin (1989) proposed a grinding force model, reasoning that the grinding forces can be considered to consist of cutting and sliding components. The cutting component has two mechanism involved: (1) chip-formation, which is the actual material removal process, and (2) plowing, which is the deformation of workpiece

material without removal. It can be considered as the side flow of material from the cutting path to the ridges (plastic deformation). The sliding component is contributed to the dulled flattened tips on the abrasive grains sliding against the workpiece surface without removing any material.

Good lubrication in the grinding zone can largely reduce the sliding forces. The lubricating properties of solid lubricant such as MoS_2 are attributed to a layered structure on the molecular level with weak bonding between layers. Such layers are able to slide relative to each other with minimal applied force, thus resulting in low friction properties. In MQL grinding using oil based nanofluids, it is believed that the suspended MoS_2 nanoparticle additives can navigate at the machining interface to yield and scarify for delivering a tribofilm to provide selective lubrication at tool-workpiece interface and the transient (explosive) evaporation of oil molecules overcoated on the nanoparticles acting as an effective vehicle for heat transfer, and as a result significantly reduce frication.

3.5. Concluding Remarks

In this chapter, MQL grinding (conventional abrasive wheels) of cast iron using water based and oil based nanofluids was investigated. Grinding performance is evaluated and compared in terms of grinding force, G-ratio, and surface roughness, etc.

Water-based Al_2O_3 and diamond nanofluids were applied in MQL grinding process and the grinding results were compared with those of pure water. Dispersion of solid particles was found to play an important role, especially when a slurry layer was formed. The slurry layer generated higher G-ratio (less wheel wear), smaller grinding forces and better surface finish. Experimental results showed that G-ratio, defined as the

volume of material removed per. unit volume of grinding wheel wear, could be improved with high concentration nanofluids. MQL grinding showed that it could significantly reduce the grinding temperature compared to dry grinding. However, there is no significant difference in grinding temperature when using nanofluids. It was further concluded that nanofluids are not able to provide superior cooling capacity in MQL grinding process. Thus, it was suggested that the future research of MQL grinding using nanofluids should focus on the advanced lubrication properties instead.

The tribological behavior and performance of oil based cutting fluids with novel molybdenum disulphide (MoS_2) nanoparticle additives in MQL grinding were also studied. It is shown for the first time that MoS_2 nanoparticle additives can offer unique advantages in MQL, that is, reducing grinding forces, increasing G-ratio, and improving the surface finish (compared to that of base fluids except for soybean oil group). However, compared to flood cooling, MQL still has problems of inefficient ship flushing, resulting in poorer surface finish. The experimental results further imply that it is possible to improve the tribological properties of the cutting fluids by adding lubricating nanoparticles, and consequently to enhance the performance of MQL grinding.

CHAPTER 4

GRINDING TEMPERATURE MEASUREMENT AND ENERGY PARTITION

A new thermocouple fixating method for grinding temperature measurement is presented. Unlike the conventional method using a welded thermocouple, this new method uses epoxy for affixing the embedded thermocouple within a blind hole in the workpiece subsurface. During grinding, the thermocouple junction is exposed and bonded to provide direct contact with the ground surface by the smearing of workpiece material. Experiments were conducted to evaluate this simplified thermocouple fixating method including the effect of thermocouple junction size. Heat transfer models were applied to calculate the energy partition for grinding under dry, wet, and MQL conditions.

For shallow-cut grinding of cast iron using a vitreous bond aluminum oxide wheel, the energy partition, ratio of the energy entering the workpiece, using a small wheel depth of cut of 10 μm was estimated as 84% for dry grinding, 84% for MQL grinding, but only 24% for wet grinding. Such a small energy partition with wet grinding can be attributed to cooling by the fluid at the grinding zone. Increasing the wheel depth of cut to 25 μm for wet grinding resulted in a much bigger energy partition of 92%, which can

be attributed to fluid film boiling and loss of cooling at the grinding zone.

When using vitrified bond CBN wheel, the energy partition was estimated as 68% for dry grinding, 54% for MQL grinding, and 13% for wet grinding. Experimental results showed that the insufficient cooling problem of MQL grinding is not as significant using the vitrified CBN wheel, which makes the MQL grinding feasible in the high volume production.

4.1. Introduction

As mentioned in Chapter 1, the grinding process generates a very high input of energy per unit volume of work-material removed. Virtually all the energy is converted to heat, which can cause high workpiece temperature and related thermal damage such as grinding burn, phase transformation, tensile residual stresses, surface cracks, reduced fatigue strength, thermal distortion and inaccuracies (Malkin, 1989). Therefore, heat transfer in grinding is of significant importance.

Experimental investigations of heat transfer in grinding require accurate temperature measurements. Methods for temperature measurement in grinding include thermal imaging (Sakagami et al., 1990; Hwang et al., 2004), optical fiber (Ueda, 1986; Ueda and Sugita, 1992; Curry et al., 2003), foil/workpiece (single pole) thermocouple (Rowe et al., 1996; Xu et al., 2003; Huang and Xu, 2004; Batako et al., 2005; Lefebvre et al., 2006), and embedded (double pole) thermocouple (Littman and Wulff, 1995; Kohli et al., 1995; Guo et al., 1999; Xu and Malkin, 2001; Upadhyaya and Malkin, 2004; Kim et al., 2006). The embedded thermocouple method is the most widely used of these techniques because of its relative simplicity, low cost, accuracy, and reliability. With this

method, a double pole thermocouple is welded to the bottom of a blind hole drilled close to the ground surface from the underside of the workpiece (Guo et al., 1999; Upadhyaya and Malkin, 2004). Welding the small tip of a double pole thermocouple at the bottom of the small hole requires special discharge welding equipment and skills. During grinding, the thermocouple measures the temperature below the workpiece surface during successive passes until the welded junction is broken by the grinding action. Accurately determining the position of the temperature measurement below the surface being ground is complicated by its size and also the blind hole. Furthermore the embedded thermocouple and the hole can disturb the local temperature field. Therefore it is desirable to make the thermocouple and hole very small.

The present investigation was undertaken to evaluate a simpler embedded thermocouple method for grinding temperature measurement which uses epoxy instead of welding to affix the thermocouple at the bottom of the blind hole. During grinding the thermocouple junction is exposed and bonded to the workpiece by smearing of the workpiece material, thereby providing direct contact with the workpiece surface and a direct temperature measurement at the workpiece surface. The proposed grinding temperature measurement method was then used to study the energy partition for dry, wet (flood cooling), and MQL grinding.

On the other hand, to reduce the energy partition to the workpiece, and overcome the problem of insufficient workpiece cooling, CBN wheels are considered for MQL grinding. CBN grains have very high thermal conductivity, which enhances heat conduction away from the grinding zone to the wheel (Lavine et al., 1989; Upadhyaya and Malkin, 2004). For conventional shallow-cut grinding of steels with Al_2O_3 wheels,

energy partition has been typically found to range from 60% to 85% (Malkin, 1989; Kohli et al., 1995). While significantly lower energy partition values of about 20% were found for grinding with a resin bond CBN wheel (Kohli et al., 1995). Furthermore, with a porous vitrified CBN wheel, much lower energy partition values of only 3% to 8% were reported by Guo et al. (1999) and Varghese et al. (2000). This additional reduction in the energy partition, beyond what was obtained with the resin bond CBN wheel, was attributed to cooling at the grinding zone by fluid entrapped in the wheel pores (Upadhyaya and Malkin, 2004). Although CBN wheels are widely used in industrial production, there is limited research in CBN MQL grinding (Silva et al., 2005).

In the first part of this chapter, the new thermocouple fixating method for grinding temperature measurement was first investigated. The experiments were conducted which compare the performance of epoxy fixated thermocouples with that of welded thermocouples. In the second part, MQL grinding performance of the vitrified CBN wheel using soybean oil, and soybean carbon nanotube (CNT) additives was studied. The experimental results including grinding forces, surface finish, grinding temperature and especially the energy partition are presented.

4.2. Thermocouple Fixating Method for Grinding Temperature Measurement

4.2.1. Grinding Test Setup

Straight surface plunge grinding experiments (no crossfeed) were conducted on an instrumented Chevalier Model Smart-B818 surface grinding machine using the setup shown in Figure 4.1. The grinding wheel was vitreous bonded aluminum oxide (Saint-Gobain/Norton 32A46-HVBEP) of initial diameter d_s=177.8 mm and width b_s=12.7 mm.

The workpiece material was Dura-Bar 100-70-02 ductile iron with a carbon content of 3.5-3.9%, hardness 50 Rockwell C, thermal conductivity 63 W/m·K, and thermal diffusivity 1.63×10^{-7} m^2/s. The workpieces were of length 58 mm in the grinding direction and width b_w=6.5 mm corresponding to the grinding width. Experiments were conducted without fluid (dry), under wet (flood) application conditions, and with Minimum Quantity Lubrication (MQL). The same fluid (5 vol% Cimtech 500 synthetic grinding fluid in water) was used both for MQL and flood application. MQL application utilized a special fluid deliver system provided by AMCOL, as mentioned in Chapter 3. The flow rate was 5400 ml/min for flood (wet) grinding, but only 5 ml/min for MQL.

All experiments were conducted in the down mode with the wheel and workpiece velocities in the same direction at the grinding zone (Figure 4.1). The wheel velocity was v_s=30 m/s. Two sets of grinding parameters were used: fine grinding with a workpiece velocity of v_w=2.4 m/min and depth of cut a=10 μm, and more aggressive grinding with v_w=3.0 m/min and a=25 μm. Prior to each grinding experiment, the wheel was dressed by taking a minimum of 15 passes across the rotating wheel using a rotary diamond disk dresser with a diameter of 96 mm and width of 3.8 mm (provided by Saint-Gobain) in the up mode with a speed ratio (ratio of peripheral dresser velocity to wheel velocity) of −0.4, a radial depth of 10 μm, and a traverse velocity of 500 mm/min. During grinding, the normal and tangential grinding force components were measured using a Kistler Model 9257A piezoelectric dynamometer, and the temperature was measured using an epoxied or welded thermocouple, as shown in Figure 4.1(b). Both grinding force and temperature data were collected simultaneously at a 5 kHz sampling rate. The workpiece was allowed to cool down completely after each grinding pass.

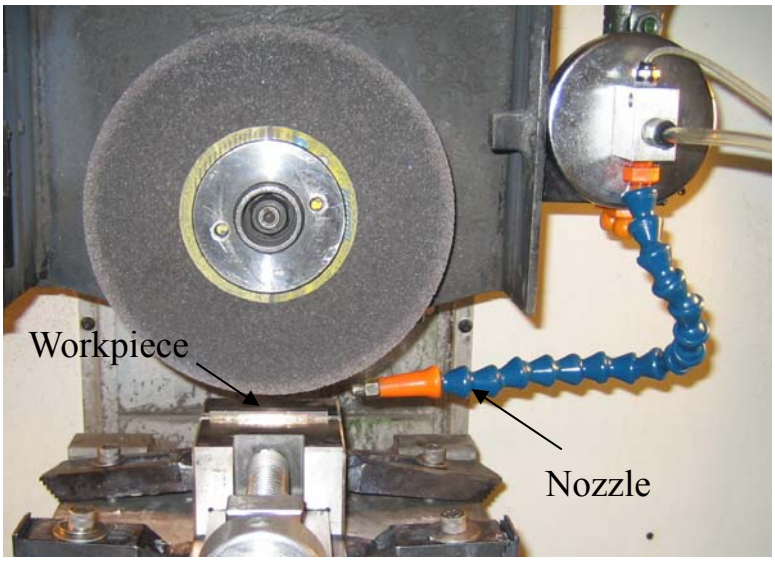

(a)

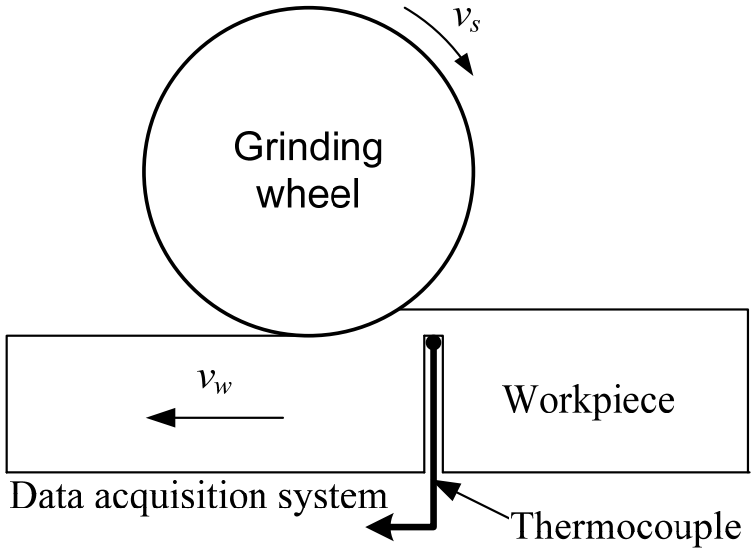

(b)

Figure 4.1. Experimental setup: (a) overview of the setup and (b) schematic drawing of grinding temperature measurement

4.2.2. Thermocouple Fixating

Most experiments were conducted with expoxied thermocouples which were affixed to the bottom of a blind hole using a high temperature epoxy (Permabond 920). Both 30 and 46 gage type K thermocouples were used to investigate the effect of junction

size. The junction diameter was 0.60−0.80 mm for the 30 gage thermocouple and 0.20−0.25 mm for the 46 gage thermocouple. A blind hole was drilled from the underside of the workpiece to within 1−2 mm of the workpiece surface by electrical discharge machining (EDM) with a tubular electrode. The hole diameter was 0.8 mm for the 30 gage thermocouples and 0.3 mm for the 46 gage thermocouples. The tubular EDM electrode left a knob at the bottom of the blind hole, as shown in the cross-sectional view in Figure 4.2(a), which made it difficult to affix the thermocouple. Therefore EDM with a solid electrode of smaller diameter was subsequently used to remove the knob and create a tapered concave pocket as shown in Figure 4.2(b). Figure 4.3(a) shows a cross-section of the 30 gage thermocouple junction inside a 0.8 mm diameter hole.

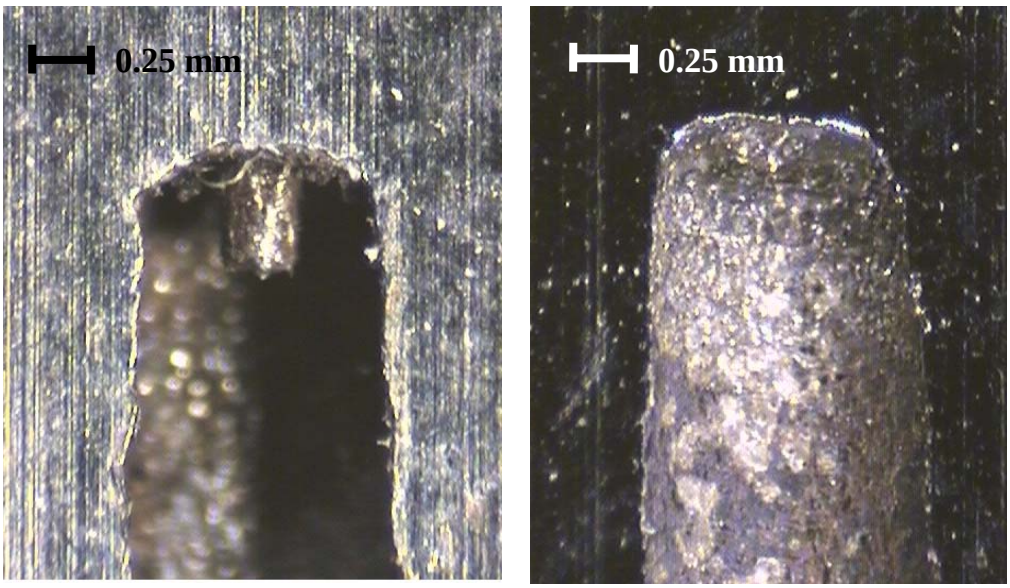

Figure 4.2. Cross-section view of blind hole tips: (a) EDM drilled using a tubular electrode and (b) EDM modified using a solid electrode

During grinding, the thermocouple junction is exposed (Figure 4.3(b)) and the deformed workpiece connects the thermocouple junction to the workpiece (Figure 4.4(a))

for temperature measurement. The thermocouple was grounded in order to reduce noise and avoid the electric charge produced by the mechanical contact. The time constant of the embedded thermocouple was on the order of 1 ms (Xu and Malkin, 2001). Whether this response time is sufficiently fast may be ascertained by comparing to the characteristic time it takes for a point on the workpiece surface to pass through the grinding zone, which can be obtained as the contact length l_c ($=\sqrt{d_s a}$) divided by the workpiece velocity v_w (Xu and Malkin, 2001). In this study, the characteristic time was estimated as 33 ms, which is more than an order of magnitude bigger than the time constant of the embedded thermocouple.

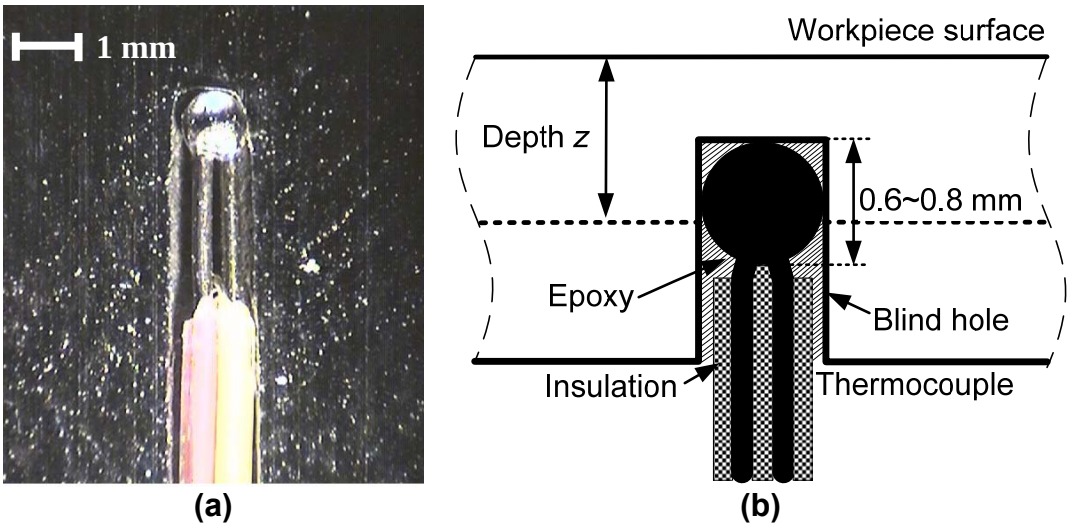

Figure 4.3. Illustration of thermocouple fixating: (a) cross-section view and (b) schematic drawing

The sizes of the hole and thermocouple junction need to be closely matched. If the hole is too large, a good connection between the thermocouple junction and workpiece is not obtained, as seen in Figure 4.4(b). It will be seen that this can adversely affect the temperature measurement.

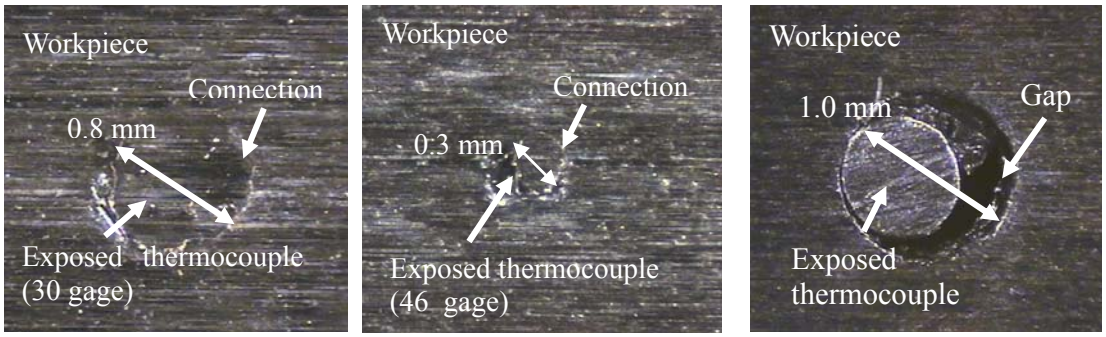

(a) **(b)**

Figure 4.4. Illustration of thermocouple fixating: (a) closely matched thermocouple tip and hole with good connection and (b) large hole leading to a gap surrounding the thermocouple tip

A calibration test was conducted to verify that the epoxied thermocouple still works even after part of the junction has been ground away. For this purpose, the ground thermocouple and workpiece assembly shown in Figure 4.4 was submerged in ice-water and in boiling water. Accurate temperature measurements were obtained.

For comparison, experiments were also conducted using welded thermocouples (Figure 4.5). Welded thermocouples require a larger junction and a bigger hole than epoxied thermocouples, which is a definite disadvantage. Furthermore, a welded thermocouple usually breaks just as it begins to become exposed during grinding, so the maximum temperature is actually measured slightly below the ground surface. Accurately determining the temperature at the workpiece surface with a welded thermocouple is usually done by extrapolation of subsurface temperature measurements to the surface (Guo and Malkin, 1996a). By contrast, an epoxied thermocouple maintains direct contact with the workpiece surface as the junction is ground, thereby providing a direct measurement of the surface temperature (Figure 4.4(a)).

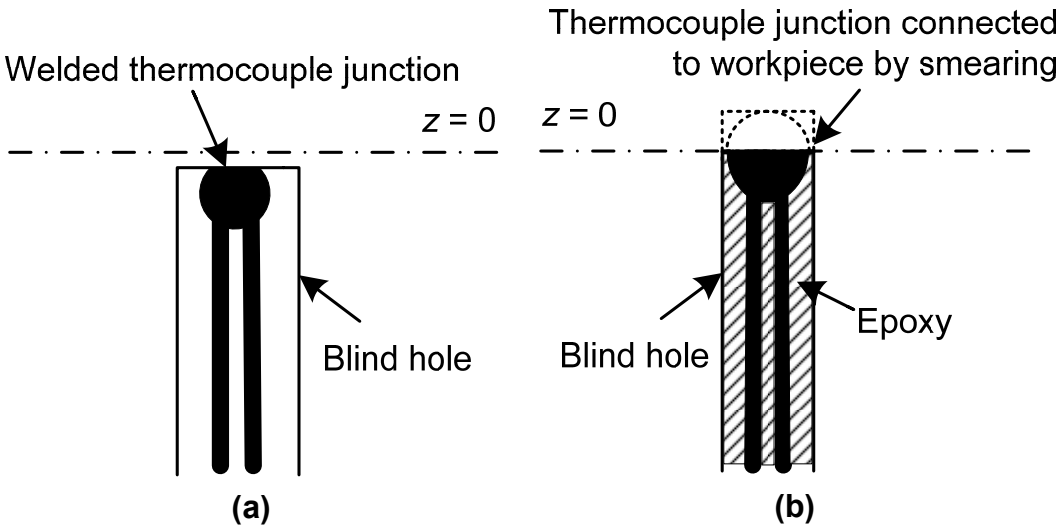

Figure 4.5. Difference between (a) welded thermocouple and (b) epoxied thermocouple

4.2.3. Experimental Design

Grinding conditions for all experiments are listed in Table 4.1. Experiments with welded thermocouples are designated as Exp. W. From eight sets of experiments with epoxied thermocouples, four marked as Exps. E1, E2, ES1, and ES2, were conducted for the same grinding conditions as with the welded thermocouples. For ascertaining the effect of junction size, smaller 46 gage thermocouples were used in Exps. ES1 and ES2. All the other experiments were conducted using 30 gage thermocouples. One test, Exp. E3, was conducted with an epoxied thermocouple placed in an oversized hole, as seen in Figure 4.4(b), to identify the effect of hole diameter on the temperature measurement. Experiments EW1 and EW2 refer to wet grinding using different parameters. Experiment EM was with MQL.

Table 4.1. Experimental matrix design

Experiment designation	W	E1	E2	E3	ES1	ES2	EM	EW1	EW2
Fixturing method	Welded	Epoxied							
Thermocouple wire gage	30	30	30	30	46	46	30	30	30
Depth of cut (μm)	10								25
Workpiece velocity (m/min)	2.4								3
Grinding fluid flow rate (ml/min)	N/A (dry)						5	5400	

4.2.4. Temperature Rise

During grinding, both the welded and epoxied thermocouples measure the temperatures at a distance z below the workpiece surface (Figure 4.3(b)). Temperature measurements with the epoxied thermocouple in Figure 4.6 show the peak temperature rise for each subsequent grinding pass progressively increasing until the thermocouple is fully exposed (Figure 4.4(a)) and the connection between the thermocouple junction and workpiece is established. At this point the peak temperature rise is reached, and it remains nearly constant for a number of additional grinding passes. The location of the reference surface at z=0 can be defined by where this steady-state period begins, as illustrated in Figure 4.6. The steady-state period in Figure 4.6 persists for more passes with the bigger 30 gage thermocouple than with the smaller 46 gage thermocouple.

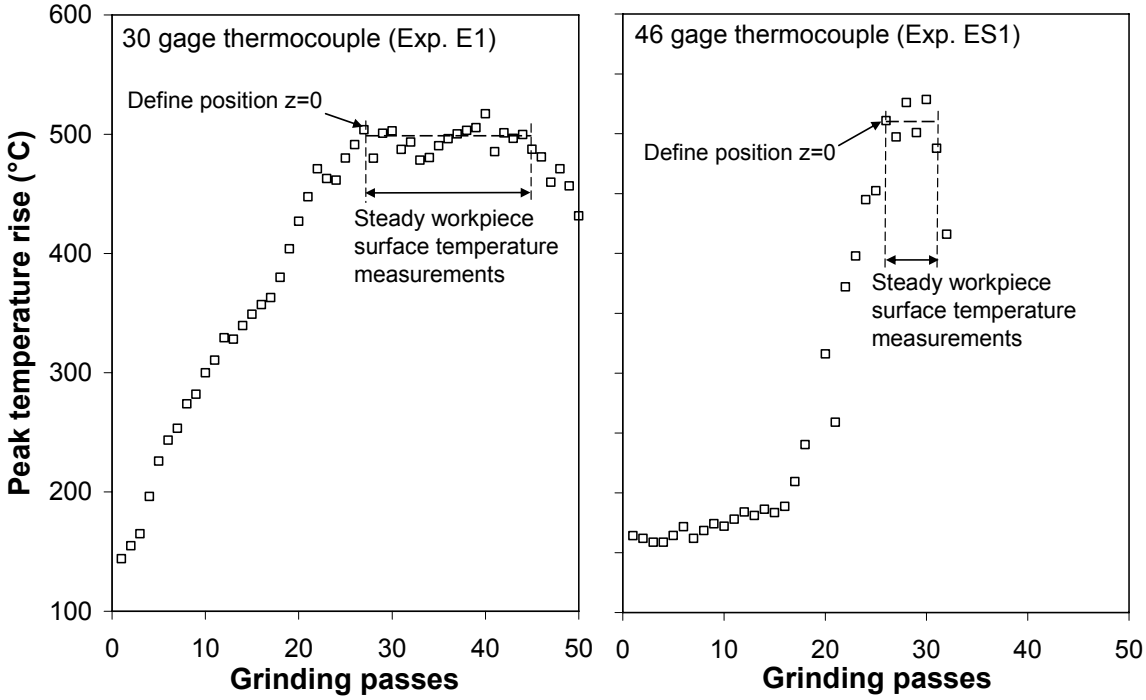

Figure 4.6. Peak temperature rise vs. grinding passes for epoxied thermocouple method

For a welded thermocouple, the reference of z=0 is usually defined at the position where the thermocouple begins to be exposed and the maximum peak temperature rise is measured. However, this peak temperature probably occurs slightly below the surface since the next grinding pass usually damages the welded connection between the thermocouple and the workpiece.

Measured temperature rises for dry grinding conditions are presented in Figure 4.7. For all experiments, the peak temperature is bigger closer to the surface at smaller depth z. Note that when the thermocouple is further down below the ground surface ($z \geq 0.2$ mm), the temperature measured using the welded thermocouple (Exp. W) decreases faster than the temperature measured using the epoxied thermocouple, which suggests poor thermal contact. When grinding at the surface where z=0, good contact is obtained between the workpiece surface and epoxied thermocouple (see Figure 4.4(a)).

This can explain why the maximum temperature measured using an epoxied thermocouple is higher than for the welded thermocouple under the same grinding conditions, except for Exp. E3 (small thermocouple in large hole) where a gap exists between the thermocouple junction and the workpiece (Figure 4.4(b)). The lower temperature measured with the welded thermocouple is a further indication that its maximum peak temperature is measured below the surface just as the junction begins to be exposed. The data obtained with the smaller 46 gage thermocouples in Exps. ES1 and ES2 generally show a faster response as well as a faster cooling rate than with the bigger 30 gage thermocouples in Exps. E1, E2 and E3. This can be attributed to reduced size and lower thermal inertia.

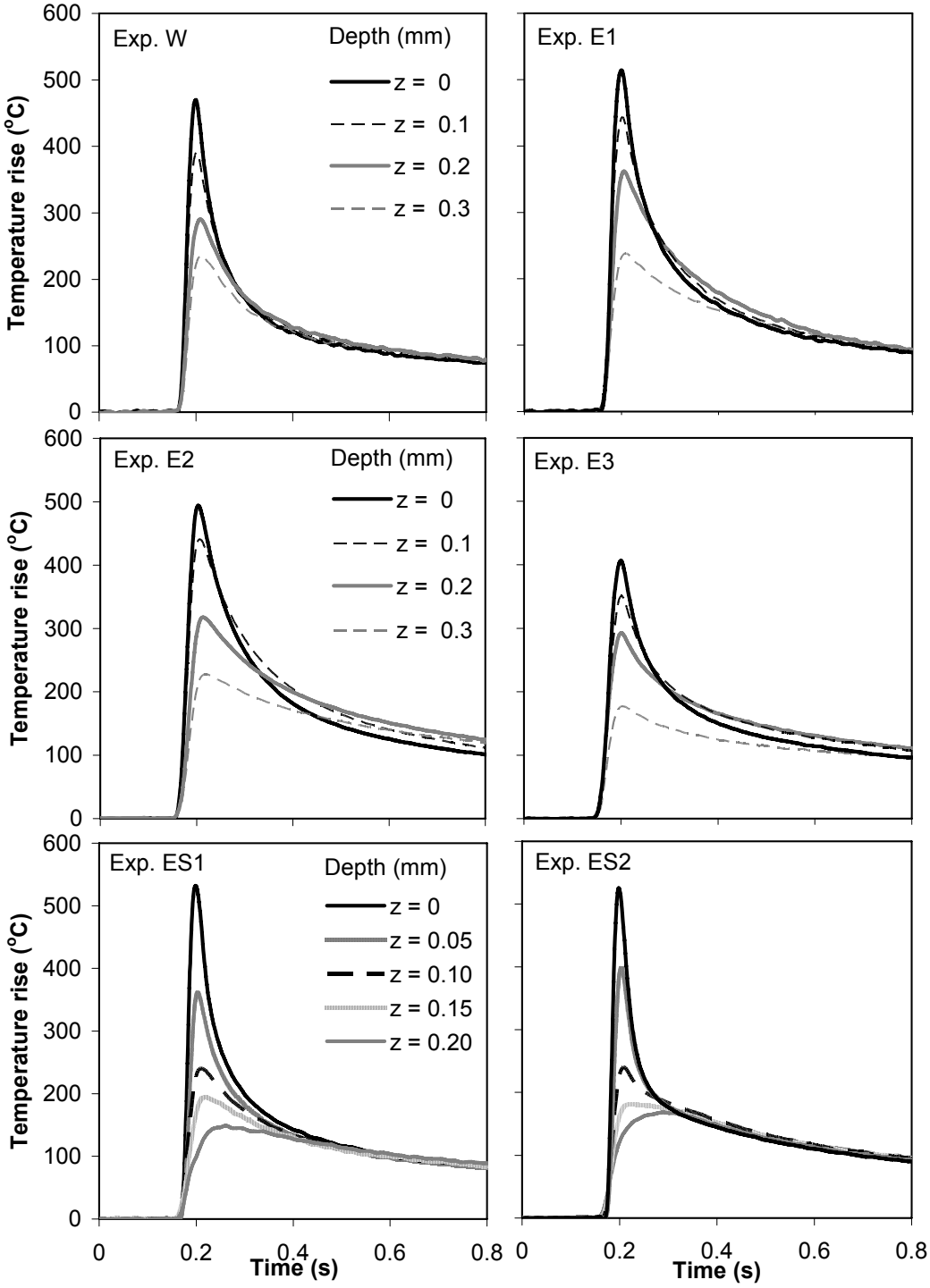

Figure 4.7. Temperature rise at different depth in dry grinding: Exp. W with welded thermocouple (30 gage), Exps. E1, E2, and E3 with epoxied thermocouple (30 gage), and Exps. ES1 and ES2 with epoxied thermocouple (46 gage)

A comparison of grinding temperatures measured at the surface (z=0) under dry conditions is presented in Figure 4.8. The peak temperature rises for Exps. E1 and E2 are almost identical at 500°C. The peak temperature rises for Exps. ES1 and ES2 (smaller 46 gage thermocouples) are slightly higher, 525°C and 511°C, respectively, which can again be attributed to the smaller junction size. The welded thermocouple (Exp. W) gives a lower peak temperature rise (469°C), apparently because of its larger size and also damage to the weld joint, as described above. Also the welded thermocouple requires a larger hole diameter (1.5 mm) for electrical insulation, which could also lower the measured temperature. For Exp. E3 with the bigger hole, the thermal connection is not formed (Figure 4.4(b)) and the measured peak temperature is much lower (405°C).

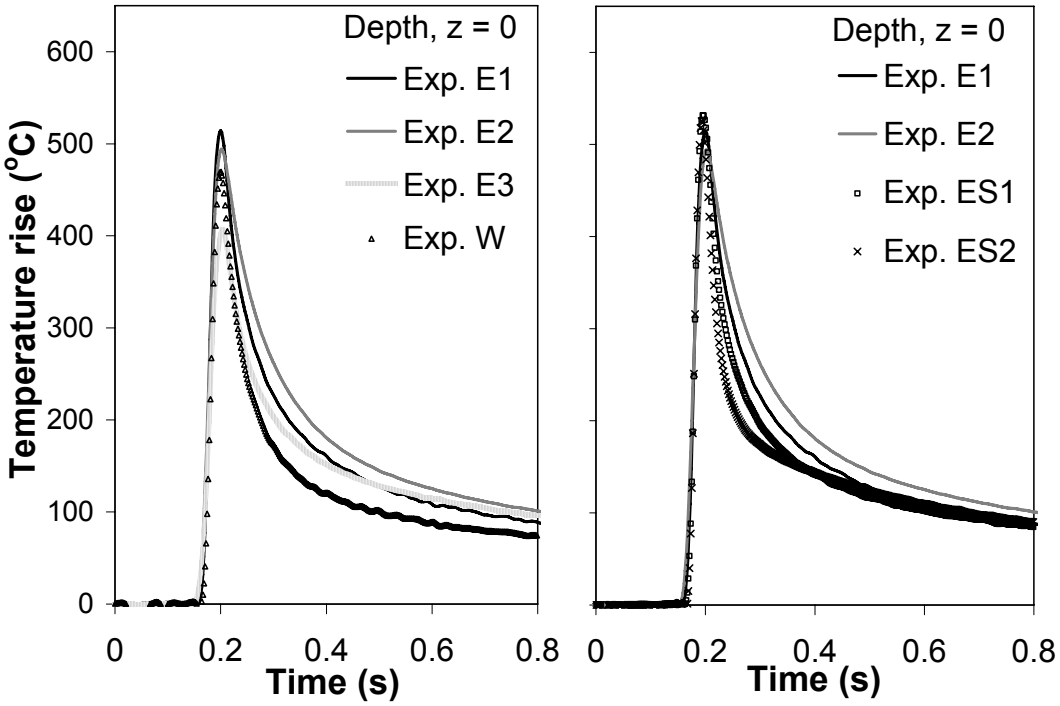

Figure 4.8. Measured grinding temperature at the workpiece surface at depth z=0 (dry condition)

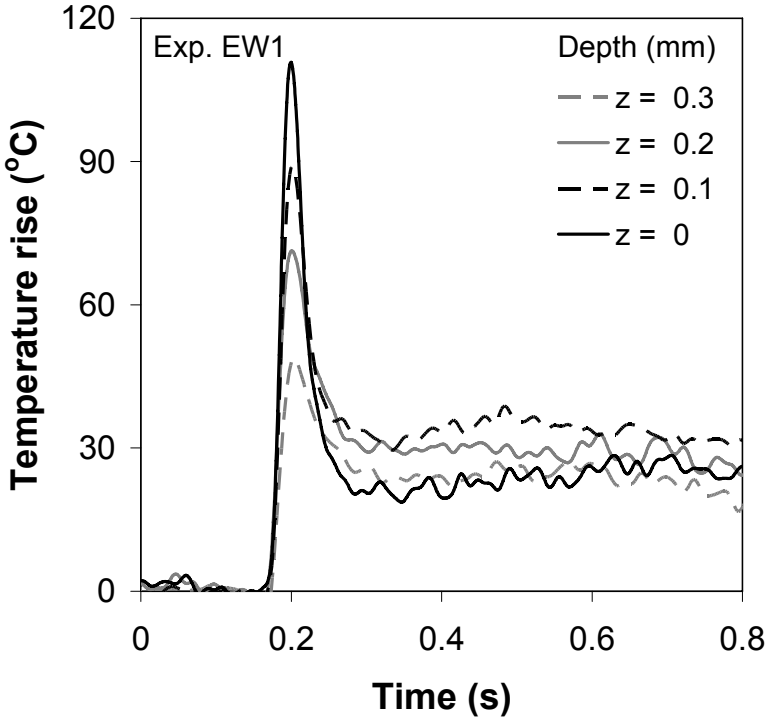

(a)

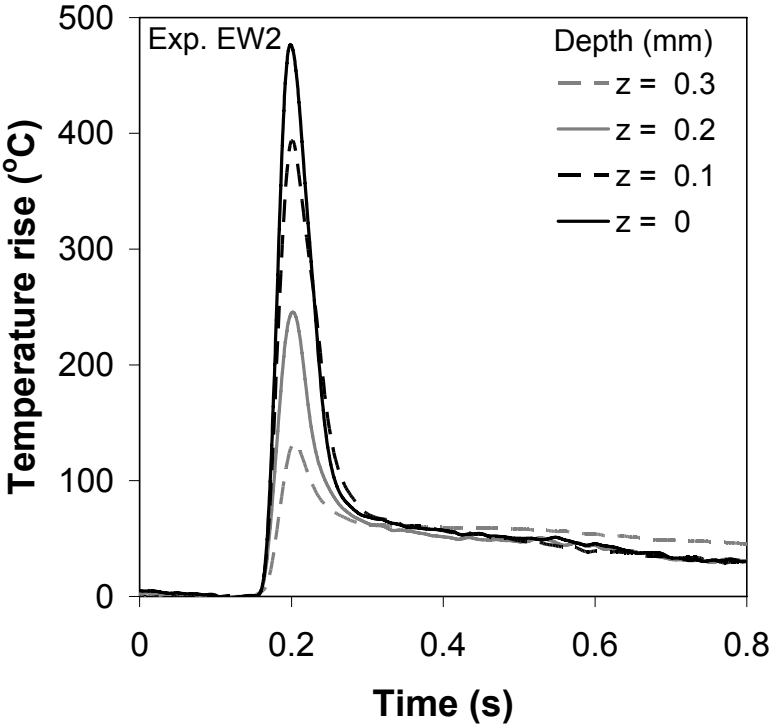

(b)

Figure 4.9. Temperature rise in wet grinding, different grinding conditions: (a) depth of cut, a=10 μm and workpiece velocity, v_w=2.4 m/min, and (b) a=25 μm and v_w=3 m/min

Experiment EW1 was conducted under wet conditions with the same grinding parameters as in dry grinding, but the maximum temperature rise of 106°C (Figure 4.9(a)) was much lower. This temperature rise is comparable to or slightly less than the film boiling temperature of the water-based grinding fluid. In the absence of film boiling, the grinding fluid should provide significant cooling at the grinding zone, which is usually much more likely with creep feed grinding than with conventional shallow cut grinding (Fuh and Huang, 1994). In another wet grinding test Exp. EW2 under more aggressive conditions (v_w=3 m/min and a=25 μm), the peak temperature rise (474°C) greatly exceeded the film boiling temperature of the grinding fluid.

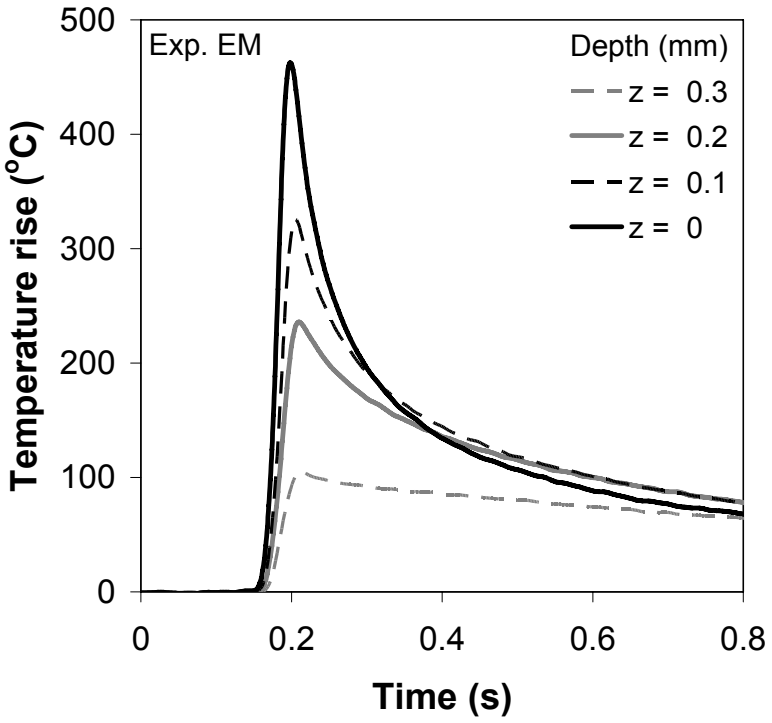

Figure 4.10. Temperature rise at different depths in MQL grinding (grinding fluid flowrate = 5 ml/min)

The temperature rise for Exp. EM with MQL is shown in Figure 4.10. The peak temperature rise of 444°C is about 60°C lower than for dry grinding (see Figure 4.8).

This lower temperature can be attributed, at least in part, to lubrication by MQL, which reduced the average tangential grinding force per unit width, F_t/b_w, from about 2.0 N/mm with dry grinding to 1.8 N/mm with MQL.

4.2.5. Energy Partition

4.2.5.1. Traditional heat transfer models

Straight surface grinding experiments were conducted as shown in Figure 4.11 where a wheel of diameter d_s rotating with a peripheral velocity v_s removes a depth a of material from the workpiece as it passes under the wheel at velocity v_w. Virtually all the grinding energy expended at the grinding zone is converted to heat, which is transported to the workpiece, grinding wheel, chips and grinding fluid. The geometrical grinding zone is the region of length l_c ($=\sqrt{d_s a}$) where the wheel interacts with the workpiece.

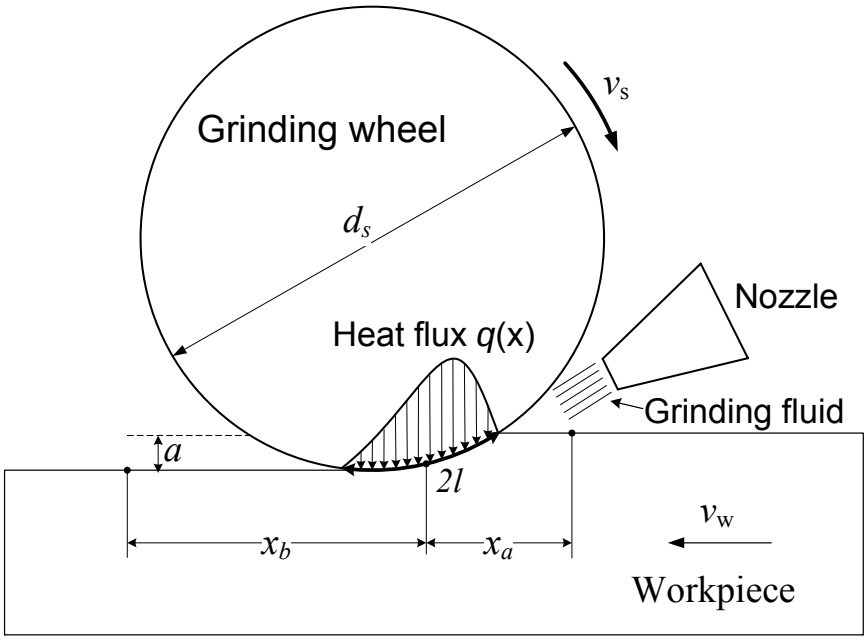

Figure 4.11. Schematic drawing of heat transfer in down grinding

The temperatures generated at the grinding zone can be calculated by considering the grinding zone as a band source of heat of length l_c which moves along the surface of the workpiece at the workpiece velocity v_w. A critical parameter for this thermal analysis is the energy partition ε, which is defined as the fraction of the grinding energy transported as heat to the workpiece at the grinding zone. Since the maximum grinding zone temperature rise θ_{max} is measured and the total energy input can be readily calculated from the tangential force measurement, the thermal analysis can be used to evaluate the energy partition which occurred for grinding using the relationships (Guo and Malkin, 1992):

$$q = \frac{k_w v_w^{1/2}}{\beta \alpha_w^{1/2} a^{1/4} d_s^{1/4}} \theta_{max} \tag{4.1}$$

$$\varepsilon = q / \frac{F_t v_s}{b_w l_c} \tag{4.2}$$

where q is the heat flux into the workpiece, k_w the workpiece thermal conductivity, α_w the thermal diffusivity of workpiece, F_t the tangential grinding force, b_w the width of the workpiece, and β a constant which depends on the heat source shape. In this study, β=1.06 for the triangular shape heat source (Guo and Malkin, 1992).

Guo and Malkin (1996a; 1996b) developed an inverse heat transfer model based on the moving heat source theory (Jaeger, 1942). For a semi-infinite body, the quasi-steady state temperature distribution $\theta_w(x,z)$ in the workpiece within a region $[x_a, x_b]$ is given by

$$\theta_w(x,z) = \int_{x_b}^{x_a} q_w(\xi)\Phi(x,z,\xi)d\xi \tag{4.3}$$

where $q_w(\xi)$ is the heat flux into workpiece, ξ a local coordinate in the x-direction, Φ a function defined as:

$$\Phi(x,z,\xi) = \frac{1}{\pi k_w} e^{-v_w(x-\xi)/2\alpha_w} K_0\left\{\frac{v_w}{2\alpha}\left[(x-\xi)^2 + z^2\right]^{1/2}\right\} \tag{4.4}$$

where K_0 is the modified Bessel function of the 2nd kind of order zero. If the region [x_a, x_b] is divided into n very small sections [ξ_i, ξ_{i+1}] of equal length, where

$$\begin{aligned} \xi_i &= x_b + \frac{x_a - x_b}{n}(i-1) \\ \xi_{i+1} &= x_b + \frac{x_a - x_b}{n} i \end{aligned} \tag{4.5}$$

The heat flux $q_w(\xi_i)$ within each section can be approximated as a constant q_i. Equation (4.3) can be rewritten as:

$$\theta_w(x,z) = \sum_{i=1}^{n} q_i \int_{\xi_i}^{\xi_{i+1}} \Phi(x,z,\xi)d\xi \tag{4.6}$$

At a depth z beneath the workpiece surface, discrete temperatures T_j were measured at n equally spaced points x_j (j=1,2,…,n) as the workpiece moves at speed v_w and the data was collected at fixed frequency. These x_j may or may not coincide with local coordinate ξ_i at the surface. Consequently, we have the following n equations:

$$\theta_w(x_j,z) = \sum_{i=1}^{n} q_i \int_{\xi_i}^{\xi_{i+1}} \Phi(x_j,z,\xi)d\xi \qquad j = 1,2,...,n \tag{4.7}$$

Substituting the n measured temperature T_j for $\theta_w(x_j,z)$ into Equation (4.7) leads to a system of n simultaneous equations:

$$\sum_{i=1}^{n} c_{ji} q_i = T_j \tag{4.8}$$

where c_{ji} are coefficients defined as:

$$c_{ji} = \int_{\xi_i}^{\xi_{i+1}} \Phi(x_j, z, \xi) d\xi \qquad i, j = 1,2,...,n \tag{4.9}$$

Equation (4.8) can also be written in the matrix form:

$$\begin{bmatrix} c_{11} & c_{12} & c_{13} & \cdot & c_{1n} \\ c_{21} & c_{22} & c_{23} & \cdot & \cdot \\ c_{31} & c_{32} & c_{33} & \cdot & \cdot \\ \cdot & \cdot & \cdot & \cdot & \cdot \\ c_{n1} & \cdot & \cdot & \cdot & c_{nn} \end{bmatrix} \begin{bmatrix} q_1 \\ q_2 \\ q_3 \\ \cdot \\ q_n \end{bmatrix} = \begin{bmatrix} T_1 \\ T_2 \\ T_3 \\ \cdot \\ T_n \end{bmatrix} \tag{4.10}$$

For a given grinding condition, coefficients c_{ji} can be numerically evaluated and thus the heat flux can be determined if the temperature profile at a particular depth z is measured. Given the heat flux distribution, the energy partition, which is the fraction of the grinding energy transported as heat to the workpiece at the grinding zone, can be found by integrating the heat flux over the entire grinding zone. Although it has the most flexibility, this method has stability problem and is very sensitive to the input temperature measurements.

On the other hand, with the assumption of heat flux shape (for example, rectangular or triangular shape), the energy partition can also be found by matching the experimentally measured temperatures with the predicted values (Equation (4.8)). This is so called "temperature matching method", and is more widely used (Kohli et al., 1995;

Guo and et al., 1999; Xu and Malkin, 2001; Upadhyaya and Malkin, 2004). In this study, the temperature method is used for energy partition calculation.

4.2.5.2. Energy partition by curve fitting

Experimental measurements of peak temperature rise versus depth z are plotted in Figure 4.12. In each case, the peak temperature rise increases closer to the surface. The inverse heat transfer model can be used to predict grinding temperature profiles at different depths. Therefore, the energy partition can be determined by matching the peak temperatures at different depth for the measured temperatures and the theoretical results. A Matlab program was developed for obtaining a least square fit. The energy partition calculated using this method is designated as $\varepsilon_{fitting}$.

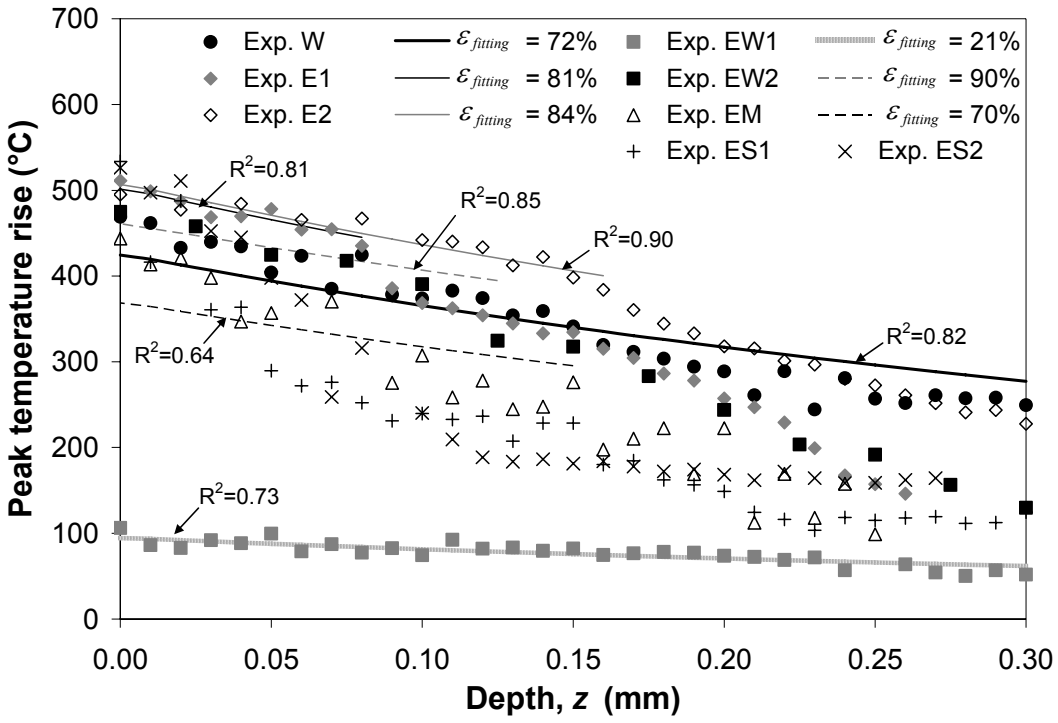

Figure 4.12. Experimental and theoretical maximum temperature rise versus the depth *z*

For the welded thermocouple (Exp. W), it was found that $\varepsilon_{fitting}$=72% using the least square fit over the entire range, as illustrated in Figure 4.12. However, the expoxied thermocouple undermeasures the temperature when it is positioned far below the workpiece surface, as discussed in the previous section. Consequently, not all the experimental data points ranging from z=0 to z=0.3 mm are appropriate for curve fitting. Therefore, the R^2 value, which determines the goodness of fit, was used to select a cutoff depth z_0, i.e., data with depth $z<z_0$, to maximize the R^2 value. The best fit theoretical curves and their corresponding R^2 value for the epoxied thermocouple experiments are plotted in Figure 4.12. The R^2 value (=0.82) for the welded thermocouple is included for comparison.

The data for the 30 gage epoxied thermocouples, except for Exp. EW1, match well with theoretical curves only near the workpiece surface (cutoff depth $z_0 \leq 0.15$ mm). Experiments E1, E2, and EM give $\varepsilon_{fitting}$=81%, $\varepsilon_{fitting}$=84%, and $\varepsilon_{fitting}$=70%, respectively. However, the R^2 value for Exp. EM (=0.64) is lower than for the other experiments. Apparently the temperature measurements in Exp. EM have a larger variation than the others due to discontinuous fluid delivery using the MQL device with 1−2 Hz pulsed fluid delivery. For Exp. EW1, the temperature rise is below the fluid burn-out limit of about 120°C. A theoretical curve with $\varepsilon_{fitting}$=21% matches the data fairly well over the whole range (z_0=0.3 mm) with R^2=0.73. Such a low energy partition in this case indicates effective cooling by the fluid at the grinding zone, as previously mentioned. For more aggressive wet grinding, Exp. EW2, the temperature at the grinding zone was much higher than the burnout limit, so cooling at the grinding zone should have been ineffective. This can account for the much higher energy partition of $\varepsilon_{fitting} \approx$ 90%.

By contrast, the data obtained with the 46 gage epoxied thermocouple (Exps. ES1 and ES2), does not match any theoretical curves (R^2<<1). In these cases, the measured temperature is very low far below the ground surface. Apparently the small thermocouple junction fits loosely in the blind hole leading to a much larger contact thermal resistance. Nonetheless, when the connection between the thermocouple junction and the workpiece starts to form during grinding (z<0.04 mm), the measured temperatures increases substantially as seen in Figure 4.12.

4.2.5.3. Energy partition results by surface temperature matching

One important advantage with epoxied thermocouples is that temperature measurements can be directly obtained at the workpiece surface as seen in Figure 4.6. Therefore it should be possible to use these peak surface temperature measurements to obtain more precise estimations of the energy partition values by matching the average of these peak temperature rises with the theoretical values according to either the simple heat transfer analysis (Equation (4.1)) or the inverse heat transfer model (Equation (4.8)). Again for this purpose, a triangular heat source was assumed. For the welded thermocouple, only the peak temperature rise at depth z=0 was used to calculate the energy partition, since only one temperature measurement at the workpiece surface was available.

The results are summarized in Table 4.2, which also includes corresponding values for the specific tangential force, grinding power, and heat flux to the workpiece at the grinding zone. The energy partitions obtained with both heat transfer models (ε_{simple} and $\varepsilon_{inverse}$) are almost identical, and they are also very close to the values obtained by

curve fitting ($\varepsilon_{fitting}$) with high R^2 values (R^2>0.8). When the R^2 value is lower, the estimated ε is less accurate. For Exp. EM, with R^2=0.64, $\varepsilon_{fitting}$ is about 14% lower than the values obtained with both heat transfer models. Slightly higher energy partitions were obtained with the epoxied thermocouples (Exps. E1 and E2) than with the welded thermocouple (Exp. W) because the epoxied thermocouples indicate slightly higher surface temperatures. Likewise higher energy partitions are also obtained with smaller epoxied thermocouples (Exps. ES1 and ES2) than with larger ones (Exps. E1 and E2). The very low energy partition of only 24% for the fine wet grinding test, Exp. EW1, can be attributed mainly to effective cooling at the grinding zone below the film boiling temperature, as previously indicated. With more aggressive wet grinding (Exp. EW2), the grinding zone temperature greatly exceeded the fluid film boiling temperature, cooling at the grinding zone became insignificant. The estimated energy partition of 84% for MQL grinding, Exp. EM, is almost identical to the energy partition for dry grinding, so it can be concluded that the minute amount of fluid applied by MQL provides virtually no cooling at the grinding zone.

Table 4.2. Summary of heat transfer analysis in grinding experiments

Exp.	W	E1	E2	ES1	ES2	EW1	EW2	EM
Fixturing method	Welded	Epoxied						
Thermocouple wire gage	30	30	30	46	46	30	30	30
Max. temperature rise (°C)	469	493	503	525	511	106	474	444
Specific tangential force, F_t (N/mm)	2.00	2.05	2.09	1.96	2.00	1.50	2.40	1.79
Grinding power (W)	390	400	408	382	390	293	468	349
ε_{simple} - simple model	78%	80%	80%	89%	85%	24%	92%	83%
$\varepsilon_{inverse}$ - inverse heat transfer	79%	82%	82%	90%	87%	24%	93%	84%
$\varepsilon_{fitting}$ - curve fitting	72%	81%	84%	--	--	21%	90%	70%
- R^2 for the curve fitting	0.82	0.89	0.90	--	--	0.73	0.85	0.64
Heat flux into workpiece (W/mm^2)	36.2	38.3	39.1	40.5	39.7	8.3	51.2	34.5

4.2.6. Summary

A new thermocouple fixating method was developed for grinding temperature measurement which uses epoxy instead of spot welding to affix the tip of the thermocouple to the bottom of a blind hole. Experiments were conducted to compare the performance of epoxied and welded thermocouples. For expoxied thermocouples, the good thermal contact was obtained as the thermocouple junction became exposed by smearing of the workpiece material during grinding, thereby providing an accurate measurement of the surface temperature at the grinding zone. For welded thermocouples, the junctions tend to be damaged during grinding as they becomes exposed and the maximum temperatures are slightly smaller than the temperatures measured with epoxied thermocouples.

Grinding experiments and heat transfer analyses showed that grinding fluids provide negligible cooling within the grinding zone as evidenced by the high energy partitions which ranged from 84% to 92% for dry grinding, wet grinding, and MQL grinding. An exception was observed for fine wet grinding which gave a much lower energy partition of 24%, due to cooling within the grinding zone below the film boiling temperature. Although cooling by the fluid may be ineffective within the grinding zone, cooling can occur outside the grinding zone as evidenced by the much faster drop in the measured temperature from its peak value with wet grinding (Figure 4.9) than with dry grinding (Figure 4.8). Bulk cooling of the workpiece in this way can be an important factor in controlling thermally induced dimensional inaccuracy and distortion. While MQL is effective in providing lubrication, it can be seen by comparing the temperature response curves for MQL (Figure 4.10) with those for dry grinding (Figure 4.9) that the

miniscule amount of applied fluid with MQL does not provide any significant cooling outside the grinding zone. This is a major drawback which can limit the more widespread application of MQL for grinding.

4.3. MQL Grinding using Vitrified CBN Wheels

From the previous section, it is confirmed that with convectional abrasive wheels MQL does not provide significant cooling in grinding, resulting in a high energy partition to the workpiece. To fundamentally lower the energy partition and reduce the workpiece temperature (in order to avoid thermal damage), CBN grinding wheels are considered in this section.

In addition, from Chapter 3, it is concluded that some nanoparticle additives may improve the lubricating properties of the base fluids. However, although it is the best lubricant among the three tested base oils, the soybean oil did not show any further significant improvement with MoS2 nanoparticle additives. Therefore, soybean oil was again chosen as for the MQL application in this study. In addition, another type of nanoparticles - carbon nanotube (CNT) was mixed in soybean oil as the additive to investigate the potential application of nano-lubricant in MQL grinding.

4.3.1. Experimental Procedure

Experiments of straight surface plunge grinding without crossfeed were conducted on the same machine (Chevalier Model Smart-B818 surface grinding machine with a 1.5 kW spindle). The experimental setup is shown in Figure 4.13(a), very similar to the pervious setup. The vitreous bond CBN grinding wheel (Universal Abrasive

VB126-J160-VT2W19) was used. The grinding wheel is about 177.8 mm in diameter and 12.7 mm in width. The surface speed of the wheel was 30 m/s. The work-material was the same as before.

For wet grinding, the water-based Cimtech 500 synthetic grinding fluid at 5 vol% was used. MQL grinding, shown in Figure 4.13(b), utilized the same fluid application device provided by AMCOL (Hazel Park, Michigan). Soybean oil and soybean oil mixed with CNT additives, denoted as CNT-soybean oil, were used for MQL application. The CNT-soybean oil were prepared by mixing soybean oil with multi-wall carbon nanotubes using 2 wt% lecithin as surfactant and subjected to 2 hrs of ultrasonic homogenization. The added multi-wall carbon nanotubes (L-MWCNT-1020), provided by Shenzhen Nanotech Port Co. in China, has outside diameter of 10-20 nm and length of 5-15 μm. The flow rate was 5400 ml/min for flood (wet) grinding, but only 5 ml/min for MQL. The grinding wheel was dressed at 2 μm down feed, 500 mm/min traverse speed and –0.4 speed ratio using a rotary diamond disk, which is 96 mm in diameter and 3.8 mm in width.

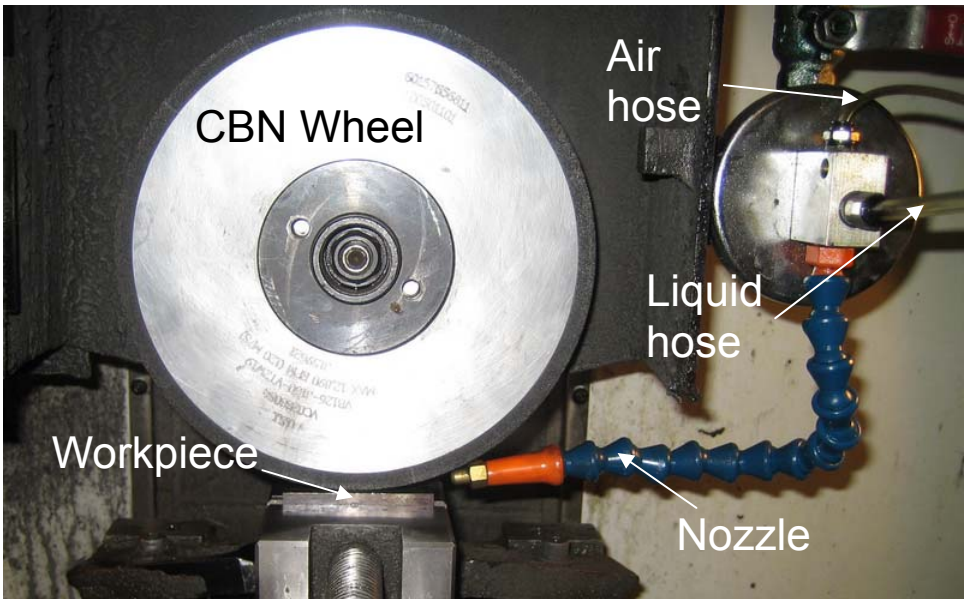

(a)

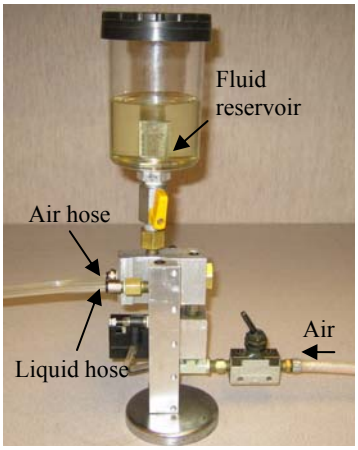

(b)

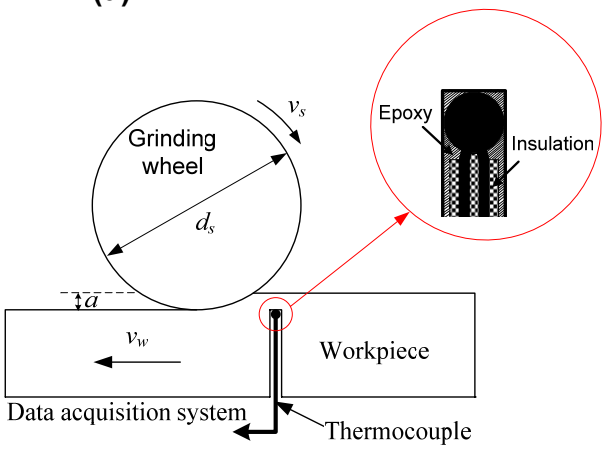

(c)

Figure 4.13. Experimental setup: (a) overview, (b) MQL fluid delivery device, and (c) illustration of grinding temperature measurement

Two sets of experiments were conducted. The first set of the experiments investigates the influence of down feed and feed rate on grinding forces and surface finish under dry, MQL, and flood cooling conditions. The down feeds and feed rates as well as the corresponding specific material removal rate (MRR) in this set of experiments are listed in Table 4.3. The specific MRR is defined as the material removal rate per unit width. The normal and tangential grinding forces were measured using a Kistler Model

9257A piezoelectric dynamometer. The surface roughness was measured using a Taylor Hobson Taylorsurf profilometer. Three measurement traces perpendicular to the grinding direction were measured. The average of three arithmetic average surface roughness (R_a) values was used to represent the roughness of a ground surface.

Table 4.3. Grinding parameters and corresponding specific MRR

Down feed (μm)	Feed rate (mm/min)	Specific MRR(mm^2/s)
25	1200	0.5
	2400	1.0
	3600	1.5
	4800	2.0
	6000	2.5
50	1200	1.0
	2400	2.0
	3600	3.0

The second set of the experiments was to study the heat transfer in CBN MQL grinding. The experiments were conducted in dry, wet and MQL grinding using both soybean oil and CNT-soybean oil, as listed in Table 4.4. For each cutting fluid application except for dry grinding, two sets of cutting parameters were tested(1) 25 μm down feed and 2400 mm/min feed rate and (2) 50 μm down feed and 3600 mm/min feed rate. For dry grinding, only the less aggressive cutting parameters (25 μm down feed and 2400 mm/min feed rate) were applied. The grinding temperatures were measured by the embedded thermocouple method (Shen et al., 2009) proposed in the Section 4.2, as shown in Figure 4.13(c). The temperature and grinding force data were collected at a sampling rate of 5 kHz. After each grinding pass, the workpiece was allowed to cool to the initial temperature before the next pass was taken.

Table 4.4. Experimental design for grinding temperature measurements

Cutting fluid application	Down feed (μm)	Feed rate (mm/min)	Energy Partition
Dry	25	2400	68.7%
MQL (Soybean oil)	25	2400	53.8%
	50	3600	54.0%
MQL (CNT-soybean oil)	25	2400	54.3%
	50	3600	53.5%
Flood cooling	25	2400	13.2%
	50	3600	13.8%

As shown in Figure 4.13(c), the surface grinding experiments were conducted with a wheel of diameter d_s rotating at peripheral surface speed v_s removing a depth a (down feed) of work-material as it passes under the wheel at the workpiece speed v_w (feed rate). The grinding energy expended at the grinding zone is converted to heat, which is transported to the workpiece, grinding wheel, chips and grinding fluid. The geometrical grinding zone is the region of length l_c ($=\sqrt{d_s a}$) where the wheel interacts with the workpiece (Malkin, 1989).

A critical parameter for grinding thermal analysis is the energy partition, ε, which is defined as the fraction of the grinding energy transported as heat to the workpiece. In this study the grinding temperatures were measured using an epoxied thermocouple (Shen et al., 2009). At the grinding pass when the thermocouple junction was exposed and bonded to the surface of the workpiece, the measured temperature reaches its peak. This peak temperature profile was used in the temperature matching method (Kohli et al., 1995; Guo et al., 1999) to determine the energy partition. In this method, the measured temperature profile is matched to the theoretically calculated temperature from the thermal model with a triangular heat source of length l_c within the grinding zone moving along the ground surface at speed v_w, as shown in Figure 4.14.

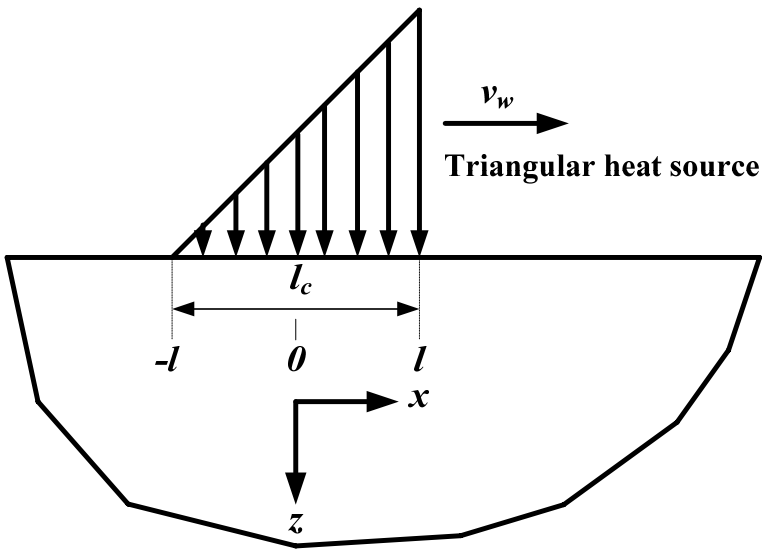

Figure 4.14 Schematic drawing of heat transfer in down grinding

4.3.2. Grinding Forces

The specific tangential and normal grinding force and force ratio vs. the specific MRR for 25 μm down feed is shown in Figure 4.15. Both the normal and tangential specific grinding forces increase almost linearly with respect to specific MRR. For the specific tangential grinding force, although the amount of the cutting fluids was reduced by about a thousand times, MQL grinding still has about the same tangential forces for all tested conditions as compared to that of flood cooling. This is likely due to the good lubrication of soybean oil as well as the more efficient penetration of the fluid into the grinding zone by MQL delivery system (Silva et al., 2005). MQL grinding can achieve the same level of MRR as that of flood cooling. It shows the potential feasibility of MQL in high volume production grinding.

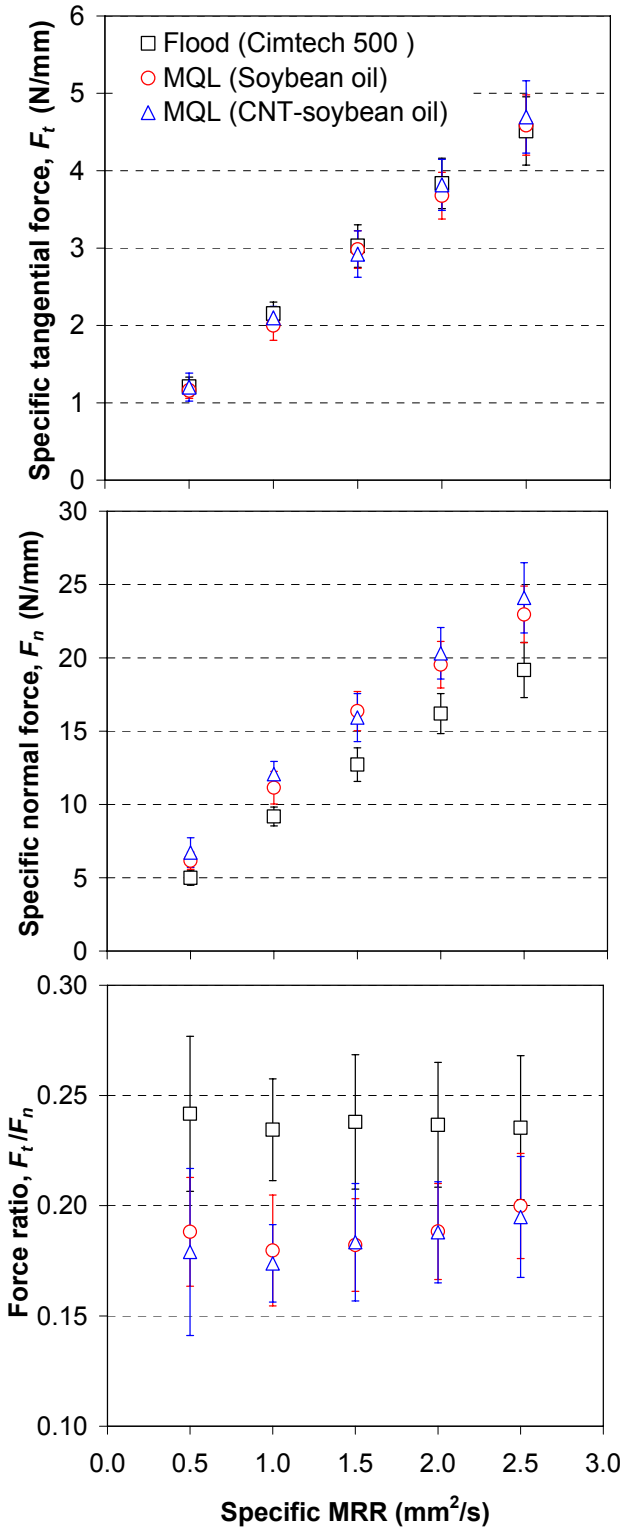

Figure 4.15. Specific grinding forces vs. specific MMR (Down feed = 25 μm)

Adding CNT in soybean oil has no improvement in terms of the reduction in grinding force. The previous study by Shen et al. (2008b) has pointed out that the improvement of lubrication with nanoparticle additives could depend on the base fluid chemistry which will guide their interaction (teaming) with the suspended nanoparticles. The selection of appropriate base fluid is critical in the application of nano-lubricant. The results of this study suggest that CNT as the additive lubricant is not appropriate for soybean oil based fluid from the friction reduction point of view.

For specific normal grinding force, it is noticed that MQL grinding with pure soybean oil and CNT-soybean oil has larger normal forces than that of flood cooling. This is attributed to the larger viscosity of soybean oil, which results a higher hydraulic pressure in the grinding zone. The higher normal grinding force and almost the same tangential grinding force lead to a smaller Ft/Fn force ratio for MQL grinding. This implies that better lubrication of the cutting fluid in MQL grinding.

The results of 50 μm down feed (seen in Figure 4.16) exhibited identical trend as that of 25 μm down feed. At the same MMR, the specific tangential and normal grinding forces of 50 μm down feed are slightly higher than that of 25 μm down feed. Larger specific normal force was also observed in MQL grinding with soybean oil and CNT-soybean oil compared to that of flood cooling.

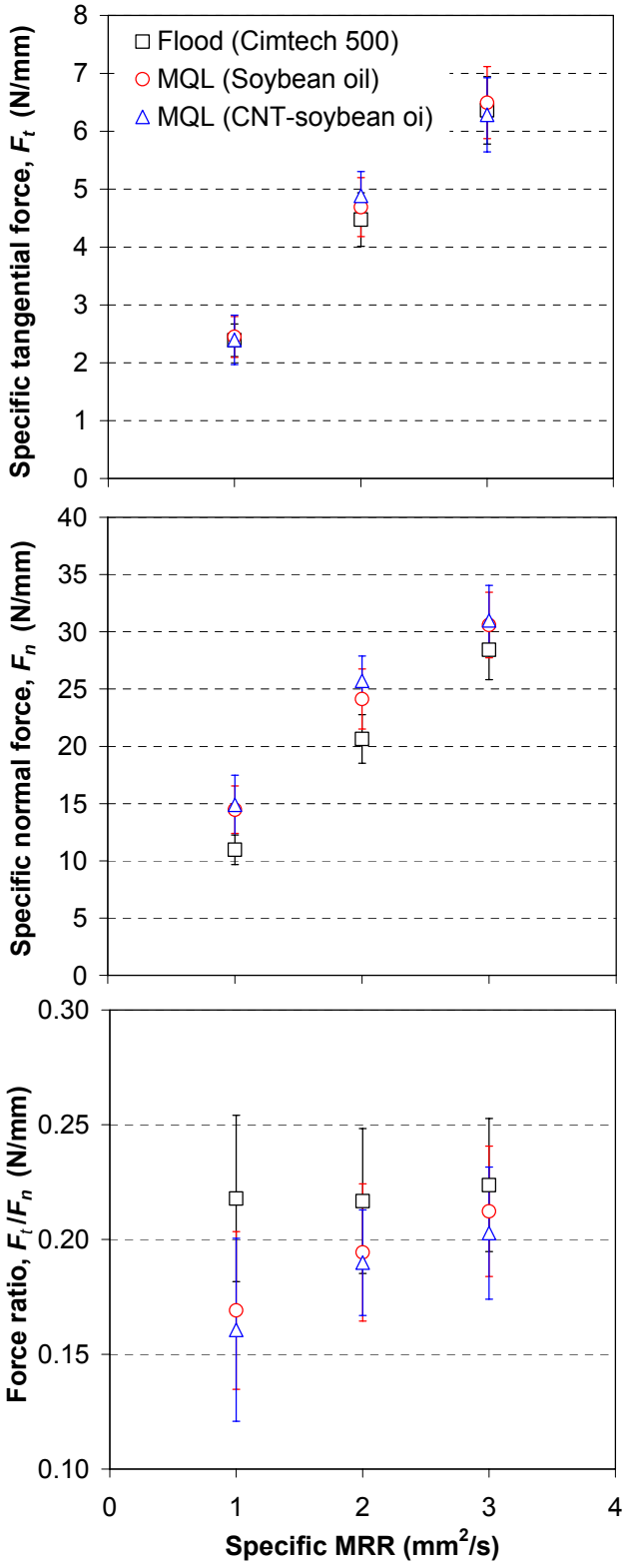

Figure 4.16. Specific grinding forces vs. specific MMR (Down feed = 50 µm)

4.3.3. Surface Finish

The surface roughness results for 25 µm down feed are presented in Figure 4.17. The surface roughness increases with the increasing feed rate, as is expected. Flood cooling generate slightly better surface finish than that of MQL grinding, likely due to better chip flushing to prevent scratching on the workpiece surface. The CNT additive does not show improvement in terms of surface finish. The surface finish results of 50 µm down feed exhibited identical trend as that of 25 µm down feed, as shown in Figure 4.18.

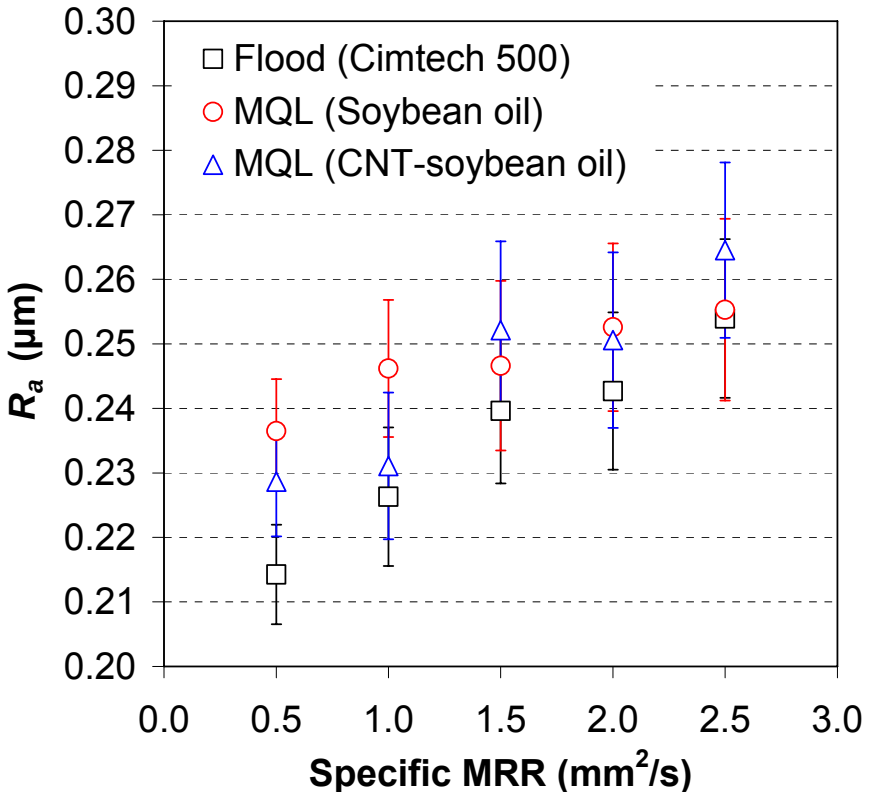

Figure 4.17. Surface finish results (Down feed = 25 µm)

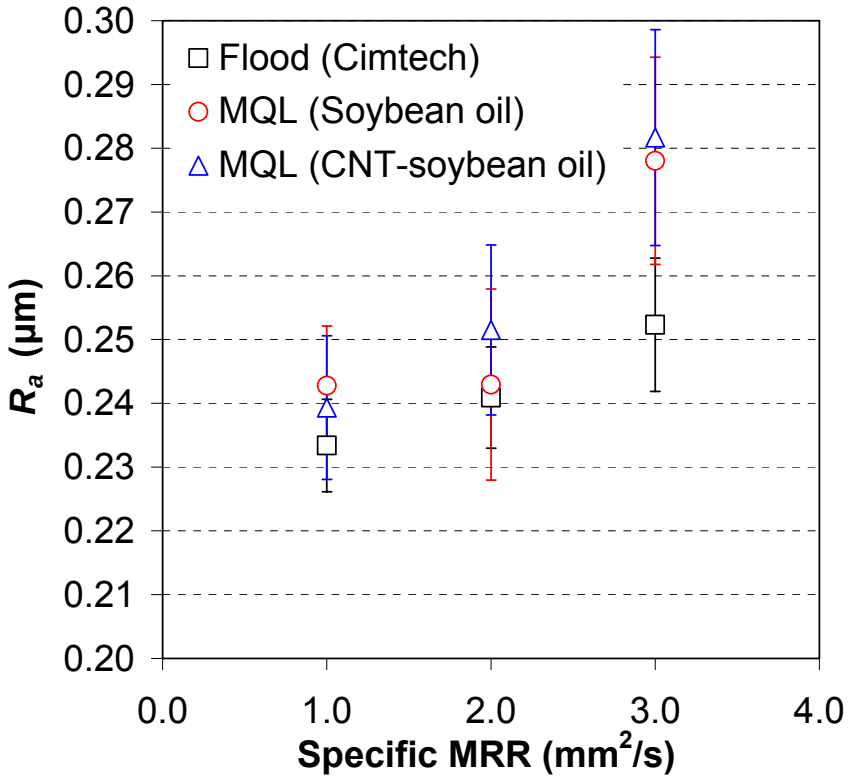

Figure 4.18. Surface finish results (Down feed = 50 μm)

4.3.4. Energy Partition

For dry grinding, the measured surface temperature profile vs. the dimensionless distance, x/l, where x is the local coordinate described in Figure 4.14 and $l=l_c/2$, is shown in Figure 4.19. The experimental data matches perfectly with the theoretical temperature for ε=68.7%. The good match validates the proposed grinding temperature measurement and energy partition calculation.

Figures 4.20(a)-(c) present the temperature measurements in wet and MQL grinding using both soybean oil and CNT-soybean oil under 25 μm down feed and 2400 mm/min feed rate. The measured temperature in wet grinding, as shown in Figure 4.20(a), is much lower and the energy partition ε=12.5%. Note there is significant

discrepancy of calculated and measured in the trailing edge (x/l <–1). It is due to the fluid cooling effect. For MQL grinding, as shown in Figures 4.20(b) and (c), both grinding temperature and energy partition are between the values of dry and wet grinding. The temperature matching method gives ε=53.8% for MQL grinding using soybean oil and ε=54.3% for CNT-soybean oil. The insignificant difference in ε shows the limited effect of CNT additive. Even the thermal-physical properties of the MQL fluids can be very different, it makes essentially no impact on the energy partition. Note that there is also cooling effect due to fluid in the trailing edge (–5<x/l<–1) in MQL conditions. The fluid flow rate in MQL grinding is very small so that only a small portion of the fluid is able to pass through the grinding zone to cool the nearby trailing edge (–5<x/l<–1) of the ground work-surface.

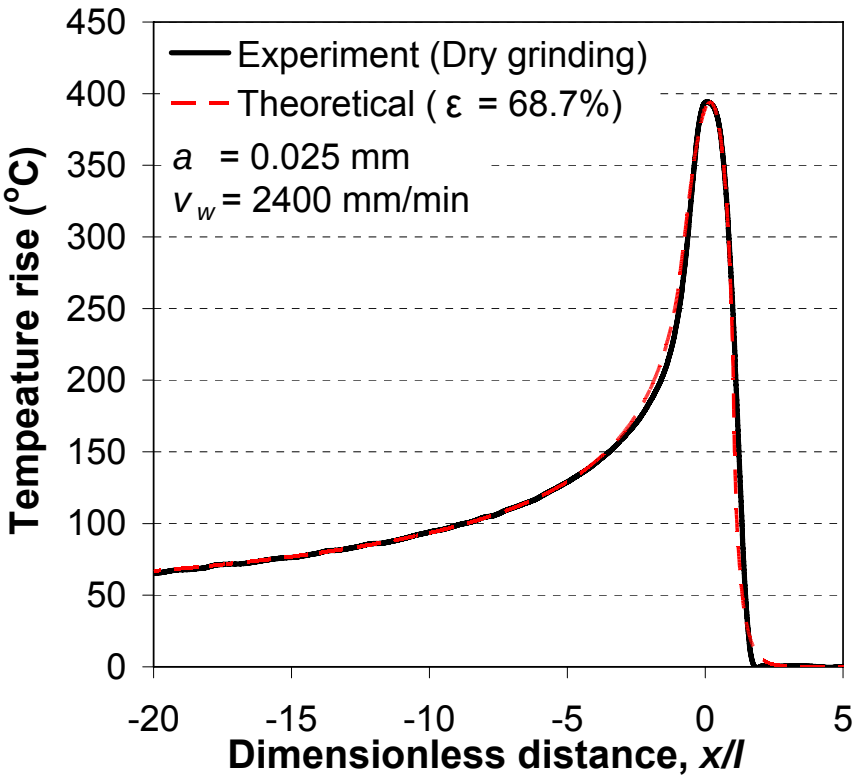

Figure 4.19. Temperature rise at the workpiece surface (dry grinding)

Figures 4.20(d)-(f) present the temperature measurements in wet and MQL grinding using both soybean oil and CNT-soybean oil under 50 μm down feed and 3600 mm/min feed rate. Due to the limited spindle power, dry grinding is not feasible under this grinding condition. The energy partition results are very similar to those under the 25 μm down feed and 2400 mm/min feed rate grinding condition. The measured temperature in wet grinding, as shown in Figure 4.20(d), is relatively low and matches with the theoretically calculated temperature for a much smaller ε=13.8%. Significant cooling due to fluid in the trailing edge ($x/l<-1$) again is also evident, like in Figure 4.20(a). MQL grinding gives much higher temperature in this case due to the increased grinding power, but the energy partition is almost the same as before, ε=54.0% for MQL grinding using soybean oil and ε=53.5% for CNT-soybean oil.

The energy partition results are summarized in Table 4.4. About the same energy partition values (67% for dry, 54% for MQL, and 14% for wet grinding) were observed, regardless of the grinding parameter settings. This is consistent with the findings in Varghese et al. (2000).

4.2.5. Summary

Grinding of cast iron using vitrified CBN wheels under dry, MQL and flood cooling conditions was studied. Compared to the flood cooling condition, MQL grinding could achieve the same MRR without increasing grinding forces. Flood cooling did produce slightly better surface finish than MQL grinding due to efficient chip flushing. The CNT additives showed no benefit to improve the grinding forces or surface finish.

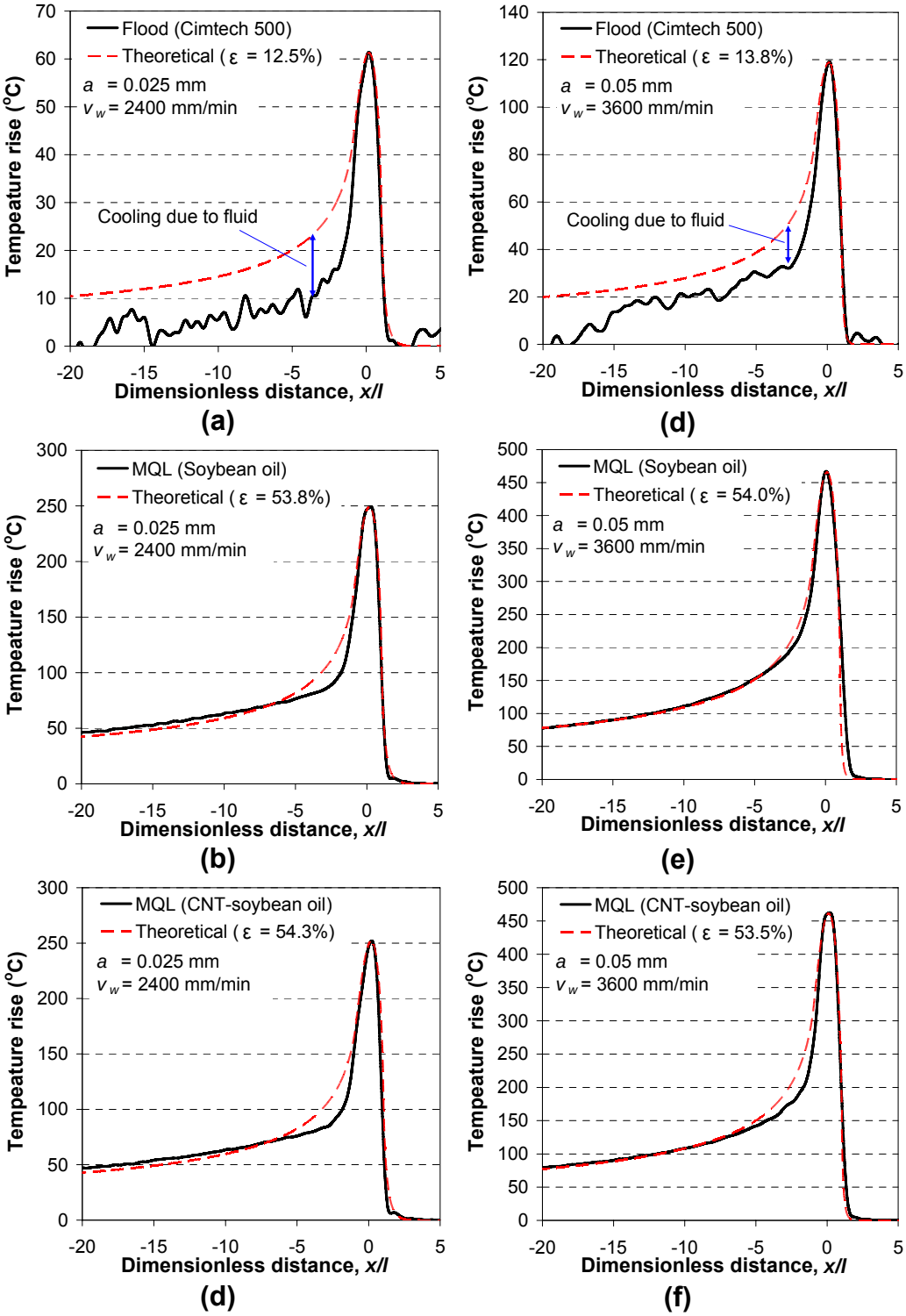

Figure 4.20. Temperature rise at the workpiece surface: (a), (b), (c) 25 µm down feed, 2400 mm/min feed rate, and (d), (e), (f) 50 µm down feed, 3600 mm/min feed rate.

Flood cooing condition had the lowest grinding temperature and smallest energy partition of about 13%. The dry condition exhibited the highest grinding temperature and largest energy partition of 68%. The energy partition under MQL condition is in between, about 54%. These results are higher than the literature of CBN grinding. Varghese et al. (2000) reported that values of the energy partition were found to range from 3 to 6% for grinding of nodular cast iron with a vitrified CBN wheel in flood cooling condition, and higher energy partitions up to 60% were obtained by reducing or eliminating the fluid. The difference between our and Varghese et al. (2000) results is likely attributed to the higher wheel surface speed (v_s=60 m/s) used in their study. Based on the study by Lavine (1988), high wheel speed reduces the energy partition and also enhance the forced convection within the grinding zone by increasing the flow rate of the cutting fluid.

For conventional shallow-cut grinding of steels with Al_2O_3 wheels, measurement of energy partition have been typically found to range from 60% to 85% (Malkin, 1989; Kohli et al., 1995). Therefore, MQL grinding using vitrified CBN wheels with an energy partition of about 54% is better than the conventional grinding with Al_2O_3 wheels in this aspect.

Overall, this study shows that the vitrified CBN wheel can improve the insufficient cooling problem of MQL grinding to certain extend. It is feasible to combine MQL technique and vitrified CBN wheel to achieve high volume grinding production. But, how to further increase the MRR without sacrifice of the surface finish or thermal damage to the workpiece still needs more research. Advanced CBN wheel with more porous vitreous bond is identified as a key technology to make the MQL CBN production grinding possible.

4.4. Concluding Remarks

A new thermocouple fixating method was developed for grinding temperature measurement. Experiments were conducted to validate the proposed method. The method was further used to experimentally investigate the heat transfer problems in grinding. Grinding of cast iron using aluminum oxide and vitrified CBN wheels under dry, MQL and flood cooling conditions was studied.

With conventional abrasive (aluminum oxide) wheels, grinding fluids provide negligible cooling within the grinding zone as evidenced by the high energy partitions which ranged from 84% to 92% for dry grinding, wet grinding, and MQL grinding. An exception was observed for fine wet grinding which gave a much lower energy partition of 24%, due to efficient cooling within the grinding zone below the film boiling temperature. Cooling by the fluid was found to be more effective outside the grinding zone rather than within the grinding zone.

With superabrasive wheels (vitrified CBN wheels), much lower energy partition values were observed, about 68% for dry grinding, 54% for MQL grinding, and 13% for wet grinding. It is concluded that the vitrified CBN wheel can improve the insufficient cooling problem of MQL grinding to certain extend, and it is feasible to combine MQL technique and vitrified CBN wheel to achieve high volume grinding production.

CHAPTER 5

GRINDING THERMAL MODEL BASED ON THE FINITE DIFFERENCE METHOD

A grinding thermal model has been developed based on the finite difference method (FDM) in order to estimate the energy partition and the convection heat transfer coefficient in grinding. It also can be used to study the transient heat transfer and temperature distributions in workpiece with finite dimension and various boundary conditions. The model is first validated by comparing with the traditional grinding thermal model assuming semi-infinite workpiece. Effects of workpiece size, feed rate, and various cooling conditions are further investigated using the FDM model. When the workpiece is short or the feed rate is low, transient heat transfer becomes more dominant during grinding. Investigation of cooling effects revealed that the free convection and cooling in the leading edge have negligible effect, cooling in the trailing edge only has influence in the trailing edge region and cooling in the grinding zone has a significant effect on the reduction of workpiece temperature. The model is further applied to investigate convective cooling in the grinding experiment. The estimated average convection heat transfer coefficient in the grinding contact zone was about 4.2×10^5

W/m^2-K for wet grinding and 2.5×10^4 W/m^2-K for MQL grinding, while the estimated convection heat transfer coefficient in the trailing edge was much lower.

5.1. Introduction

The energy required to remove a unit volume of work-material for grinding is very high. Virtually all this energy is converted to heat, which can cause high temperatures and thermal damage to the workpiece such as grinding burn, phase transformations, undesirable tensile residual tensile stresses, cracks, reduced fatigue strength, thermal distortion and inaccuracies (Malkin, 1989). Workpiece thermal damage is the major limitation to increase the material removal rate (MRR) in grinding.

A considerable research effort has devoted to both theoretical and experimental aspects of heat transfer in grinding. The classic thermal analysis of moving heat source and the temperature at sliding contacts was studied by Jaeger (1942). The application of Jaeger's moving heat source solutions to heat transfer problems in grinding was first proposed by Outwater and Shaw (1952), whereby the grinding zone is approximated as a band source of heat moving along the surface of the workpiece. Outwater and Shaw (1952) assumed that grinding heat is mainly generated at the shear plane, and thus the grinding temperature can be calculated by matching the average temperatures on the shear plane. Hahn (1956) considered the frictional rubbing forces on the clearance surface and neglected the cutting forces on the rake surface in the grinding thermal model. Snoeys et al. (1979) and Malkin (1984) presented a comprehensive literature review of early research work on the prediction of workpiece surface temperatures in dry grinding without significant convective heat transfer.

Takazawa (1972) considered the partitioning of energy over the grinding contact zone based on grinding wheel bulk thermal properties. Similar contact zone thermal model was also proposed by Rowe et al. (1988). Shaw (1990) considered both real and apparent contact areas, and used an area ratio factor to correlate grain properties with such a model.

Grain analysis considers the energy partitioning at the grain-workpiece interface, rather than the wheel-workpiece interface (the whole contact zone). It was first proposed by Hahn (1956, 1962, 1966). Later, many grain analysis heat transfer models have been developed (Liao et al., 2000; Maksoud, 2005). The grain analysis models tend to give better results across a wide range of grinding conditions (Rowe et al., 1995).

Lavine (1988) developed an energy partition model, which combines both the micro- and macro-scale thermal analysis. The wheel and grinding fluid are considered to be a composite solid moving at the wheel speed. It predicts the convective heat transfer coefficient on the workpiece surface, the fraction of energy entering the workpiece, and the workpiece surface temperature. The model was further extended to account for the variation of the heat fluxes along the grinding zone in down grinding with large Peclet number (Jen and Lavine, 1995). Ju et al. (1998) considered both the scales of the wheel-workpiece and grain-workpiece contact length and developed a complete thermal analysis that can handle both up and down surface grinding without the assumption of large Peclet number.

Temperature measurements in the workpiece subsurface during grinding indicated that the triangular heat source is more accurate than the rectangular one (Kohli et al., 1995). Analytical investigations by Guo and Malkin (1995a) indicated that energy

partition is approximately constant along the grinding zone for regular down grinding, but varies greatly along the grinding zone for regular up grinding and both up and down creep-feed grinding.

The inverse heat transfer method was also applied to grinding thermal modeling. Guo and Malkin (1996a, 1996b) first developed an inverse heat transfer method to estimate the heat flux distribution in the workpiece for regular grinding and the local convective heat transfer coefficient on the workpiece surface from the measured temperature distributions in the workpiece. Inverse heat transfer models have been studied extensively in grinding processes (Hong and Lo, 2000; Wang and Chen, 2002; Kim and Kwak, 2006). These models are similar to Guo and Malkin (1996a, 1996b), except that Wang and Chen (2002) generalized the inverse heat transfer model to the 3D case.

Most of these traditional grinding thermal models have assumptions such as the steady-state condition, semi-infinite workpiece size, and adiabatic boundary condition on the workpiece surface. The numerical method is an approach to overcome these constraints. The finite element method (FEM) and finite difference method (FDM) are considered to model the heat transfer problems in grinding. Guo and Malkin (1995b) has developed the FDM based grinding thermal model for the transient temperature distribution and shown that workpiece temperature rises rapidly during the initial wheel-workpiece engagement, subsequently reaches a quasi-steady state value if the workpiece is sufficiently long and further increases during the final wheel-workpiece disengagement. The FEM has been widely employed to simulate the workpiece grinding temperature for both 2D and 3D cases and further developed to analyze the phase transformation and

thermal stress on ground surface (Mahdi and Zhang, 1995; Biermann et al., 1997; Wang et al., 2003; Mamalis et al., 2003; Lefebvre et al., 2006).

FDM applies the discrete analog of the derivative and is simple to formulate, easy to apply and straightforward to extend to two or three dimensional problems. In this study, a FDM based grinding thermal model is developed to study the heat transfer in grinding. This model is similar to that developed by Guo and Malkin (1995b). In addition to the transient heat transfer problem, this study also investigated the workpiece with finite dimension and various boundary conditions. The model is introduced in Section 2 and validated by comparing with the solution of the traditional heat transfer model in Section 3. Effects of workpiece dimension, feed rate, and various boundary conditions are studied using the FDM heat transfer model in Sections 4 and 5. In Section 6, the FDM heat transfer model is further applied in the grinding experiment to estimate the energy partition and convection heat transfer coefficient.

5.2. Finite Difference Heat Transfer Model

To apply the finite difference method, the first step is to subdivide the computation domain into small regions and assigning each region a reference point. In this study, the computation domain is the workpiece, as shown in Figure 5.1(a). Each node is at the center of a small region, and designated by the indices, as seen in Figure 5.1(b). The grid size is defined as the distance between the two adjacent nodes. In this study, the uniform grid size is used, i.e., $\Delta x = \Delta z$. The moving heat source was assumed to be triangular.

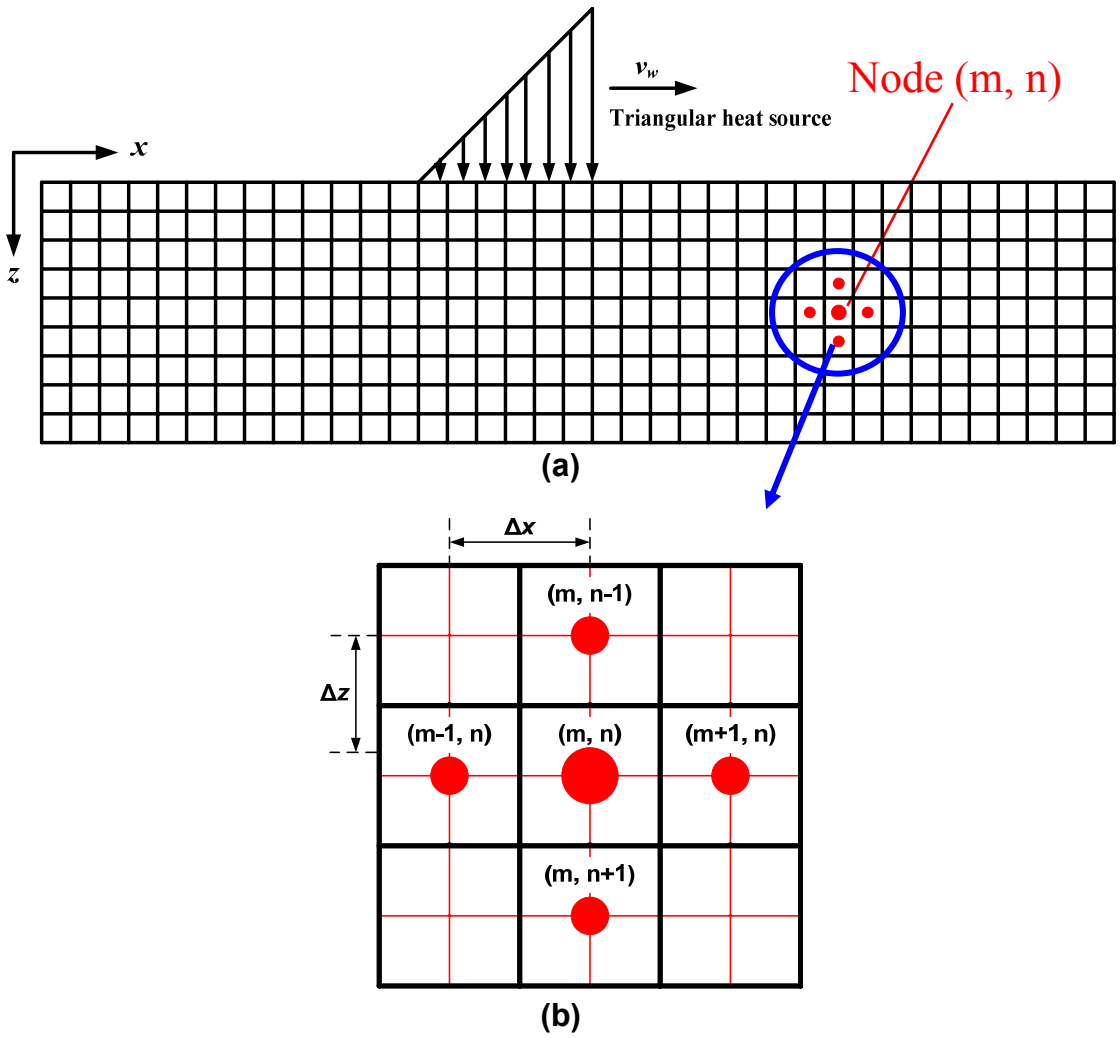

Figure 5.1. Illustration of nodal network: (a) mesh of the computation domain (workpiece) and (b) close-up view of the nodal network

5.2.1. Governing Equation

Now that the computation domain is characterized in terms of a nodal network, the governing equation and the boundary conditions need to be transformed into the finite difference form to compute the nodal temperatures. The 2D heat transfer governing equation is:

$$\frac{\partial^2 T}{\partial x^2} + \frac{\partial^2 T}{\partial z^2} = \frac{1}{\alpha}\frac{\partial T}{\partial t} \tag{5.1}$$

where α is the thermal diffusivity of the workpiece. Using the finite difference discretization, Equation (5.1) can be expressed as:

$$\frac{T_{m+1,n}(t)+T_{m-1,n}(t)-2T_{m,n}(t)}{(\Delta x)^2}+\frac{T_{m,n+1}(t)+T_{m,n-1}(t)-2T_{m,n}(t)}{(\Delta z)^2}=\frac{1}{\alpha}\frac{T_{m,n}(t+\Delta t)-T_{m,n}(t)}{\Delta t} \quad (5.2)$$

Considering the uniform mesh ($\Delta x = \Delta z$), Equation (5.1) can be rearranged as following:

$$T_{m,n}(t+\Delta t)=\frac{\alpha\Delta t}{(\Delta x)^2}\left[T_{m-1,n}(t)+T_{m+1,n}(t)+T_{m,n-1}(t)+T_{m,n+1}(t)\right]+\left[1-4\frac{\alpha\Delta t}{(\Delta x)^2}\right]T_{m,n}(t) \quad (5.3)$$

5.2.2. Boundary Conditions

In the finite difference method, either full grid or half grid can be used at the boundary. The half grid has the advantage of direct expression of the nodal temperature at the boundary, while the full grid requires much less computation time and is more accuracy because of the uniform mesh. Therefore, in this study the full grid was adopted at the boundary. The surface grinding configuration is shown in Figure 5.2(a). In this configuration, as seen in Figure 5.2(b), six boundaries, the leading edge, contact zone, trailing edge, front, back and bottom side of the workpiece, need to be considered. Finite

difference equations for these boundary conditions (BCs) can be derived by energy conservation and the results are summarized in Appendix B.1.

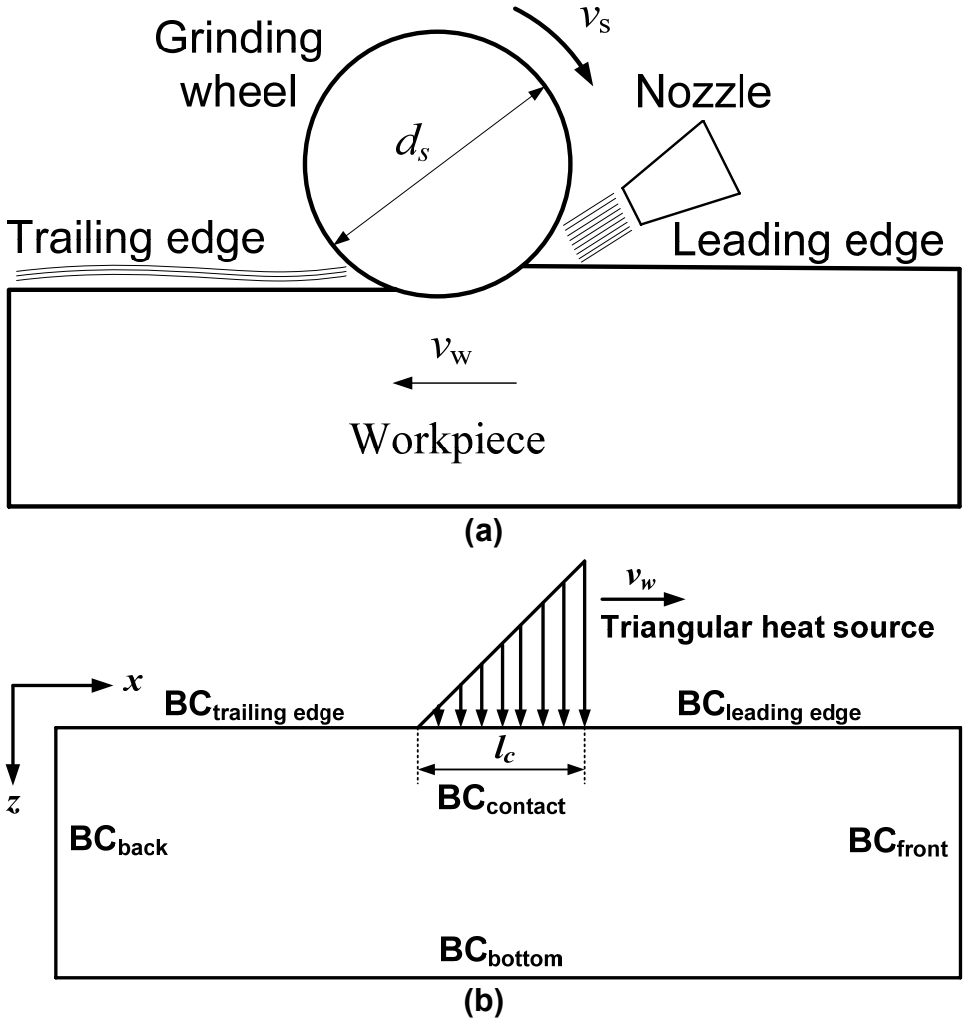

Figure 5.2. Illustration of the boundary conditions: (a) surface grinding process and (b) the corresponding BCs

5.2.3. Surface Temperature

Since the full grid was used at the boundary instead of the half grid, the temperature on the ground workpiece surface, T^s, which is of the most interest, needs to be derived using energy balance method. Finite difference equations for the top surface

temperature prediction are presented in Appendix B.2.

5.3. Validation of Finite Different Thermal Model

Unlike the traditional grinding thermal models which only give the steady state solution, the FDM heat transfer model can calculate the evolution of temperature within the workpiece which makes it capable to handle the transient heat transfer problems in grinding. To validate the FDM heat transfer model developed in this study, the results of the FDM model is compared with the solution of the traditional heat transfer model (Kohli et al, 1995; Guo and Malkin, 1996a; 1996b).

The FDM heat transfer model was first applied to simulate the spatial and temporal temperature distribution of grinding Dura-Bar 100-70-02 ductile iron workpiece with length L=50 mm and thickness H=10mm. The grinding parameters and work-material properties are listed in Table 5.1. The triangular moving heat source, as shown in Figure 5.2(b), with an average heat flux of 40 W/m^2 and a width of contact length l_c = 1.33 mm was used. All the BCs are set to be adiabatic, identical to the assumption for the traditional heat transfer model.

Table 5.1. Summary of the parameters used in simulation

Wheel diameter d_s	177.8 (mm)
Depth of cut a	10 (μm)
Wheel speed, v_s	30 (m/s)
Feed rate, v_w	0.04 (m/s)
Thermal conductivity of workpiece, k_w	63 (W/m·K)
Thermal diffusivity of workpiece, α_w	16.3×10^{-6} (m^2/s)

The spatial distributions of temperature field in the workpiece at time t = 0.15, 0.40, 0.65, 0.90, and 1.15 (s) are shown in Figure 5.3. The time t = 0 s is defined at the

start of wheel contacting the workpiece. A similar pattern of the temperature field with high temperature region of about 480°C is observed beneath the moving heat source and propagating along the x-axis.

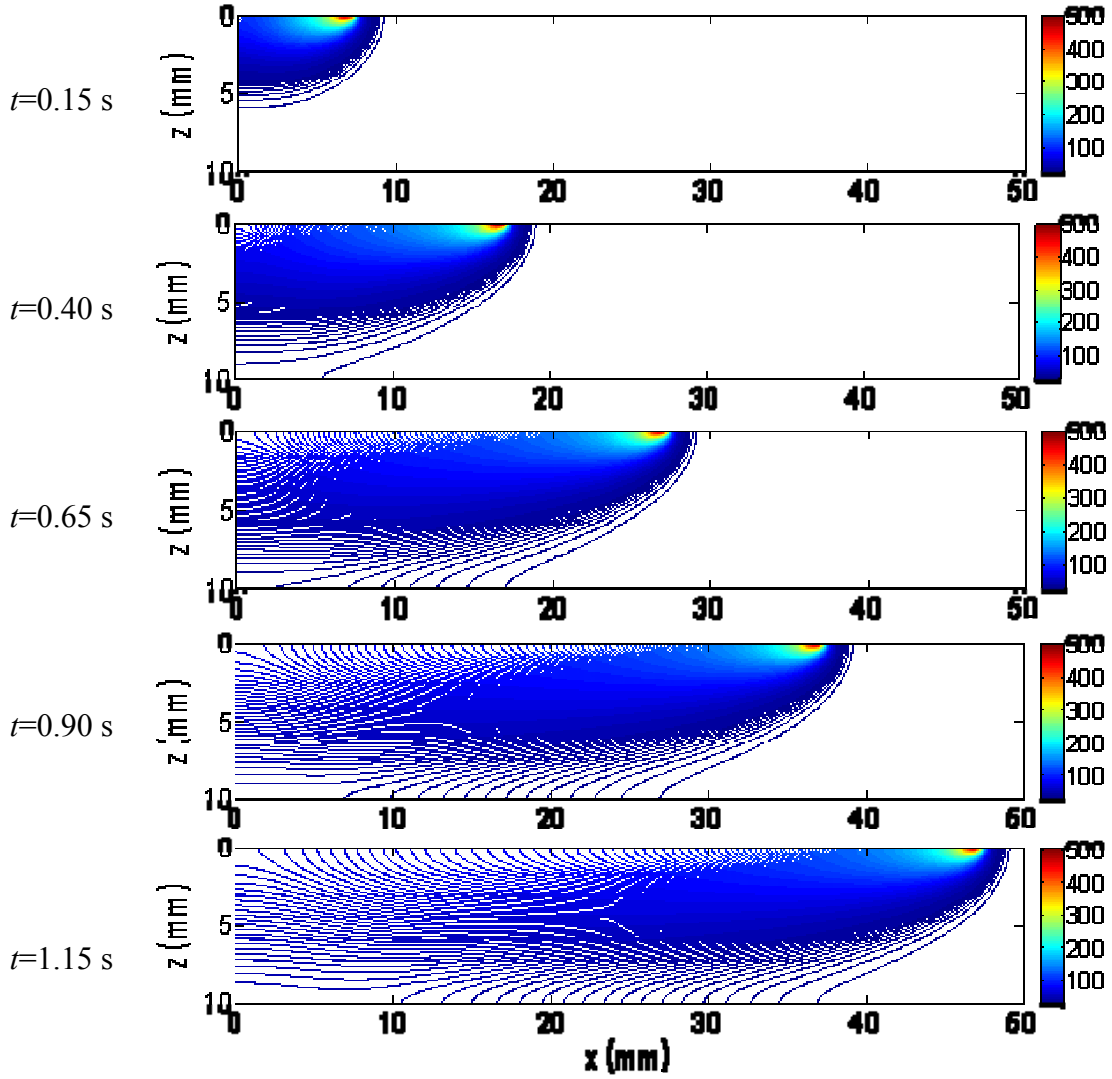

Figure 5.3. Temporal and spatial distributions of the workpiece temperature (*L*=50 mm and *H*=10 mm)

The temporal and spatial distributions of temperature on the ground surface are plotted in Figure 5.4. There are three regions, cut-in, steady-state, and cut-out. In the cut-in region, the workpiece peak temperature rises rapidly when the grinding wheel first

engages with the workpiece. In the steady-state region, the workpiece surface temperature profile reaches a stable status. The peak temperature maintains at about 480°C, the same level of peak temperature in Figure 5.3. As the wheel disengaging from the workpiece, due to the boundary condition, the peak temperature increases to 550°C and higher for a short period of time in the cut-out region. The transient heat transfer during the cut-in and cut-out region has been previously studied by Guo and Malkin (1995b). This simulation results also indicate that a steady-state region exists if the workpiece is long enough.

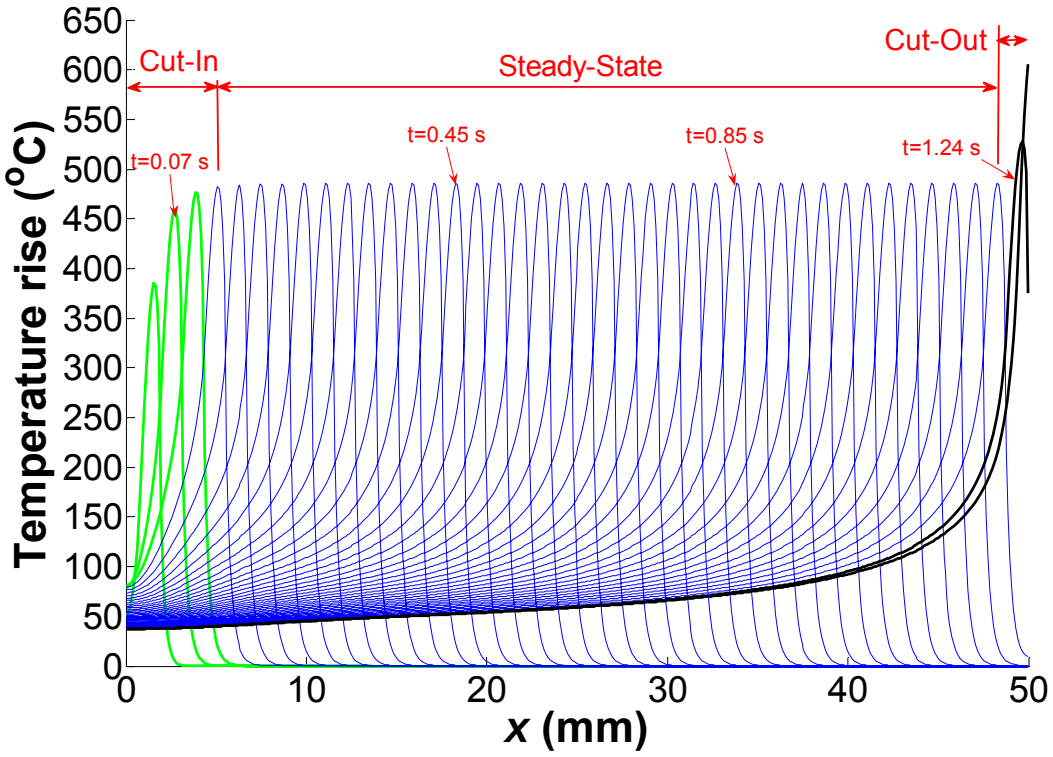

Figure 5.4. Temporal and spatial distribution of the grinding temperature at the workpiece surface (*L*=50 mm, *H*=10 mm, v_w=2400 mm/min)

The steady-state FDM heat transfer solution is compared with that of the traditional heat transfer model. As shown in Figure 5.5, the FDM surface temperature

profile at t = 0.625 s (steady-state region) is plotted against the results from the traditional heat transfer model (Kohli et al, 1995; Guo and Malkin, 1996a; 1996b). The x-axis is the dimensionless distance, x/l, where x is the local coordinate with original point at the center of the grinding zone and $l=l_c/2$. The results match very well except some small deviation (less than 10°C) at the far trailing edge (x/l<-25). This discrepancy is because the FDM model uses a workpiece with a finite dimension, while the traditional model has an assumption of semi-infinite body.

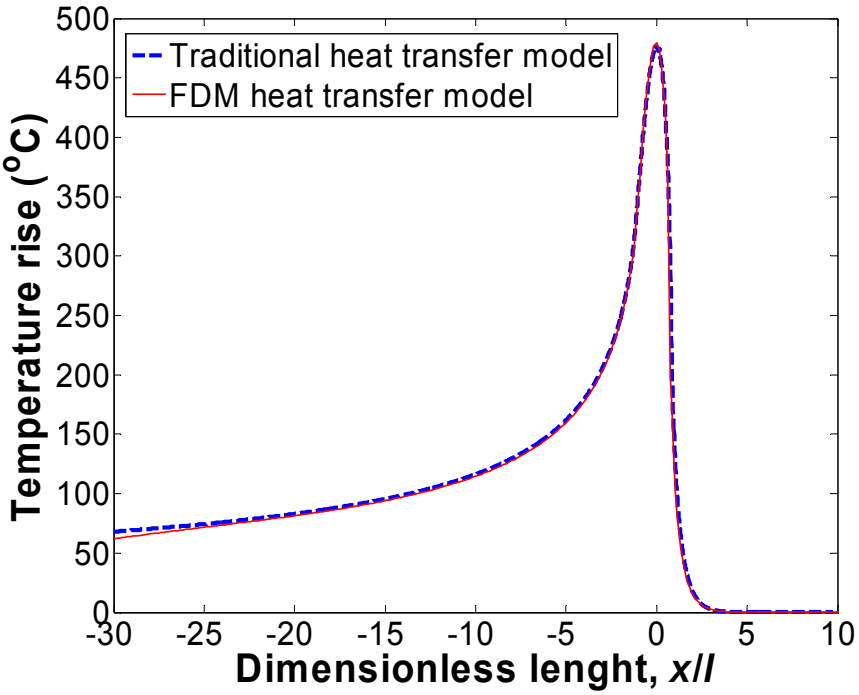

Comparison of steady-state surface temperature profile

The temperature rise in the z-direction from the FDM model is also compared to the result from the traditional heat transfer model, as shown in Figure 5.6. Again, very good match of the two curves with less than 5°C discrepancy is evident and further validated the FDM heat transfer model developed in this study.

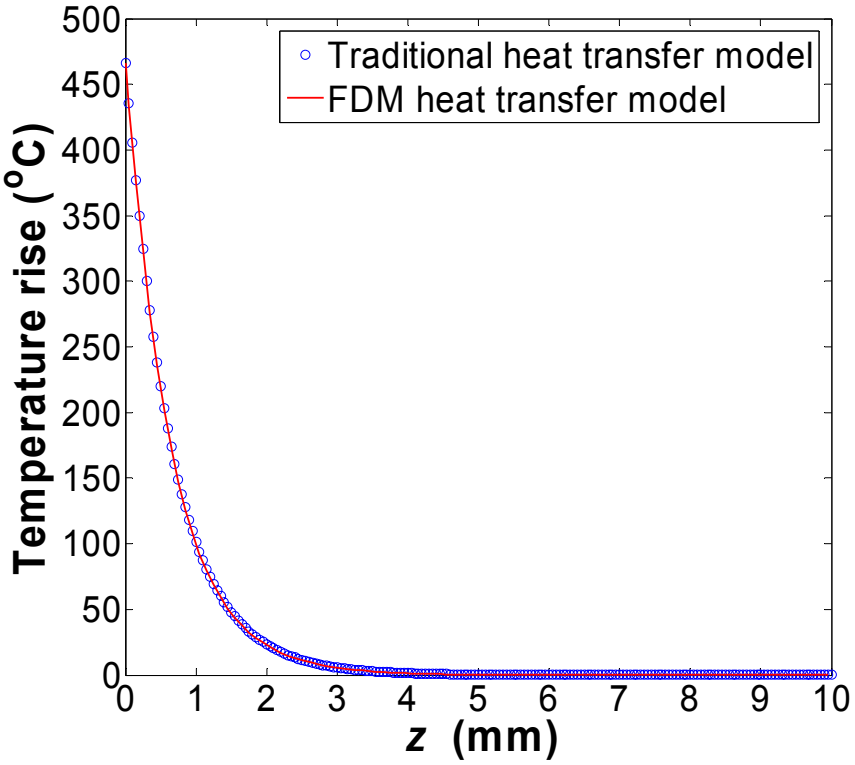

Figure 5.6. Comparison of temperature rise along the z-direction (at *x*/*l*=0)

5.4. Effects of Workpiece Dimension and Workpiece Velocity

5.4.1. Effect of Workpiece Length

As discussed in the previous session, when the workpiece is long, a steady state region exists. However, if the workpiece is short, the whole process would become a transient heat transfer problem. An example when the length of the workpiece in Sec. 3 is shortened to 5 mm (same thickness H = 10 mm) is shown in Figure 5.7. The peak temperature at the workpiece surface continues going up until the grinding wheel disengages with the workpiece. No steady state can be reached during the whole process.

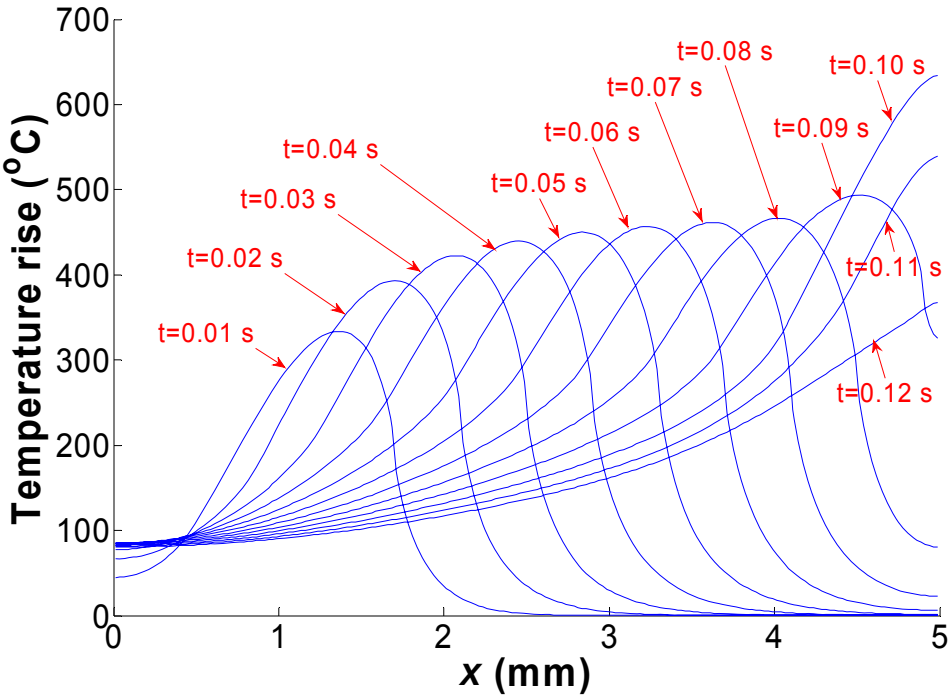

Figure 5.7. Effect of workpiece length (*L*=5 mm, *H*=10 mm, v_w=2400 mm/min)

5.4.2. Effect of Workpiece Thickness

The thickness of the workpiece mainly affects the temperature rise along the *z*-direction in the workpiece. The distribution of steady-state grinding surface temperature in the z-direction for H = 1, 2, 5, and 10 mm and L = 50 mm is shown in Figure 5.8. Compared to the traditional heat transfer model which assumes semi-infinite workpiece size, the temperature profile of H = 10 mm matches very well. When the workpiece is thick enough, H > 5 mm, the FDM solution is almost identical to the result from the traditional heat transfer model. The discrepancy starts to show when H < 2 mm. Also, the thinner workpiece has higher surface temperature because the heat cannot be dissipated efficiently in the *z*-direction.

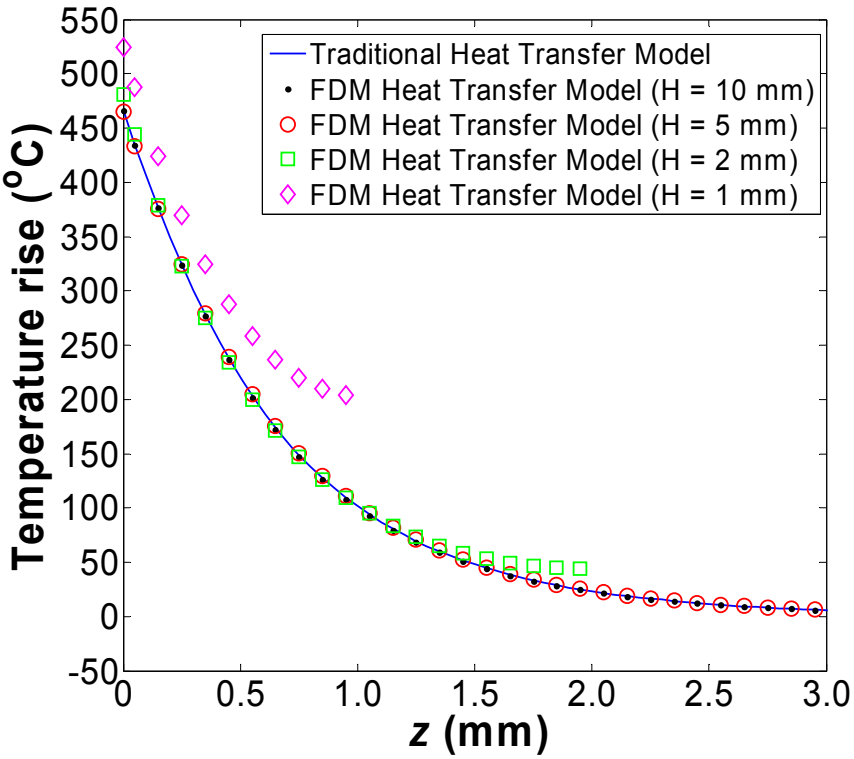

Figure 5.8. Effect of workpiece thickness (*L*=50 mm, v_w=2400 mm/min)

5.4.3. Effect of Workpiece Velocity

The workpiece velocity (feed rate) v_w has the same effect as the length of the workpiece. For example, as shown in Figure 5.9, under the same workpiece size (L = 50 mm and H = 10 mm), when v_w is small (v_w=240 mm/min), the transient heat transfer may become dominant during the whole process, and the temperature is also much higher due to the prolonged period for the heat conduction.

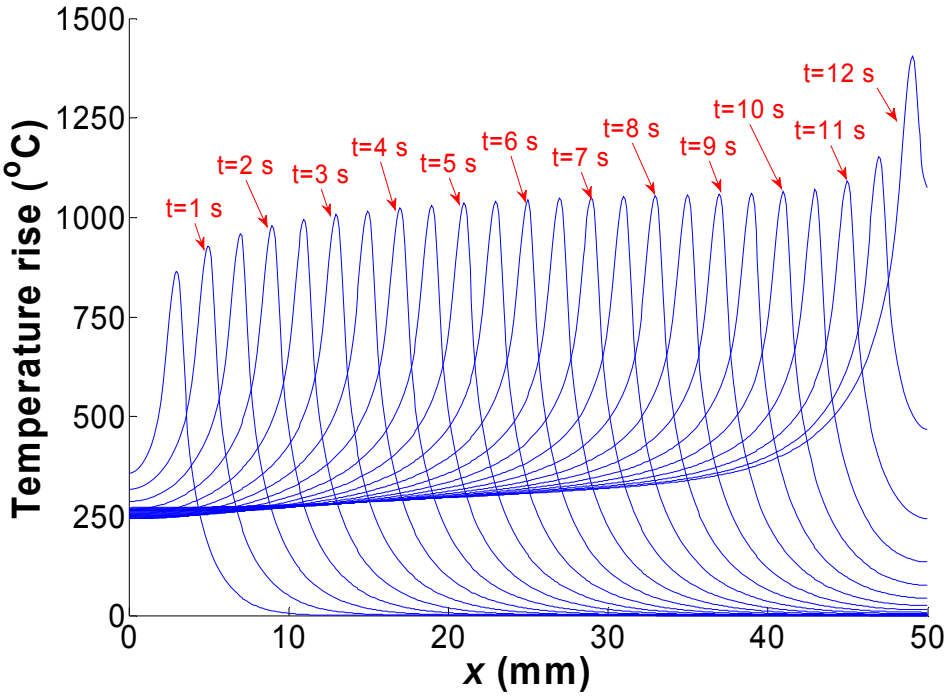

Figure 5.9. Effect of workpiece velocity (*L*=50 mm, *H*=10 mm, v_w=240 mm/min)

5.5. Cooling Effects

An advantage of FDM grinding heat transfer model is the capability to study the impact of different cooling conditions. The adiabatic surface boundary condition is assumed in the traditional heat transfer model. The practical boundary condition can be very complicated, especially when the cutting fluid is applied. In this study, the free convection and cooling in the three regions (leading edge, contact zone, and trailing edge) are analyzed and discussed in detail.

The range of heat transfer coefficient (h) for free convection is form 10 to 10^3 W/m^2-K, while for forced convection and convection with phase change ranges is from 10^2 to 10^5 W/m^2-K (Incropera and DeWitt, 2001). Jin et al. (2003) reported that the convection heat transfer coefficient within the grinding contact zone can be very high,

about 290,000 W/m^2-K for the water-based cutting fluid and 23,000 W/m^2-K for oil-based cutting fluid. In this study, h is assumed to range from 10 to 10^3 W/m^2-K for free convection condition and 10^3 to 10^5 W/m^2-K for forced convection and convection with phase change. All the other parameters used in this section are the same as in Table 5.1.

5.5.1. Free Convection

Figure 5.10 shows the steady-state surface temperature profiles for the whole surface (leading edge, contact zone, and trailing edge) under the adiabatic and free convection (h = 10, 10^2, and 10^3 W/m^2-K) boundary conditions. The results with free convection are almost identical to that with adiabatic boundary condition. This indicates that the free convection is not strong enough to influence the heat transfer in the grinding process.

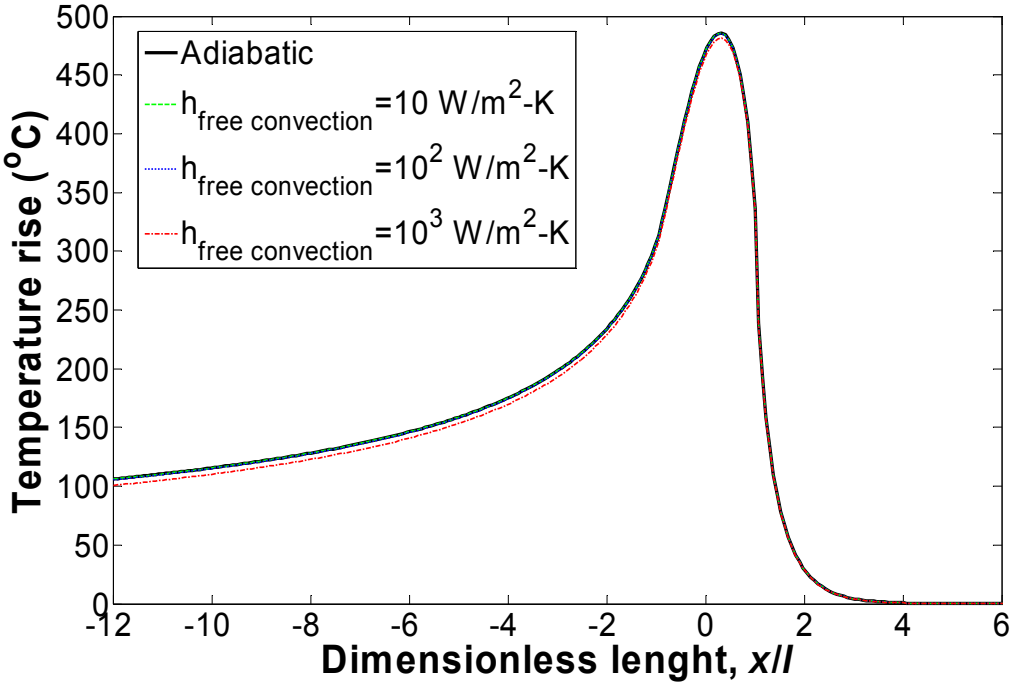

Figure 5.10. Effect of free convection (surface temperature)

5.5.2. Leading Edge

Assuming the contact zone and trailing edge is under adiabatic condition and the leading edge has h of 10^3, 10^4, and 10^5 W/m^2-K, the steady-state surface temperature profile is shown in Figure 5.11. The effect of cooling in leading edge is minimal. Under high cooling rate with h = 10^5 W/m^2-K in the leading edge, the peak temperature is reduced by only about 5%.

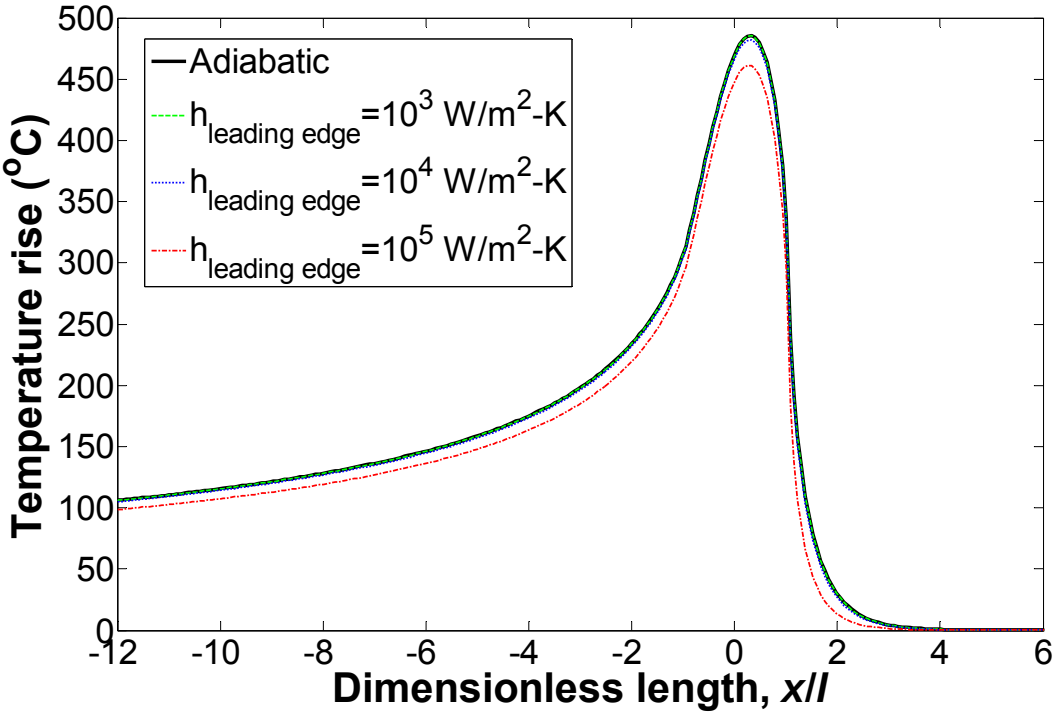

Figure 5.11. Effect of cooling in the leading edge (surface temperature)

5.5.3. Trailing Edge

By imposing the h = 10^3, 10^4, and 10^5 W/m^2-K in the trailing edge and adiabatic in the leading edge and contact zone, the steady-state workpiece surface temperature profiles is shown in Figure 5.12. Cooling in the trailing edge has a significant impact on

the temperature profile. But it only influences the trailing edge, not the contact zone or the leading edge. The peak temperature remains about the same as that with high h in trailing edge cooling.

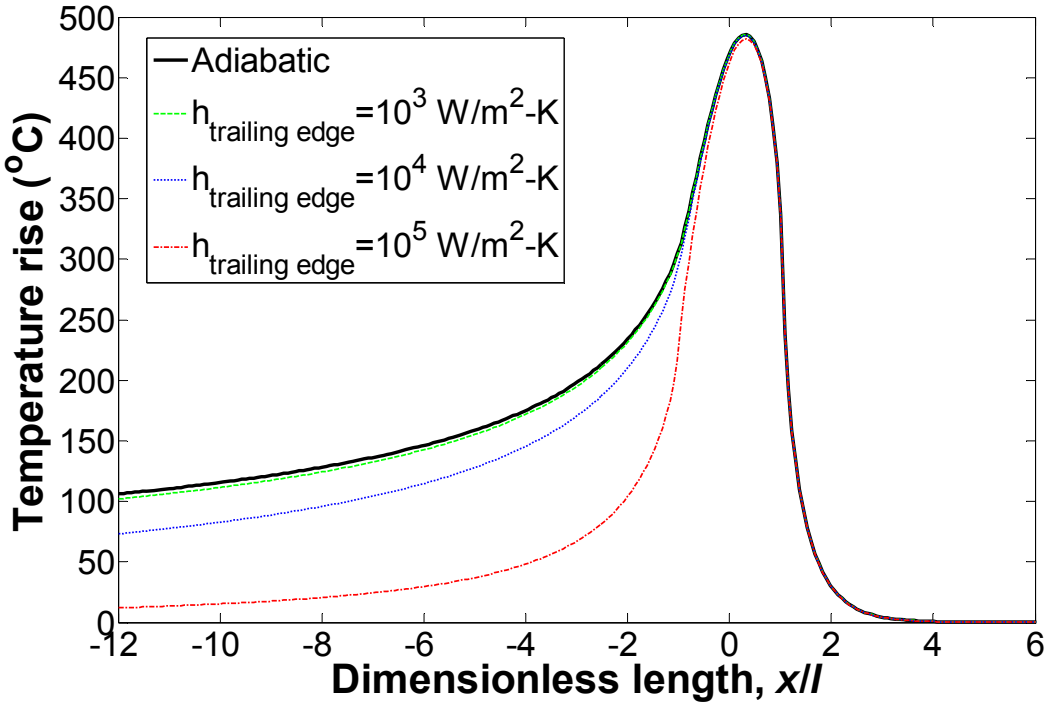

Figure 5.12. Effect of cooling in the trailing edge (surface temperature)

5.5.4. Contact Zone

For $h = 10^3$, 10^4, and 10^5 W/m^2-K in the grinding contact zone and adiabatic in the leading and trailing edges, the corresponding steady-state workpiece surface temperature profile is shown in Figure 5.13. Efficient cooling in the grinding contact zone has a significant impact on the peak temperature and trailing edge temperature. This observation confirms that the contact zone cooling is the most dominant factor in grinding.

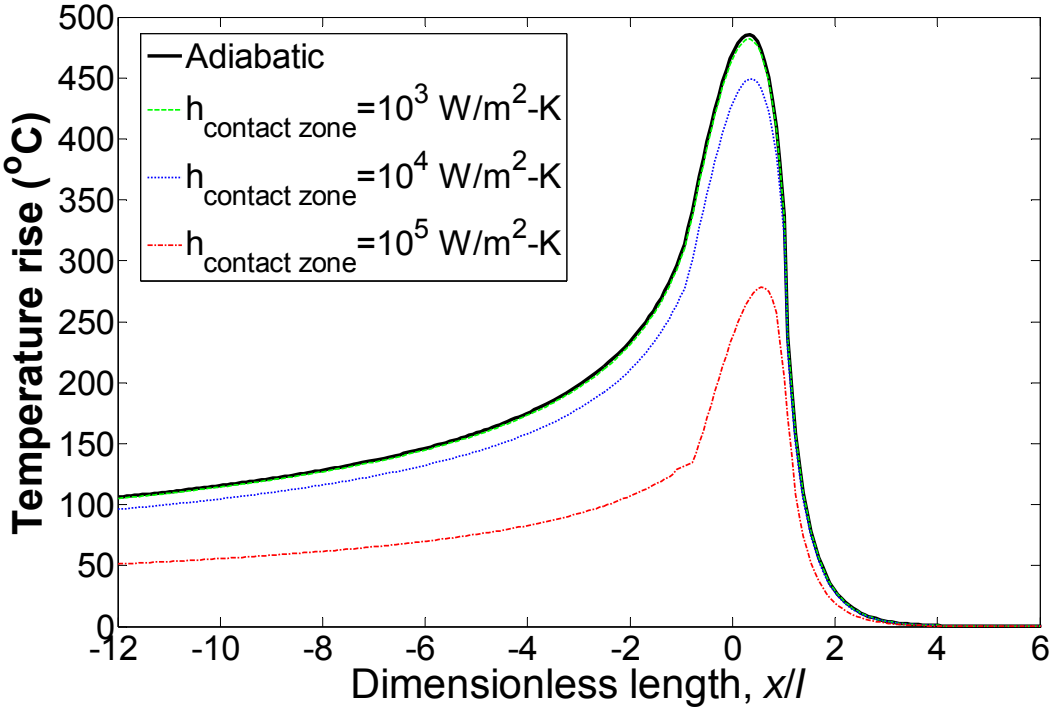

Figure 5.13. Effect of cooling in the contact zone (surface temperature)

5.6. Energy Partition Prediction

In this section, the FDM heat transfer model was used to estimate the energy partition (ratio of the energy entering the workpiece) in the real grinding application. The FDM heat transfer model traces the temporal distribution of the temperature in the workpiece, rather than only gives a steady-state solution. Therefore, the temperature response measured by the thermocouple, which is in the time domain, can be directly matched to the results calculated from the FDM heat transfer model. This makes the FDM advantageous when the grinding process is unable to reach the steady-state condition under the circumstance of short workpiece, slow v_w, and others.

According to the results in Chapter 4, the energy partition for the vitrified CBN wheel is estimated as 68% for dry grinding, 54% for MQL grinding, and 13% for wet

grinding (Shen and Shih, 2009), as summarized in Table 5.2. These values were calculated based on the traditional heat transfer model, which has already considered the cooling within the grinding zone. The reduced energy partition values in MQL and wet grinding are attributed to the convection cooling of fluids in the grinding zone. However, the traditional heat transfer model is unable to estimate the convection heat transfer coefficient in the grinding process.

Table 5.2. Grinding parameters and corresponding energy partition results

Cutting fluid application	Flowrate (ml/min)	Depth of cut (μm)	Feed rate (mm/min)	Energy partition (ε_{dry} or ε_{fluid})
Dry	--	25	2400	68.7%
MQL (soybean oil)	5			53.8%
Wet (5 vol% Cimtech 500 synthetic grinding fluid)	5400			13.2%

Inputs for the FDM heat transfer model, as presented in Section 4.3, has 177.8 mm in diameter for vitreous bond CBN grinding wheel, 30 m/s wheel surface speed (v_s), Dura-Bar 100-70-02 ductile iron work-material, 63 W/m-K thermal conductivity, 1.63×10^{-7} m^2/s thermal diffusivity, and 57 mm long, 6.5 mm wide and 20 mm tall workpiece.

The total heat flux (q_{total}) is assumed to be partitioned between the grinding wheel (q_{wheel}) and workpiece/fluid (q_{wf}).

$$q_{total} = q_{wheel} + q_{wf} = \frac{F_t v_s}{b_w l_c} \tag{5.16}$$

where F_t is the tangential grinding force and b_w is the width of the workpiece. In dry grinding, there is no heat flux carried away by the cutting fluids; therefore,

$$q_{wf} = q_{workpiece} = \varepsilon_{dry} q_{total} \tag{5.17}$$

In wet or MQL grinding, the heat flux enters both workpiece and fluids; thus,

$$q_{wf} = q_{workpiece} + q_{fluid} = \varepsilon_{fluid} q_{total} + q_{fluid} \tag{5.18}$$

where ε_{dry} and ε_{fluid} are the energy partition into the workpiece under dry and wet/MQL condition, respectively.

The energy partition values in Table 5.2 were estimated by temperature matching method using the traditional heat transfer model (Kohli et al., 1995). The same results with less than 0.1% discrepancy can also be obtained using the proposed FDM heat transfer model by imposing the adiabatic BCs, as shown in Figure 5.14. The only difference is that the temperature matching was done in the time domain instead of in the space domain.

In Figures 14(b) and (c), the deviation from the experimental measurements and FDM results is evident under the wet and MQL conditions due to the assumption of adiabatic BCs. This problem can be solved by using the appropriate boundary conditions. The FDM heat transfer model is further developed in the next section to estimate the convection heat transfer coefficient in the grinding process.

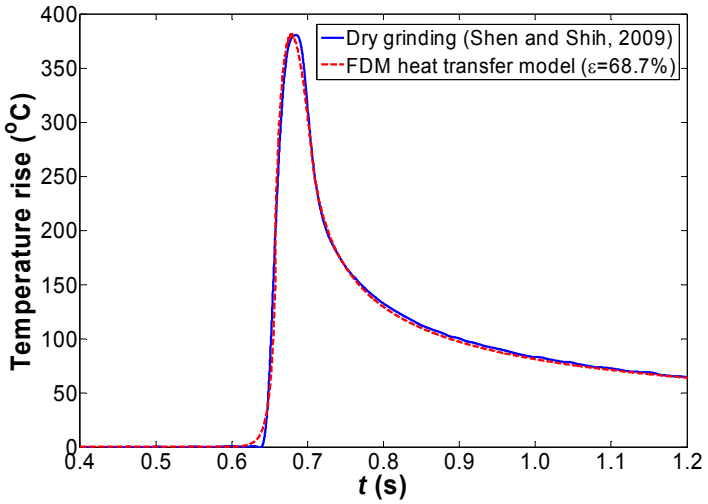

(a)

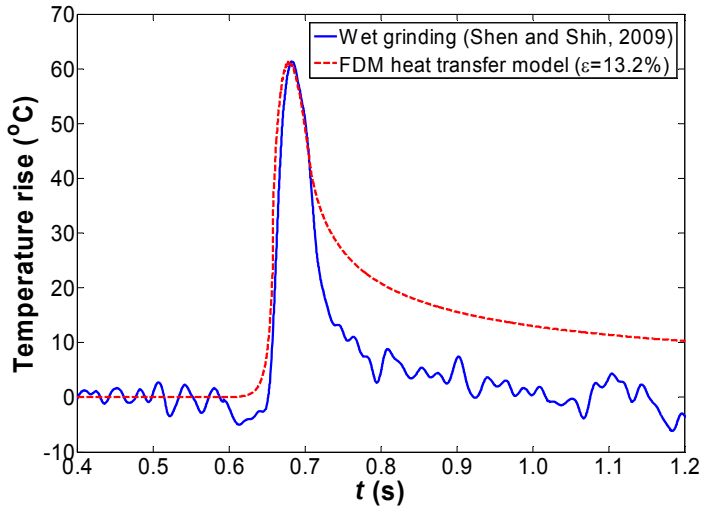

(b)

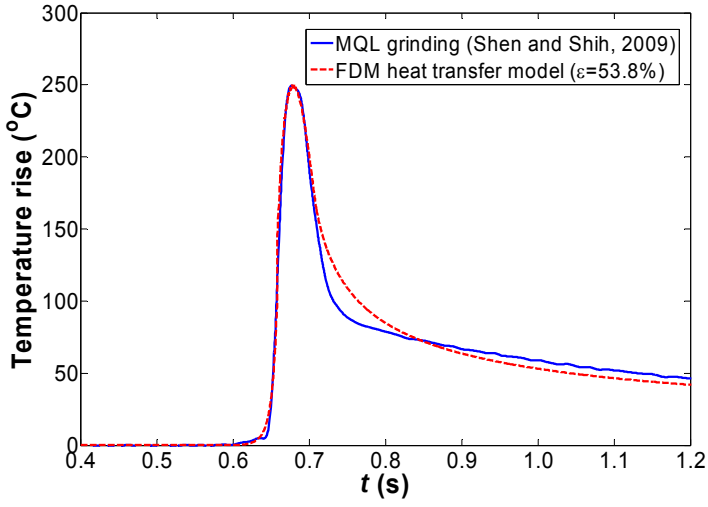

(c)

Figure 5.14. Temperature matching results: (a) dry grinding, (b) wet grinding, and (c) MQL grinding

5.7. Convection Heat Transfer Coefficient Prediction

Assuming the energy partition to the workpiece/fluid is the same in dry, wet and MQL grinding, i.e., $q_{wf} = \varepsilon_{dry} q_{total}$ regardless of the cooling condition. Thus, as long as ε_{dry} is known, the heat flux input q_{wf} for the FDM heat transfer model can be found. In addition, the heat flux into the cutting fluid can be expressed as:

$$q_{fluid} = \int_{-l}^{l} h(x)\left[T^s(x) - T_a\right]dx \tag{5.19}$$

where T_a is the fluid (or ambient) temperature.

The actual depth of cut in the grinding zone decreases from the leading edge side to the trailing edge side for down grinding. This creates the non uniform convective cooling. As shown in Figure 5.15, in this study the convection heat transfer coefficient in the grinding zone, $h_{contact}$, is assumed as a linear function.

$$h_{contact}(x) = h_1 + \frac{h_2 - h_1}{l_c}\left(x + \frac{l_c}{2}\right) \tag{5.20}$$

where $h_2 = max\left[h_{contact}(x)\right]$, $h_1 = min\left[h_{contact}(x)\right]$, and x is the local coordinate with original point at the center of the grinding zone. The average convection heat transfer coefficient in the grinding zone, $\bar{h}_{contat}$ is defined as:

$$\bar{h}_{contat} = \frac{h_1 + h_2}{2} \tag{5.21}$$

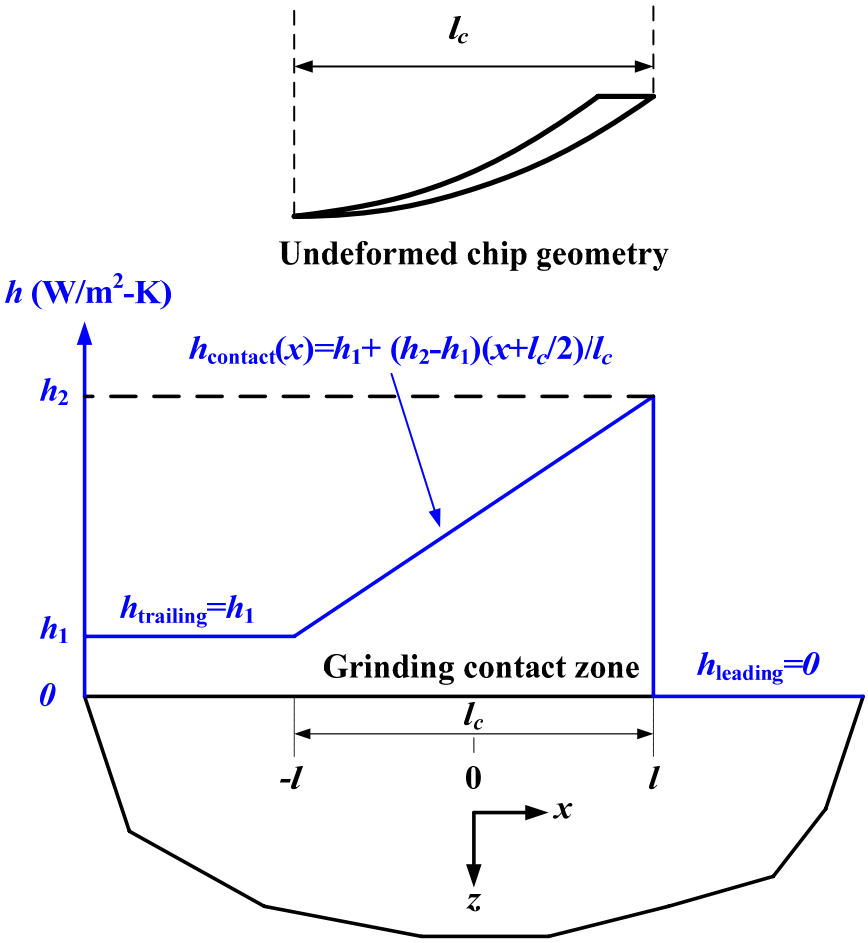

Figure 5.15. Assumption of convection heat transfer coefficient

The convection heat transfer coefficient in the trailing edge, $h_{trailing}$, is assumed to be uniform. Due to the continuity constraint, the convection heat transfer coefficient should not change rapidly between the trailing edge and the end of the contact zone at $x = -l$, where the actual depth of cut is close to zero. Therefore,

$$h_{trailing} = h_1 \tag{5.22}$$

According to Section 5, cooling effect in the leading edge is negligible. Hence $BC_{leading\_edge}$ is set to be adiabatic. The other three boundaries, BC_{back}, BC_{front}, and

BC_{bottom}, are also set to be adiabatic. A triangular heat source with an average heat flux of q_{wf} was used.

By matching the measured temperature profile to the calculated temperature from the FDM heat transfer model, the convection heat transfer coefficient within the grinding zone ($\bar{h}_{contact}$) and in the trailing edge ($h_{trailing}$) can be found. The temperature matching results are shown in Figure 5.16, and the estimated convection heat transfer coefficient values are summarized in Table 5.3. The convection heat transfer coefficient in the contact zone is much higher than that in the trailing edge for all cases. This is expected because of the much higher fluid velocity in the contact zone. Wet grinding has much higher convection heat transfer coefficient than MQL grinding both in the contact zone and the trailing edge.

Table 5.3. Summary of convection heat transfer coefficient

Cutting fluid application	h_2 (W/m^2-K)	$\bar{h}_{contact}$ (W/m^2-K)	$h_{trailing}$ (W/m^2-K)
MQL (soybean oil)	3.9×10^4	2.5×10^4	1.0×10^4
Wet (5 vol% Cimtech 500 synthetic grinding fluid)	7.4×10^5	4.2×10^5	9.5×10^4

As shown in Figure 5.16(a), for wet grinding, the uniform convection heat transfer coefficient in the trailing edge gives very good matching. However, for MQL grinding, as seen in Figure 5.16(b), the convection heat transfer coefficient in the trailing edge may not be uniform. The calculated temperature profile with a high $h_{trailing}$ matches with the experimental measurement very well in the trailing edge near the contact zone, but not in the trailing edge far away from the contact zone, while the calculated temperature profile with a zero $h_{trailing}$ has the opposite result. It indicated that MQL only provided some cooling in the trailing edge near the contact zone. This is probably due to

the low flow rate in MQL grinding which only allows a small portion of the fluid to pass through the grinding zone and cool the nearby trailing edge of the ground surface; however, in the trailing edge far away from the contact zone, MQL provides no cooling.

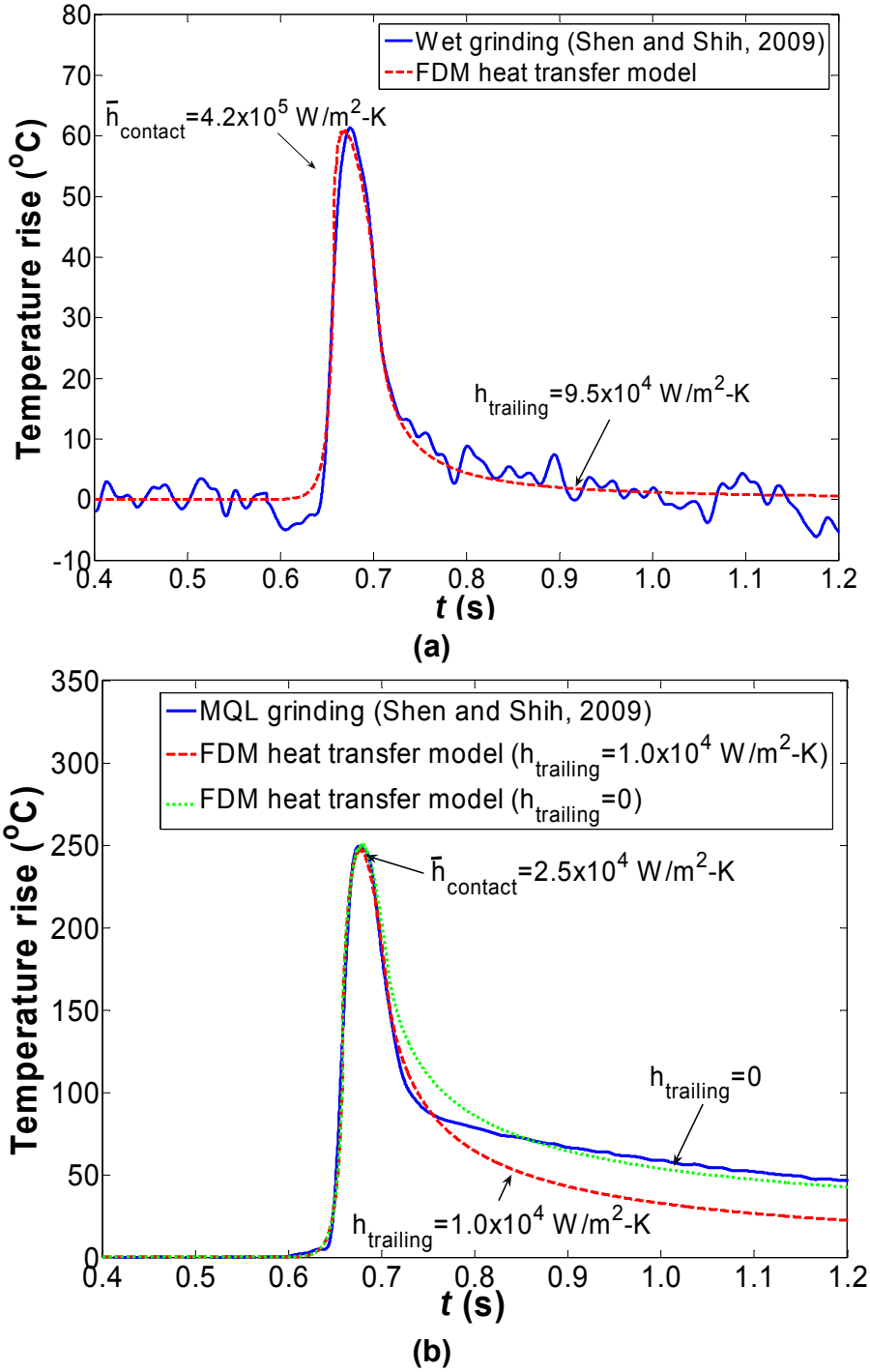

Figure 5.16. Convection heat transfer coefficient prediction: (a) wet grinding and (b) MQL grinding

5.8. Concluding Remarks

A FDM based grinding thermal model was developed and validated by comparing with the traditional heat transfer model. The FDM heat transfer model was used to study the effects of workpiece size, workpiece velocity (feed rate), and cooling in the leading edge, trailing edge and grinding zone. Transient heat transfer occurred in the cut-in and cut-out regions. When the workpiece was short or the feed rate was low, the transient effect was more significant. The thickness of the workpiece could influence the temperature profile along the *z*-direction in the workpiece. As for cooling effects, the free convection and cooling in the leading edge were neglectable; the convection heat transfer in the trailing edge could not reduce the peak temperature; and the most efficient cooling was in the grinding contact zone.

The FDM heat transfer model was further applied in the grinding experiment to estimate the energy partition and convection heat transfer coefficient. By imposing the adiabatic boundary conditions, the model was capable to estimate the same energy partition values as the traditional heat transfer model. The estimated average convection heat transfer coefficient in the grinding zone was about 4.2×10^5 W/m^2-K for wet grinding and 2.5×10^4 W/m^2-K for MQL grinding. The convection heat transfer coefficient in the trailing edge was about an order of magnitude lower than that in the grinding contact zone. However, MQL only provides some cooling in the trailing edge near the contact zone. In addition, a uniform convection heat transfer in the trailing edge may not be realistic for MQL grinding. More complicated cooling boundary conditions needs to be investigated and the FDM heat transfer model needs to be further improved.

CHAPTER 6

CONCLUSIONS AND FUTURE WORK

This research advances the fundamental research of nanofluids and the state-of-the-art MQL grinding. The formulation and characterization of nanofluids, and MQL grinding of cast iron using nanofluids were investigated. A new thermocouple fixating method for grinding temperature measurement was proposed, thermal analysis of MQL grinding was conducted, and a grinding thermal model based on the Finite Difference Method has been developed.

6.1. Major Contributions

The major contributions made in this research include:

1. The fundamental research of nanofluids was conducted. The suspension of nanoparticles has been proved to be able to enhance the thermal conductivity, especially with the high volume fraction of nanoparticles. Although the nanofluids showed higher Nusselt number than the base fluid at the same Reynolds number; in terms of convection heat transfer coefficient vs. flow rate,

there is no significant difference between the nanofluids and the base fluid.

2. The application of nanofluids in MQL grinding was evaluated for the first time. It is concluded that nanofluids are not able to provide superior cooling capacity in MQL grinding process. However, the suspension of nanoparticles can improve the tribological properties of the base fluids, which can help lubricate the grinding zone. Therefore, the research of application of nanofluids in MQL grinding should focus on the advanced lubrication properties.

3. It is shown for the first time that lubricant oils with novel MoS2 nanoparticles significantly reduces the tangential grinding force and friction between the wear flats and the workpiece, increases G-ratio and improves the overall grinding performance in MQL applications.

4. A new thermocouple fixating method was developed for grinding temperature measurement which is easy to install, and can provide a direct measurement of the surface temperature.

5. Thermal analysis for MQL grinding was studied for the first time. For shallow-cut grinding of cast iron using a vitreous bond aluminum oxide wheel, the energy partition was estimated as 84% for dry grinding, 84% for MQL grinding, but only 24% for wet grinding due to cooling within the grinding zone below the film boiling temperature.

6. Much lower energy partition to the workpiece (68% for dry grinding, 54% for MQL grinding, and 13% for wet grinding) was achieved by using vitrified bond CBN wheel. The insufficient cooling problem of MQL grinding can be improved by using the vitrified CBN wheel, which makes the MQL grinding feasible in the

high volume production.

7. A grinding thermal model has been developed based on the Finite Difference Method to better understand the transient heat transfer and temperature distributions in workpiece with finite dimension and various cooling conditions.

8. The FDM heat transfer model was applied to estimate the convection heat transfer coefficient in grinding. The average convection heat transfer coefficient in the contact zone was about 4×10^5 W/m^2-K for wet grinding and 2×10^4 W/m^2-K for MQL grinding, while the convection heat transfer coefficient in the trailing edge is much lower.

Overall, the research included the fundamental research of nanofluids, evaluation of grinding performance, measurement of grinding temperature, thermal analysis and FDM heat transfer modeling of the grinding process. It has showed that the key to the success of MQL grinding is (1) the grinding fluid with advanced tribological properties, (2) the grinding wheel with high thermal conductivity, and (3) the good understanding of cooling effects in grinding processes. The first point can be achieved by the development of new type of nanofluids which contains the nanoparticles with advanced lubricity. The second can be achieved using superabrasive grinding wheels such as CBN wheels. And the last has been addressed by the methodology developed in this study.

6.2. Recommendations for Future Study

This study has identified several future directions for the development of engineering nanofluids and MQL grinding:

The mechanism of enhanced thermal conductivity for nanofluids is still not clear. Fundamental research needs to be continued in order to better understand the involved mechanism. This is the foundation of the future nanofluids research, which can be used to guide the formulation of nanofluids for cooling application.

The mechanism of enhanced lubricating properties for nanofluids needs to be further explored. The experimental results have shown that the improvement of lubrication with lubricating nanoparticle additive could depend on the base fluid chemistry. Thus the selection of appropriate base fluid is very critical in the application of nanoparticle based lubricants in MQL grinding and requires further course of research in this field.

Based on the better understanding of nanofluids, future researches can be conducted on formulation of new nanofluids to achieve excellent tribological and thermal properties, and explore the feasible industrial application such as engine/fuel cell/radiator/ power electronics cooling and MQL machining.

It has been shown that MQL grinding using vitrified CBN wheels is very promising for the high volume grinding production. Therefore, the process needs to be further optimized.

In addition, the dimension accuracy of the ground parts has not been addressed in this study. It is another big concern for manufacturing production; especially with MQL, the accumulated heat can cause large thermal expansion of the workpiece, resulting in thermal distortion and inaccuracies. Workpiece dimension accuracy for MQL machining has already been studied (Braga et al., 2002; Furness et al., 2006; Dhar et al., 2007), but not in MQL grinding, which definitely needs more investigation.

Chip flushing seems to be a major concern for MQL grinding, resulting in undesired surface finish of ground parts. This problem has to be addressed before the MQL technology can be applied to the grinding production. One possible solution is to design a chip cleaning sub-system such as vacuum suction or high pressure air blow, as a supplement to the MQL delivery system.

The Finite Difference Method based heat transfer model developed in this research has been proved to be a simple and powerful tool to conduct the thermal analysis of the grinding process. It needed to be further improved to be more accurate and more comprehensive. For example, more complicated cooling boundary conditions and grinding zone geometry (especially for creep grinding) can be introduced into the FDM heat transfer model.

Each of these suggested future topics can be used to further enhance the understanding of nanofluids and contribute to the development of environmentally benign MQL grinding processes.

APPENDICES

Appendix A

Characterization of Nanofluids

The thermal properties of nanofluids including thermal conductivity and convection heat transfer coefficient are studied in this research.

A.1. Thermal Conductivity Measurements

A.1.1. Transient Hot Wire Method

Transient hot wire method is widely used to measure thermal conductivity of materials, especially for fluids. It was developed about thirty years ago (DeGroot et al., 1974; Castro et al., 1976; Nagasaka and Nagashima, 1981; Hoshi et al., 1981). Before that time, the thermal conductivity of fluids had historically proven to be a difficult transport property to measure accurately because the heat transfer by convection was recognized as a prominent source of error during the measurement (DeGroot et al., 1974). The most advantageous feature of the transient hot wire method for thermal conductivity measurements of fluids is its capability of experimentally eliminating convective error, and for this reason, it is a high precision technique for the measurement of the thermal conductivity of fluids (Nagasaka and Nagashima, 1981).

The theory of the transient hot wire method was developed in Carslaw and Jaeger

(1959). Based on the model of a perfectly conducting line heat source of infinite length surrounded by an infinite medium, the temperature rise of the heater wire, T, as a function of time, t, is given by (Batty et al., 1981):

$$T(t) = \frac{q}{4\pi k}\left[\ln\left(\frac{4\alpha t}{r^2}\right) - \gamma\right] \tag{A.1}$$

where r is the radius of the heater wire; q is the heat dissipated per unit length, α and k are the thermal diffusivity and thermal conductivity of the fluid to be tested; and γ is Euler's constant.

Equation (A.1) is subjected to the following assumptions:

1) The radius r of the wire is infinitesimal and the length is infinite.
2) The surrounding medium is infinite.
3) The temperature in the wire is uniform.
4) Heating period is long enough, that is, Fourier number, $F_o >> 1$, i.e.

$$F_0 = \frac{\alpha t}{r^2} >> 1 \tag{A.2}$$

The first two assumptions are hard to achieve under real engineering conditions. Thus, the effects of departures from ideal conditions on the accuracy of the thermal conductivity determinations had been studied. To avoid significant errors due to the effect of heater wire being finite, Blackwell (1954) proposed the minimum probe length to radius ratio, that is

$$\frac{L}{r} > \left(\frac{F_0}{0.0632}\right)^{1/2} \tag{A.3}$$

where L is the length of the wire.

Vos (1955) concluded that the effect of test medium being finite, i.e. the boundary effects, become significant if

$$\frac{4\alpha t}{b^2} > 0.6 \tag{A.4}$$

where b represents the shortest distance between the heater wire and the nearest boundary of the test medium.

Equation (A.1) can also be rewritten as (Batty et al., 1981):

$$\Delta T(t) = \frac{q}{4\pi k}\Delta \ln(t) \tag{A.5}$$

Therefore, the curve of temperature, T, versus time, t, on a semi-log plot is a linear line, and the slope of this line is $q/4\pi k$. Thus, if the heat flux q is known, the thermal conductivity of the test fluid can be determined experimentally by monitoring the wire temperature.

In practice, it is easy to measure the temperature of the heater wire if it is made of platinum since its resistance-temperature is well-established and measurement of resistance is much easier than measurement of temperature. For the range 0 to 630ºC, Callendar equation gives (Lowenthal and Harper, 1960):

$$R(T) = R(0)\left(1 + aT + bT^2\right) \tag{A.6}$$

where $R(T)$ is the resistance of the platinum wire at temperature, T and $R(0)$ is the resistance of the platinum wire at 0ºC; a and b are Callendar-Van Dusen coefficients.

According to ASTM Standards E 1137, a=3.9083× 10^{-3} (ºC^{-1}) and b= 5.775 × 10^{-7} (ºC^{-2}).

A.1.2. Experimental Setup

The thermal conductivity measurement apparatus, as shown in Figure A.1, was built based on transient hot wire method described in Section A.1.1. Two hot platinum wire probes, 76 μm in diameter, were developed. One probe is made of a long wire (200 mm long), as shown in Figure A.1(a) and the other probe has a short platinum wire (20 mm long), as shown in Figure A.1(b). The short wire probe is particularly suitable to test nanofluids because only a small amount of fluid is required. Both platinum wires are coated with thin Teflon film for electrical insulation. As shown in Figure A.1(c), the hot wire probe is inserted in a tube with inner diameter of 22.1 mm. The tube is filled with test fluid so that the platinum wire is submerged. The required volume of test fluid is approximately 250 and 25 ml for long and short wire probe respectively. The hot wire probe is then connected in the circuit which consists of a DC power supply and a Wheatstone bridge. All the data are collected by a PC based data acquisition system at 100 Hz. As shown in the schematic drawing Figure A.2, the platinum wire is heated by DC current passing through the wire. Meanwhile this heat flows into the surrounding fluid. The wire resistance increases as its temperature rises (the resistance of the platinum wire at room temperature was measured to be 5.08 and 0.54 Ω for long and short wire respectively). The Wheatstone bridge is used to determine the resistance of the platinum wire, which is converted to the temperature of the platinum wire using Equation (A.6). Thus the thermal conductivity of the surrounding fluid can be determined using Equation (A.5).

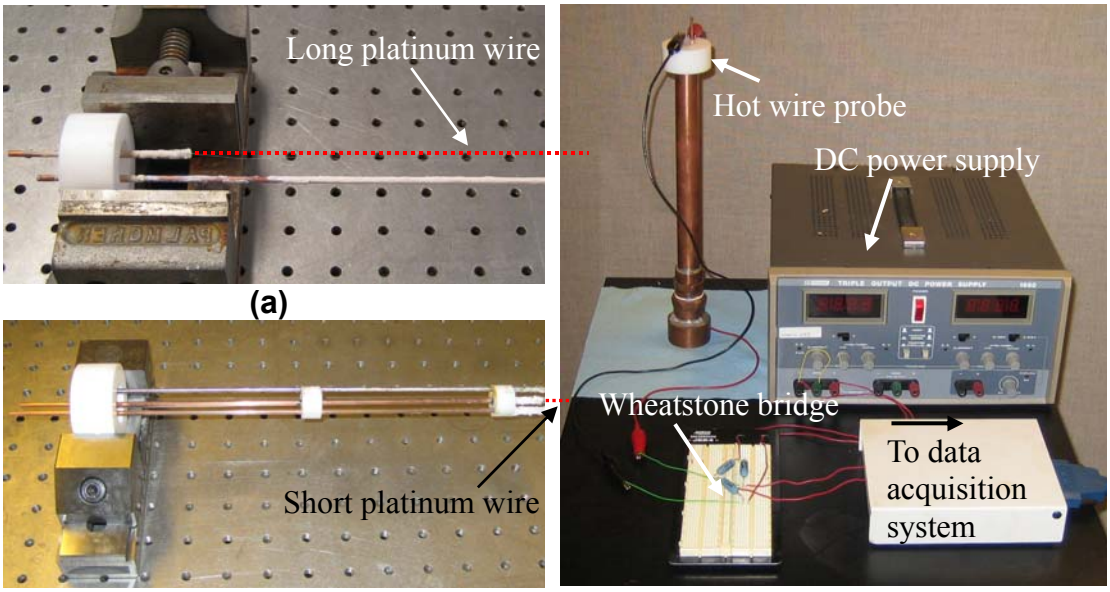

Figure A.1. Thermal conductivity measurement setup: (a) Long hot wire probe (200 mm wire marked by dashed line), (b) Short hot wire probe (20 mm wire marked by dashed line), and (c) Thermal conductivity measurement apparatus

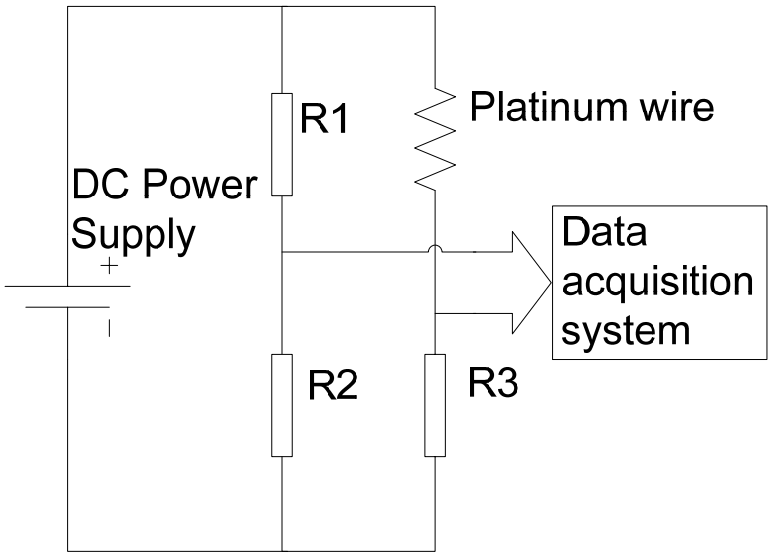

Figure A.2. Thermal conductivity measurement schematic drawing

The dimension of the apparatus was designed in such a way that all the criteria (A.2)–(A.4) are satisfied, thus the systematic errors become insignificant. The

verification of these criteria is shown in Table A.1. Here, the thermal diffusivity of water and ethylene glycol are used as they are the most common base fluid for nanofluids. Time duration of the experiment t is estimated as 30 s. The boundary b is estimated as the half inner diameter of the cylindrical tube.

Table A.1. Verification of criteria for both long and short hot wire probes (r = 38 μm, t = 30 s, b = 11.05 mm)

Criteria	Parameter	Long hot wire probe		Short hot wire probe	
	L (mm)	200		20	
	$\alpha \times 10^6$ (m^2/s)	93.9 (1)	14.9 (1)	93.9	14.9
$F_0 = \frac{\alpha t}{r^2} >> 1$	F_o	1951	3098	1951	3098
$\frac{L}{r} > \left(\frac{F_0}{0.0632}\right)^{1/2}$	$\frac{L}{r}$	5263	5263	526	526
	$\left(\frac{F_0}{0.0632}\right)^{1/2}$	176	221	176	221
Boundary effects become significant if $\frac{4\alpha t}{b^2} > 0.6$	$\frac{4\alpha t}{b^2}$	0.09	0.15	0.09	0.15

(1) Incropera and DeWitt (2001).

A.1.3. Calibration

Calibration was carried out on deionized water and ethylene glycol. The thermal conductivity of water and ethylene glycol are 0.252 and 0.606 W/m-K at room temperature (Incropera and DeWitt, 2001). Theoretically, heat dissipated per unit length q of the wire can be calculated using:

$$q = \frac{VI}{L} \tag{A.7}$$

where V is the voltage applied on the wire and I is the current passing through the wire.

Since the output voltage of the DC power supply is known, both V and I can be determined from Wheatstone bridge.

However, in reality, the platinum wire is connected to the circuit by connecting wires, therefore, there is heat loss on these connecting wires and conjunctions. Especially for short wire, this heat loss is even larger since its resistance is not that much larger than the connecting wires. Also, there is uncertainty in the measurement of wire length. Therefore, the heat dissipated per unit length q needs to be compensated when used in Equation (A.5) to determine the thermal conductivity:

$$q = \eta \frac{VI}{L} \tag{A.8}$$

where η is determined by matching the measured thermal conductivity of water with the literature value, which is 66% and 79% for short wire and long wire probe respectively. To justify the accuracy of the apparatus, the thermal conductivity of ethylene glycol was then measured, and it is in good agreement with literature value.

Sample data plot for ethylene glycol measured by both long and short wire probe are shown in Figure A.3. Clearly, there exist linear relationship between temperature and the logarithmic time within certain time interval. The departure from the linear line at the end is because of the convection heat transfer effect. Also, it is obvious that the short wire probe responds much faster than the long wire probe. A segment of data was chosen such that the linearity is guaranteed within the selected region. This segment of data was later used for linear fit in order to calculate the thermal conductivity. The corresponding calculated thermal conductivity results for different selected time interval are also shown in Figure A.3. It is clear that the later time interval gives a little higher value due to the

growing convection effect, but this difference is considerably small. To avoid both the instability of the circuit right after switch-on and the severe convection effects, the time interval of 3 to 6 (s) for long wire and 0.5 to 2 (s) for short wire are used for future calculation. Thus, the measured thermal conductivity of ethylene glycol is 0.2519 and 0.2518 for long and short respectively. Obviously, both long and short wire probes can give accurate results compared with the reference data — thermal conductivity of ethylene glycol at room temperature is 0.252 W/m-K (Incropera and DeWitt, 2001).

A.2. Convection Heat Transfer Coefficient Measurements

A.2.1. Principle

For internal flow in a tube with constant surface heat flux q, as shown in Figure A.4, the mean temperature of the fluid $T_f(x)$ varies linearly with the axial distance from the entrance x (Incropera and DeWitt, 2001):

$$T_f(x) = T_{in} + \frac{qS}{\rho c_p Q} x \tag{A.9}$$

where T_{in} is the fluid temperature at the inlet, S is the surface perimeter, ρ, c_p, Q are the density, specific heat capacity, and flowrate of the fluid, respectively.

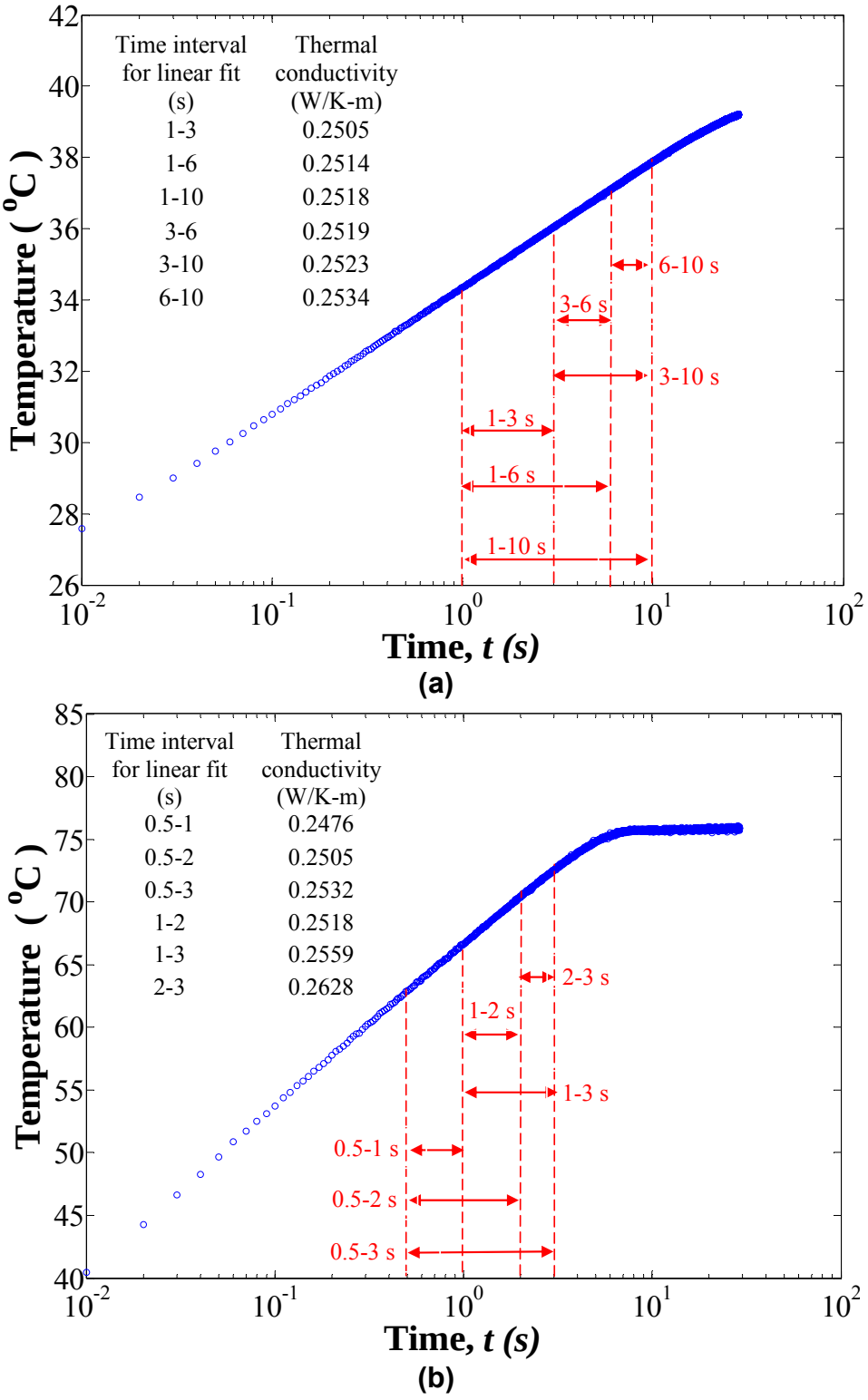

Figure A.3. Sample thermal conductivity measurement data for ethylene glycol: (a) sample data measured by the long wire probe and (b) Sample data measured by the short wire probe

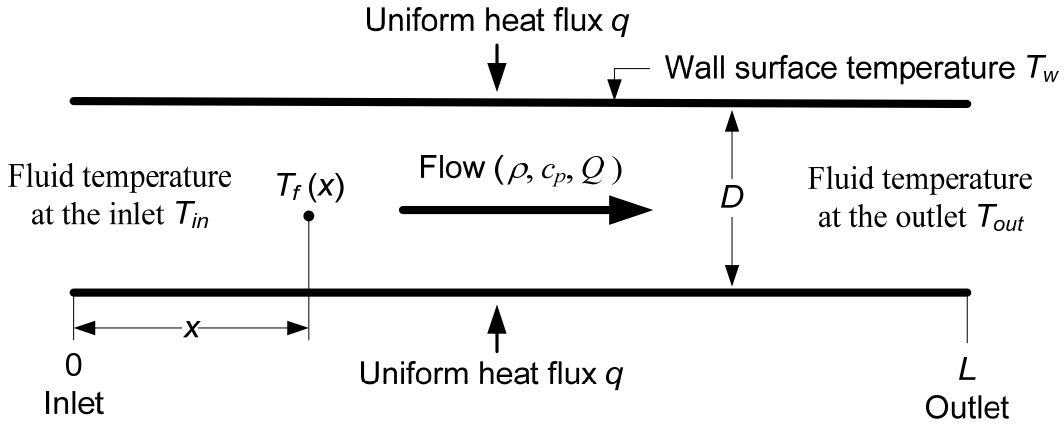

Figure A.4. Internal flow in a tube

In addition, the conservation of energy gives:

$$q = \frac{\rho c_p Q(T_{out} - T_{in})}{SL} \tag{A.10}$$

where T_{out} is the fluid temperature at the outlet, L is the length of the tube. The heat flux q can be solved by measuring the fluid temperature at both inlet and outlet (T_{in} and T_{out}).

The local convection heat transfer coefficient is defined as:

$$h(x) = \frac{q}{T_w(x) - T_f(x)} \tag{A.11}$$

where $T_w(x)$ is the wall temperature at location x. The dimensionless convection heat transfer coefficient, Nussult number, is defined as:

$$Nu = \frac{hD}{k} \tag{A.12}$$

where D is the tube diameter and k is the fluid thermal conductivity.

A.2.2. Experimental Setup

The schematic drawing and experimental setup of heat transfer coefficient measurement design are shown in Figure A.5. The testing section consists of a stainless steel tube with a diameter of 0.83 mm and a length of 304.8 mm which is considered as a micro-size channel.

The flow loop is driven by a peristaltic pump (Newport FPU5-MT-N). A filter is placed before the test section in order to avoid clogging. The test section consists of a metallic tube, a heating element, and temperature sensors. The insulation for the two setups are different because of the tubing size. The micro tube is placed inside a Teflon pipe filled with fiberglass, while the regular tube is insulated by two layers of ceramic insulation strips. Two T-type thermocouples are placed at the entrance and the exit of the test section to measure the flow inlet and outlet temperature. Five T-type thermocouples are evenly positioned along the tube to measure the wall temperature. The metallic tube is heated by the DC power supply (BK Precision 1692, Test Equipment Depot) when the fluid is passing through, and hence the forced convection heat transfer occurs. The outlet fluid is then cooled by a flow-through chiller (VWR 1106), which is turned on and off periodically by a temperature controller (Omega CN8592) in order to maintain the fluid at the temperature before it enters the test section again. The wall temperatures and the fluid temperatures at inlet and outlet are recorded after the system reaches a steady.

The volumetric flowrate was estimated by measuring the volume of fluid transported per unit time. The heat loss δ can be estimated using:

$$\delta = 1 - \frac{q_{tot}}{P} = 1 - \frac{\rho c_p Q(T_{out} - T_{in})}{VI} \tag{A.13}$$

where P is the input power of the DC power supply ($P = VI$), q_{tot} represents the total heat entering the flow, $q_{tot} = \rho c_p Q(T_{out} - T_{in})$, V and I are the output voltage and current of the DC power supply, respectively. The heat loss in the experiments is about 5% in the current setup.

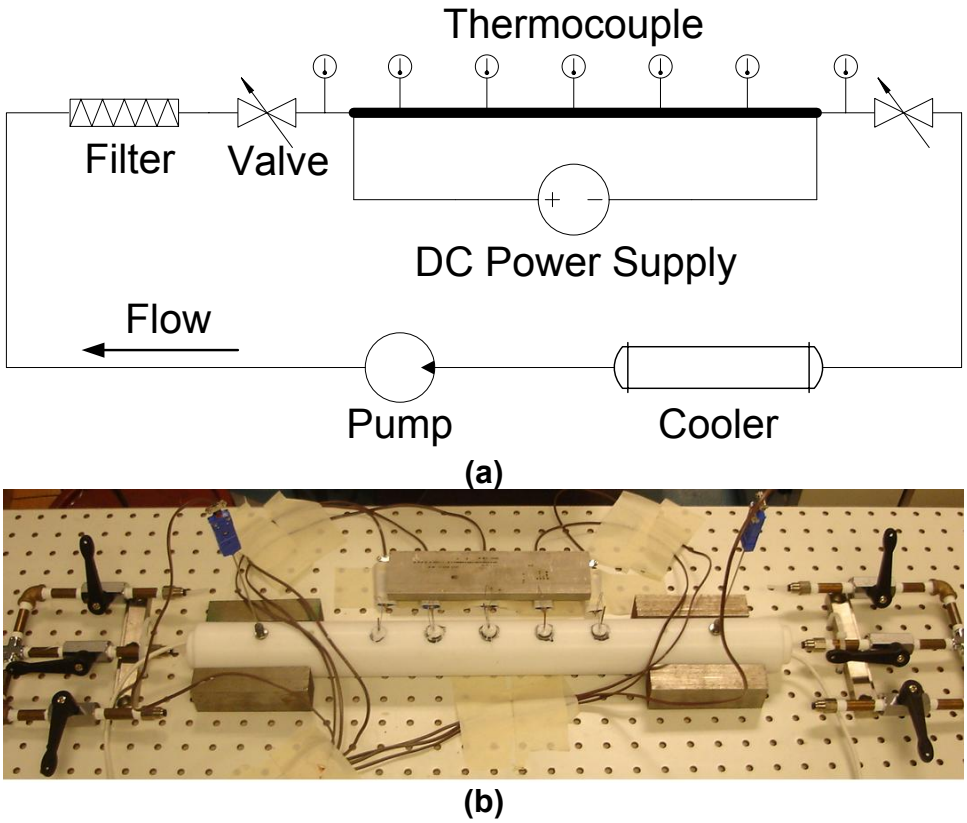

Figure A.5. Convection heat transfer measurement apparatus: (a) convection heat transfer measurement schematic drawing and (b) experimental setup

A.2.3. Calibration Results

The calibration tests were conducted on pure water and the tested flow rate ranged from 110 to 410 ml/min, which corresponds to Reynolds number of 3,600 to 14,000. The Reynolds number is a dimensionless number, defined as

$$Re = \frac{UD}{\nu} \tag{A.14}$$

where U is the mean velocity of the fluid, D is the tube diameter, and ν is the kinematic viscosity. Since the critical Reynolds number corresponding to the onset of turbulence is 2,300 (Incropera and DeWitt, 2001), the tests for microchannel setup were conducted in the turbulent regime.

Many correlations have been well-established for heat transfer flow such as Hausen correlation and Shah correlation for laminar flow, Dittus-Boelter correlation and Gnielinski correlation for turbulent flow (Incropera and DeWitt, 2001), but the convective heat transfer behavior of flow in microchannels is still controversial. Morini (2004) presented a detailed review of single-phase convective heat transfer in microchannels and most of the experimental research work being reviewed does not match well with the conventional theory. Some of those research works were conducted in the circular cross-section microchannels (Bucci et al., 2003; Tso and Mahulikar, 2000; Choi et al., 1991; Yu et al., 1995; Adams et al., 1998; Celata et al., 2000; Kandlikar et al., 2001). Among these, only Bucci et al. (2003) reported that experimentally measured Nusselt number agrees with the conventional theory. Tso and Mahulikar (2000) reported that the measured Nusselt number is lower than the prediction of conventional theory. All the other researches (Choi et al., 1991; Yu et al., 1995; Adams et al., 1998; Celata et al., 2000; Kandlikar et al., 2001) showed that the Nusselt number is larger than that predicted by conventional theory. Choi et al. (1991), Yu et al. (1995) and Adams et al. (1998) also proposed correlations for convection heat transfer of flow in microchannels. To verify our experimental setup and methodology, we will compare our experimental

results with their correlations as well as the conventional theory. Those convection heat transfer correlations will be first introduced in the following:

Choi et al. (1991) studied the friction factors, inner wall surface roughness, and convective heat transfer coefficients for flow of nitrogen gas in microtubes ranging from 3 – 81 μm in both laminar and turbulent regimes, and proposed correlations:

$$Nu = 0.000972\,\mathrm{Re}^{1.17}\,\mathrm{Pr}^{1/3} \qquad (\mathrm{Re} < 2{,}000) \tag{A.15}$$

$$Nu = 3.82\times10^{-6}\,\mathrm{Re}^{1.96}\,\mathrm{Pr}^{1/3} \qquad (2{,}500 < \mathrm{Re} < 20{,}000) \tag{A.16}$$

where Pr is Prandtl number, defined as: $\mathrm{Pr} = \dfrac{\text{kinematic viscosity, } \upsilon}{\text{thermal diffusivity, } \alpha}$

Yu et al. (1995) studied the fluid flow and heat transfer characteristics of dry nitrogen gas and water in microtubes, with diameters of 19, 52, and 102 μm , for Re ranging from 250 to over 20,000, and proposed a correlation:

$$Nu = 0.007\,\mathrm{Re}^{1.2}\,\mathrm{Pr}^{0.2} \qquad (6{,}000 < \mathrm{Re} < 20{,}000) \tag{A.17}$$

Adams et al. (1998) studied turbulent, single-phase forced convection of water in circular microchannels with diameters of 0.76 and 1.09 mm, and modified the Gnielinski correlation to accommodate the small diameters encountered in microchannels:

$$\begin{aligned} Nu &= Nu_{Gn}\left(1+F\right) \\ F &= 7.6\times10^{-5}\,\mathrm{Re}\left(1-\left(\frac{D}{1.164}\right)^{2}\right) \end{aligned} \tag{A.18}$$

for the range of conditions: $1.53 \le \mathrm{Pr} \le 6.43$; $2{,}600 \le \mathrm{Re} \le 23{,}000$; and $0.102\,\mathrm{mm} \le D \le 1.09\,\mathrm{mm}$. where Nu_{Gn} is given by Gnielinski equation (Incropera and

DeWitt, 2001), which is the well-known correlation for Nusselt number in turbulent regime:

$$Nu_{Gn} \frac{(f/8)(\mathrm{Re}-1000)\mathrm{Pr}}{1+12.7(f/8)^{1/2}(\mathrm{Pr}^{2/3}-1)} \qquad (A.19)$$
$$f = (0.790\ln \mathrm{Re}-1.64)^{-2}$$

for $2300 \le Re \le 5\times 10^6$ and $0.5 \le \mathrm{Pr} \le 200$.

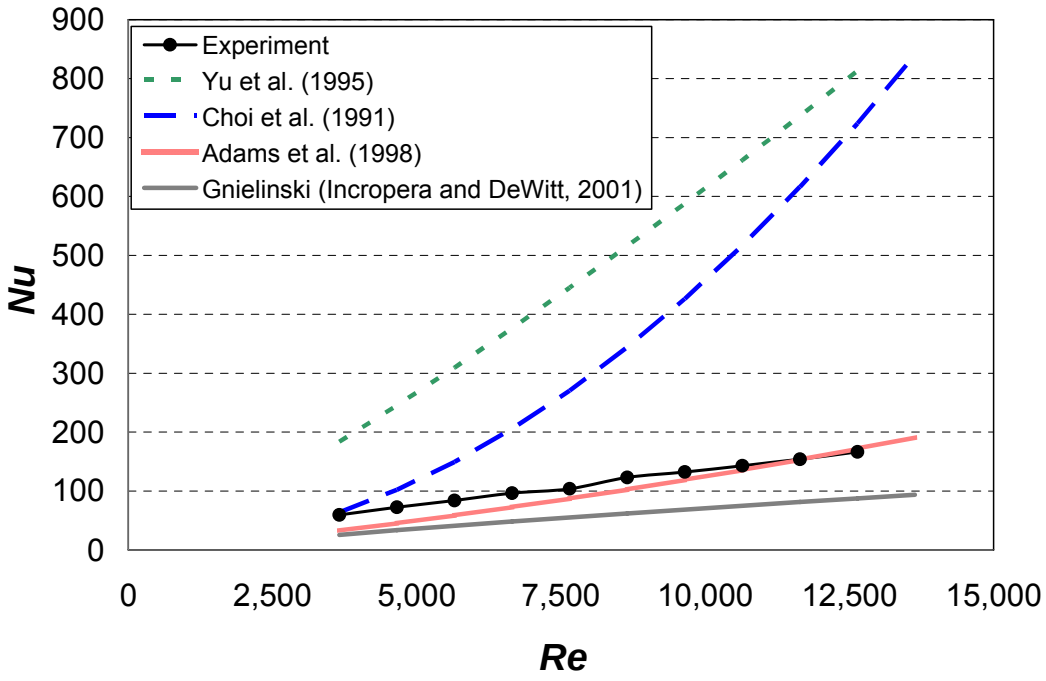

Figure A.6. Microchannel setup calibration

The calibration results for microchannels are shown in Figure A.6. The measured Nusselt number falls between the correlations in the literature. However, our experimental results also indicted that the convection heat transfer coefficient in microchannels is larger than that predicted by conventional theory (Gnielinski equation). But they are very close to Adams correlation, this is most likely because the diameter of

our microchannel setup (0.83mm) is very close to that in Adams' experiment (0.76 and 1.09 mm). Overall, the calibration results demonstrated that the current experimental setup is capable to measure the convection heat transfer coefficient of fluids in the microchannels.

Appendix B

Finite Difference Method Heat Transfer Modeling

B.1. Boundary Conditions

For the boundary condition within the grinding zone, as shown in Figure B-1, by considering the heat conduction between the nodes, heat flux from the wheel-workpiece interface, as well as the forced convection or convection with phase change within the grinding zone, the energy conservation gives:

$$q_{(m-1,1)\to(m,1)} + q_{(m+1,1)\to(m,1)} + q_{(m,2)\to(m,1)} + q'' A = \rho c_p V_o \frac{\partial T}{\partial t} + G_{contact} A\left[T_{m,1}(t) - T_a\right] \qquad \text{(B.1)}$$

where ρ, C_p are the density and the specific heat capacity of workpiece, T_a the fluid (or ambient) temperature; $V_o = \Delta x \bullet \Delta z \bullet 1$; $A = \Delta x \bullet 1$; and G_{contact} is the combined heat transfer coefficient, defined as:

$$G_{contact} = \left(\frac{1}{h_{contact}} + \frac{\Delta z}{2k} \right)^{-1} \qquad \text{(B.2)}$$

where $h_{contact}$ is the convection heat transfer coefficient within the contact zone, and k is the thermal conductivity of the workpiece. The heat flux terms can be expressed as:

$$q_{(m-1,1)\to(m,1)} = k(\Delta z \bullet 1)\left[\frac{T_{m-1,1}(t) - T_{m,1}(t)}{\Delta x}\right] \tag{B.3}$$

$$q_{(m+1,1)\to(m,1)} = k(\Delta z \bullet 1)\left[\frac{T_{m+1,1}(t) - T_{m,1}(t)}{\Delta x}\right] \tag{B.4}$$

$$q_{(m,2)\to(m,1)} = k(\Delta x \bullet 1)\left[\frac{T_{m,2}(t) - T_{m,1}(t)}{\Delta z}\right] \tag{B.5}$$

Equation (B.1) can be rewritten as:

$$\begin{aligned} T_{m,1}(t+\Delta t) &= \frac{(\Delta x)^2}{\alpha \Delta t}\left[T_{m-1,1}(t) + T_{m+1,1}(t) + T_{m,2}(t) + \frac{G_{contact}\Delta x}{k}T_a\right] \\ &+ \left[1 - 3\frac{(\Delta x)^2}{\alpha \Delta t} - \frac{(\Delta x)^2}{\alpha \Delta t}\frac{G_{contact}\Delta x}{k}\right]T_{m,1}(t) + \frac{(\Delta x)^2}{\alpha \Delta t}\frac{q''\Delta x}{k} \end{aligned} \tag{B.6}$$

For the BC in the region of leading edge, there is no heat flux; therefore, the $BC_{leading\_edge}$ can be derived by modifying Equation (B.6):

$$\begin{aligned} T_{m,1}(t+\Delta t) &= \frac{(\Delta x)^2}{\alpha \Delta t}\left[T_{m-1,1}(t) + T_{m+1,1}(t) + T_{m,2}(t) + \frac{G_{leading}\Delta x}{k}T_a\right] \\ &+ \left[1 - 3\frac{(\Delta x)^2}{\alpha \Delta t} - \frac{(\Delta x)^2}{\alpha \Delta t}\frac{G_{leading}\Delta x}{k}\right]T_{m,1}(t) \end{aligned} \tag{B.7}$$

where $G_{leading} = \left(\frac{1}{h_{leading}} + \frac{\Delta z}{2k}\right)^{-1}$ and $h_{leading}$ is the convection heat transfer coefficient in the leading edge.

All the other boundary conditions ($BC_{trailing\_edge}$, BC_{back}, BC_{front}, and BC_{bottom}) are very similar to Equation (B.7). Note that, if the adiabatic boundary is imposed, all the

BCs will still hold by simply setting the convection heat transfer coefficient ($h_{contact}$, $h_{leading}$, $h_{trailing}$, h_{front}, or h_{back}) to zero.

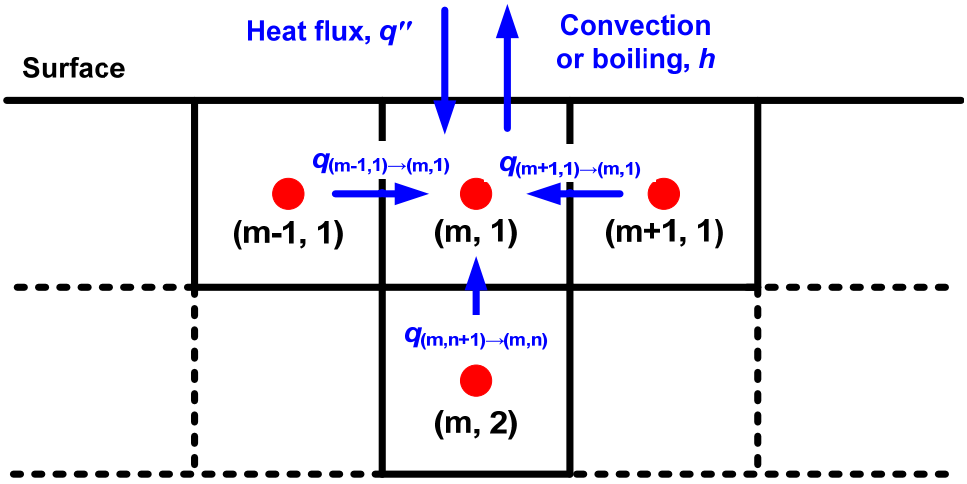

Figure B.1. BC within the contact zone

B.2. Surface Temperature

As seen in Figure B.2, the energy conversation at the surface (within the contact zone) gives:

$$q''\,A = q_{surface\to(m,1)} + h_{contact}\,A\left[Ts_{m,1}(t) - T_a\right] \tag{B.8}$$

$$q''(\Delta x \bullet 1) = k(\Delta x \bullet 1)\left[\frac{T^s_{m,1}(t) - T_{m,1}(t)}{\Delta z/2}\right] + h_{contact}(\Delta x \bullet 1)\left[T^s_{m,1}(t) - T_a\right] \tag{B.9}$$

$$T^s_{m,1}(t) = \frac{q''\Delta z/k + 2T_{m,1}(t) + h_{contact}\Delta z T_a/k}{\left(2 + h_{contact}\Delta z/k\right)} \tag{B.10}$$

Similarly, the surface temperature in the region of leading and trailing edges can be expressed as following, respectively.

$$T_{m,1}^{s}(t)=\frac{2T_{m,1}(t)+h_{leading}\Delta z T_a / k}{\left(2+h_{leading}\Delta z / k\right)} \tag{B.11}$$

$$T_{m,1}^{s}(t)=\frac{2T_{m,1}(t)+h_{trailing}\Delta z T_a / k_a}{\left(2+h_{trailing}\Delta z / k\right)} \tag{B.12}$$

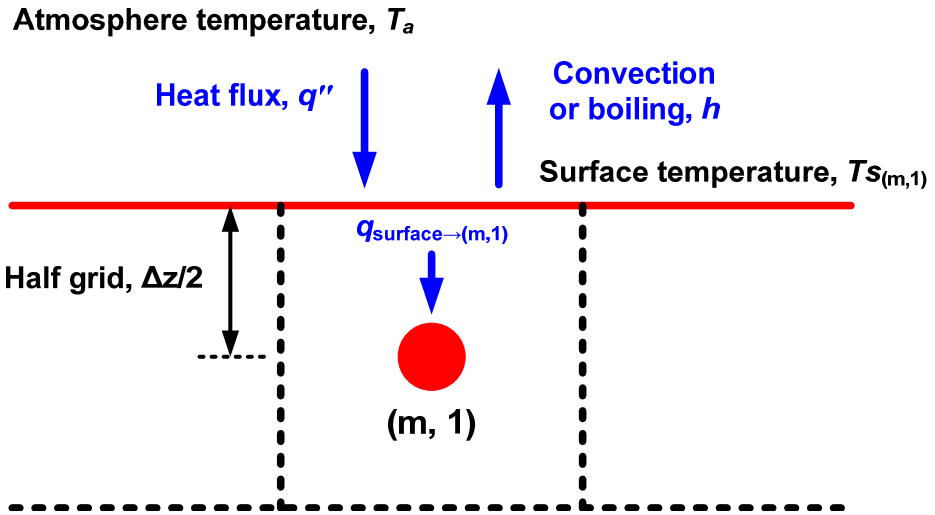

Figure B.2. Interpretation of the surface temperature (contact zone)

BIBLIOGRAPHY

Bibliography

Adams, T.M., Abdel-Khalik S.I., Jeter S.M., and Qureshi Z.H., 1998, "An experimental investigation of single-phase forced convection in microchannels," International Journal of Heat and Mass Transfer, vol. 41, pp. 851–857.

Assael, M.J., Chen, C.F., Metaxa, I., Wakeham, and W.A., 2004, "Thermal conductivity of suspensions of carbon nanotubes in water," International Journal of Thermophysics, vol. 25, no. 4, pp. 971-985.

Autret, R., and Liang, S.Y., 2003, "Minimum quantity lubrication in finish hard turning," HNICEM '03.

Baheti, U., Guo, C., and Malkin, S., 1998, "Environmentally conscious cooling and lubrication for grinding," Proceedings of the International Seminar on Improving Machine Tool Performance, vol. 2, pp. 643-654.

Batty, W.J., O'Callaghan, P.W., and Probert, S.D., 1984, "Assessment of the thermal-probe technique for rapid, accurate measurements of effective thermal conductivities," Applied Energy, vol. 16, pp. 83-113.

Baheti, U., Guo, C., and Malkin, S., 1998, "Environmentally conscious cooling and lubrication for grinding," Proceedings of the International Seminar on Improving Machine Tool Performance, vol. 2, pp. 643-654.

Batako, A.D., Rowe, W.B., and Morgan, M.N., 2005, "Temperature measurement in high efficiency deep grinding," Int. J. Machine Tools Manuf., vol. 45, pp.1231-1245.

Biermann, D. and Schneider, M., 1997, "Modeling and simulation of workpiece temperature in grinding by finite element analysis," Machining Science and Technology, vol. 1, no. 2, pp. 173-183.

Blackwell, J.H., 1954. "A transient-flow method for determination of thermal constants of insulating materials in bulk," J. Appl. Phys., vol. 25, no. 2, pp.137–144.

Braga, D.U., Diniz, A.E., Miranda, G.W.A., and Coppini, N.L., 2002, "Using a minimum quantity of lubricant (MQL) and a diamond coated tool in the drilling of aluminum-silicon alloys," Journal of Materials Processing Technology, vol. 122, no. 1, pp. 127-138.

Brinksmeier, E., Brockhoff, T., and Walter, A., 1997, "Minimalmengenkühlschmierung und Trockenbearbeitung beim Schleifen," Haerterei-Technische Mitteilungen, vol. 52, pp. 166-170.

Bucci, A., Celata, G.P., Cumo, M., Serra, E., and Zummo, G., 2003, "Fluid flow and single-phase flow heat transfer of water in capillary tubes," Proceedings of the Int. Conference on Minichannels and Microchannels, Rochester, USA, paper ICMM-1037.

Carslaw, H.S., and Jaeger, J.C., 1959, Conduction of heat in solids, 2nd Edition, Clarendon Press., Oxford, pp. 169 -170.

Castro, C.A.N, Calado, J.C.G, Wakeham, W.A, and Dix, M., 1976, "An apparatus to measure the thermal conductivity of liquids," J Phys E Sci Instrum, vol. 9, pp. 1073-1080.

Celata, G.P., Cumo, M., Guglielmi, M., and Zummo G., 2000, "Experimental investigation of hydraulic and single phase heat transfer in 0.130 mm capillary tube," Proceedings of International Conference on Heat Transfer and Transport Phenomena in Microscale," Begell House, New York, USA, pp. 108–113.

Che, J.W., Cagin, T., Goddard, W.A., 2000, "Thermal conductivity of carbon nanotubes," Nanotechnology, vol. 11, pp. 65-69.

Chen, Z., Yamaguchi, H., and Liang, S.Y., 2002a, "Predictive modeling of cutting fluid aerosol in grinding process," Transactions of the North American Manufacturing Research Institution, Society of Manufacturing Engineers, pp. 277-285.

Chen, Z., Liang S.Y., and Yamaguchi, H., 2002b, "Predictive modeling of cutting fluid aerosol generation in cylindrical grinding," Society of Manufacturing Engineers, vol. 160, pp. 1-8.

Choi, S.B., Barron, R.F., and Warrington, R.O., 1991, "Fluid flow and heat transfer in microtubes," Micromechanical Sensors, Actuators and Systems, ASME DSC, vol. 32, Atlanta, GA, pp. 123–134.

Choi, S.U.S., 1995, "Enhancing thermal conductivity of fluids with nanoparticles," Proceedings of the 1995 ASME International Mechanical Engineering Congress

and Exposition, San Francisco, CA, USA.

Choi, S.U.S., Li, S., Yu, W., and Thompson, L.J., 2001a, "Anomalously increased effective thermal conductivities of ethylene glycol-based nanofluids containing copper nanoparticles," Applied Physics Letters, vol. 78, no. 6, pp. 718-720.

Choi, S.U.S., Zhang, Z.G., Yu, W., Lockwood, F.E, and Grulke, E.A., 2001b, "Anomalous thermal conductivity enhancement in nanotube suspensions," Applied Physics Letters, vol. 79, pp. 2252-2254.

Choi, S.U.S., and Eastman, J.A., 2001, "Enhanced heat transfer using nanofluids," US Patent Number 6,221,275.

Curry, A.C., Shih, A.J., Scattergood, R.O., Kong, J., and McSpadden, S.B., 2003, "Grinding temperature measurements in MgO PSZ using infrared spectrometry," J. Am. Ceram. Soc., vol. 86, pp. 333-341.

Das, S.K., Putra, N., Thiesen, R., and Roetzel, W., 2003, "Temperature dependence of thermal conductivity enhancement for nanofluids," Journal of Heat Transfer, vol. 125, no. 4, pp. 567-574.

Davim, J.P., Sreejith, P.S., Gomes, R., and Peixoto, C., 2006, "Experimental studies on drilling of aluminum (AA1050) under dry, minimum quantity of lubricant, and flood-lubricated conditions," J. Engineering Manufacture, vol. 220, pp. 1605-1611.

Davim, J.P., Sreejith, P.S. and Silva, J., 2007, "Turning of brasses using minimum quantity of lubricant and flooded lubricant conditions," Materials and Manufacturing Processes, vol. 22, pp. 45-50.

DeGroot, J.J, J. Kestin, and H. Sookiazian, 1974, "Instrument to measure the thermal conductivity of gases," Physica, vol. 75, pp. 454-482.

Demetriou, M.D., and Lavine, A.S., 2000, "Thermal aspects of grinding, the case of upgrinding," J. Manuf. Sci. Eng., vol. 122, pp. 605-611.

DesRuisseaux, N.R., and Zerkle, R.D., 1970, "Thermal analysis of the grinding process," ASME J. Eng. Ind., vol. 92, pp. 428-434.

Dhar, N.R., Islam, M.W., Islam, S., and Mithu, M.A.H., 2006, "The influence of minimum quantity of lubrication (MQL) on cutting temperature, chip and dimensional accuracy in turning AISI-1040 steel," Journal of Materials Processing Technology, vol. 171, pp. 93-99.

Dhar, N.R., Ahmed, M.T., and Islam, S., 2007, "An experimental investigation on effect of minimum quantity lubrication in machining AISI 1040 steel," International Journal of Machine Tools and Manufacture, vol. 47, no. 5, pp. 748-753.

Eastman, J.A., Choi, S.U.S., Li S., Thompson L.J., and Lee S., 1997, "Enhanced thermal conductivity through development of nanofluids," Materials II, ed. S Komarnenl, JC Parker, HJ Wollenberger, pp. 3. Pittsburgh: Materials Research Society.

Eastman, JA, Choi, S.U.S., Li, S., Yu, W., and Thompson, L.J., 2001, "Anomalously increased effective thermal conductivity of ethylene glycol-based nanofluids containing copper nanoparticles," Applied Physics Letters, vol. 78, no. 6, pp. 718-720.

Eastman, J.A., Phillpot, S.R., Choi, S.U.S., Keblinski, P., 2004, "Thermal transport in nanofluids," Annual Review of Materials Research, vol. 34, pp. 219-246.

Filipovic, A., and Stephenson, D.A., 2006, "Minimum quantity lubrication applications in automotive power-train machining," Machining Science and Technology, vol. no. 10, pp. 3-22.

Florescu, D.I., Mourokh, L.G., Pollak, F.H., Look, D.C. , Cantwell, G., Li, X., 2002, "High spatial resolution thermal conductivity of bulk ZnO," Journal of Applied Physics, vol. 91, no.2, pp. 890-892.

Fuh, K.H., and Huang, J.S., 1994, "Thermal analysis of creep-feed grinding," J. Materials Proc. Technology, vol. 43, pp. 109-124.

Furness, R., Stoll, A., Nordstrom, G.. Martini, G., Johnson, J., Loch, T., and Klosinski, R., 2006, "Minimum Quantity Lubrication (MQL) machining for complex powertrain components," Proceedings of the International Conference on Manufacturing Science and Engineering.

Guo, C., and Malkin, S., 1992, "Heat transfer in grinding," J. Materials Proc. Manuf. Sci., vol. 1, pp. 16-27.

Guo, C., Wu, Y., Varghese, V., and Malkin, S., 1999, ''Temperatures and energy partition for grinding with vitrified CBN wheels,'' CIRP Annals, vol. 48, pp. 247-250.

Guo, C., and Malkin, S., 1995a, "Analysis of energy partition in grinding," Journal of Engineering for Industry, vol.117, pp. 55–61.

Guo, C. and Malkin, S., 1995b, "Analysis of transient temperatures in grinding," Journal of Engineering for Industry, vol. 117, pp. 571-577.

Guo, C., and Malkin, S., 1996a, "Inverse heat transfer analysis of grinding, part 1: Methods," Journal of Engineering for Industry, vol. 118, no. 1, pp. 137-142.

Guo, C., and Malkin, S., 1996b, "Inverse heat transfer analysis of grinding, part 2: Applications," Journal of Engineering for Industry, vol. 118, no. 1, pp. 143-149.

Hafenbraedl, D., and Malkin, S., 2000, "Environmentally-conscious minimum quantity lubrication (MQL) for internal cylindrical grinding," Transactions of NAMRI/SME, vol. 28, pp. 149-154.

Hahn, R.S., 1956, "The relation between grinding conditions and thermal damage in the workpiece ," Transactions of the ASME, vol. 78, pp. 807-812.

Hahn. R.S., 1962, "On the nature of the grinding process," Proceedings of the 3rd Machine Tool Design and Research Conference, pp. 129-154.

Hahn R S., 1966, "On the mechanics of the grinding process under plunge cut conditions," Journal of Engineering for Industry, vol. 88, pp. 72-80.

Hamilton, R.L. and Crosser, O. K., 1962, "Thermal conductivity of heterogeneous two-component systems," I&EC Fundamentals, vol. 1, no. 3, pp. 187-191.

Heinemann, R., Hinduja, S., Barrow, G., and Petuelli, G., 2006, "Effect of MQL on the tool life of small twist drills in deep-hole drilling," International Journal of Machine Tools and Manufacture, vol. 46, pp. 1-6.

Hong, K.K. and Lo, C.Y., 2000, "Inverse analysis for the heat conduction during a grinding process," Journal of Materials Processing Technology, vol. 105, no. 1, pp. 87-94.

Hong, T.K., Yang, H.S., and Choi, C.J., 2005, "Study of the enhanced thermal conductivity of Fe nanofluids," J. Appl. Phys., vol. 97, 64311.

Hoshi, M., Omotani, T., and Nagashima, A., 1981, "Transient method to measure the thermal conductivity of high-temperature melts using a liquid-metal probe," Review of Scientific Instruments, vol. 52, no. 5, pp. 755-758.

Huang, H., and Xu, X.P., 2004, "Interfacial interactions between diamond disk and granite during vertical spindle grinding," Wear, vol. 256, pp. 623-629.

Hwang, J., Kompella, Sridhar, S., Chandrasekar, S., and Farris, T.N., 2003, "Measurement of temperature field in surface grinding using Infra-Red (IR) imaging system," J. Tribology, vol. 125, pp. 377-383.

Incropera, F.P. and DeWitt, D.P., 2001, Fundamentals of Heat and Mass Transfer, 5th Edition, Wiley.

Itoigawa, F., Childs, T.H.C., Nakamura, T., and Belluco, W., 2006, “Effects and mechanisms in minimal quantity lubrication machining of an aluminum alloy," Wear, vol. 260, no. 3, pp. 339-344.

Jaeger, J.C., 1942, “Moving sources of heat and the temperature at sliding contacts,” Journal of the Royal Society of New South Wales, vol. 76, pp. 203–224.

Jang S.P. and Choi S.U.S., 2004, “Role of Brownian motion in the enhanced thermal conductivity of nanofluid,” Appl. Phys. Lett., vol. 84, no. 21, pp. 4316–4318.

Jeffrey, D.J., 1973, “Conduction through a random suspension of spheres,” Proceedings of the Royal Society of London, Series A, vol. 335, no. 1602, pp. 355–367.

Jen, T.C. and Lavine, A.S., 1995, “A variable heat flux model of heat transfer in grinding: model development,” Journal of Heat Transfer, vol. 117, no. 2, pp. 473-478.

Ju, Y., Farris, T.N., and Chandrasekar, S., 1998, “Theoretical analysis of heat partition and temperatures in grinding,” Journal of Tribology, vol. 120, no. 4, pp. 789-794.

Kamata, Y., and Obikawa, T., 2007, “High speed MQL finish-turning of Inconel 718 with different coated tools,” Journal of Materials Prorcessing Technology, vol. 192, pp. 281-286.

Kandlikar, S.G., Joshi, S., and Tian, S., 2001, “Effect of channel roughness on heat transfer and fluid flow characteristics at low Reynolds numbers in small diameter tubes,” Proc. of 35th National Heat Transfer Conference, Anaheim CA, USA, paper 12134.

Keblinski, P., Phillpot, S.R., Choi, S.U.S., and Eastman J.A., 2002, “Mechanisms of heat flow in suspensions of nano-sized particles (nanofluids),” International Journal of Heat and Mass Transfer, vol. 45, no. 4, pp. 855-863.

Kim, H.J., Kim, N.K., and Kwak, J.S., 2006, “Heat flux distribution model by sequential algorithm of inverse heat transfer for determining workpiece temperature in creep feed grinding,” International Journal of Machine Tools and Manufacture, vol. 46, no. 15, pp. 2086-2093.

Klocke, F., and Eisenblatter, G., 1997, “Dry cutting,” Annals of the CIRP, vol. 46, pp. 519-526.

Kobayashi, S., Ohgoe, Y., Ozeki, K., Sato, K., Sumiya, T., Hirakuri, K.K., and Aoki, H., 2005, "Diamond-like carbon coatings on orthodontic archwire," Diamond and Related Materials, vol. 14, pp. 1094-1097.

Kohli, S. P., Guo, C., and Malkin, S., 1995, ''Energy partition for grinding with aluminum oxide and CBN abrasive wheels,'' Journal of Engineering for Industry, vol. 117, pp. 160–168.

Komanduri, R., and Reed, W.R., 1980, "New technique of dressing and conditioning resin bonded superabrasive grinding wheels," Annals of the CIRP, vol. 29, no. 1, pp. 239-243.

Lavine, A.S., 1988, "A simple model for convective cooling during the grinding process," Journal of Engineering for Industry, vol. 110, pp. 1-6.

Lavine, A.S., Malkin, S., and Jen, T., 1989, ''Thermal Aspects of Grinding with CBN," CIRP Ann., vol. 38, pp. 557–560.

Lee, S., Choi, S.U.S., Li, S., and Eastman, J.A., 1999, "Measuring thermal conductivity of fluids containing oxide nanoparticles," ASME Journal of Heat Transfer, vol. 121, no. 2, pp. 280-289.

Lefebvre, A., Vieville, P., Lipinski, P., and Lescalier, C., 2006, "Numerical analysis of grinding temperature measurement by the foil/workpiece thermocouple method," International Journal of Machine Tools and Manufacture, vol. 46, no. 14, pp. 1716-1726.

Liao, Y.S., Luo, S.Y. and Yang, T.H., 2000, "Thermal model of the wet grinding process," Journal of Materials Processing Technology, vol. 101, no. 1, pp. 137-145.

Liao, Y.S., and Lin, H.M., 2007, "Mechanism of minimum quantity lubrication in high-speed milling of hardened steel," International Journal of Machine Tools and Manufacture, vol. 47, pp. 1660-1666.

Littman, W.E., and Wulff, J., 1995, "The influence of the grinding process on structure of hardened steels," Trans. Am. Soc. Metals, vol. 47, pp. 692.

Lockwood, F.E., Zhang, Z.G., Forbus, T.R., Choi, S.U.S., Yang, Y., and Grulke, E.A., 2005, "The current development on nanofluid research," SAE 2005 World Congress & Exhibition, Detroit, MI, USA, Session: Military Vehicle Fuels, Lubes and Water.

Lopez de Lacalle, L.N., Angulo, C., Lamikiz, A., and Sanchez, J.A., 2006, "Experimental

and numerical investigation of the effect of spray cutting fluids in high speed milling," Journal of Materials Processing Technology, vol. 172, pp. 11-15.

Lowenthal, G.C. and Harper, A.F.A., 1960, "Resistance-temperature relationship of platinum at low temperatures and its influence on precision thermometry," J. Appl. Phys., vol. 11, pp. 205-208.

Machado, A. R., and Wallbank, J., 1997, "Effect of extremely low lubricant volumes inachining," Wear, vol. 210, pp. 76-82.

Mahdi, M. and Zhang L., 1995, "The finite element thermal analysis of grinding processes by ADINA," Computer and Structure, vol. 56, pp. 313–320.

Maksoud, T.M.A., 2005, "Heat transfer model for creep-feed grinding," Journal of Materials Processing Technology, vol. 168, no. 3, pp. 448-463.

Malkin, S., and Anderson, R.B., 1974, "Thermal aspects of grinding. Part 1 - Energy Partition," ASME J. Eng. Ind., vol. 96, pp. 1177-1183.

Malkin S., 1984, "Grinding of metals: theory and application," Journal of Applied Metalworking, America Society for Metals, vol. 3, no. 2, pp. 95-109.

Malkin, S., 1989, Grinding Technology: Theory and Applications of Machining with Abrasives, Ellis Horwood Ltd, Chichester, and John Wiley & Sons, New York.

Malshe, A.P., and Verma, A., 2006, "Nanoparticle compositions and methods for making and using the same," International Application No. PCT/US07/60506.

Mamalis, A.G., Kundrak, J., Manolakos, D.E., Gyani, K., and Markopoulos, A., 2003, "Thermal modelling of surface grinding using implicit finite element techniques," International Journal of Advanced Manufacturing Technology, vol. 21, no. 12, pp. 929-934.

Masuda, H., Ebata, A., Teramae, K., and Hishinuma, N., 1993, "Alteration of thermal conductivity and viscosity of liquid by dispersing ultra-fine particles (dispersion of γ -Al_2O_3, SiO_2 and TiO_2 ultra-fine particles)," Netsu Bussei, vol.4, pp. 227-233.

Maxwell, J.C., 1904, A Treatise on Electricity and Magnetism, 2nd ed. Oxford University Press, Cambridge, U.K., 1904, pp. 435–441.

Morini, G.L., 2004, "Single-phase convective heat transfer in microchannels: A Review of Experimental Results," Int. J. Therm. Sci., vol. 43, pp. 631–651.

Murshed, S.M.S., Leong, K.C., and Yang, C., 2005, "Enhanced thermal conductivity of TiO_2 - water based nanofluids," International Journal of Thermal Sciences, vol. 44, pp. 367-373.

Nagasaka, Y, and Nagashima, A., 1981, "Absolute measurement of the thermal conductivity of electrically conducting liquids by transient hot-wire method", J Phys E Sci Instrum, 1981, vol. 14, pp. 1435-1440.

Nouari, M., List, G., Girot, F., and Coupard, D., 2003, "Experimental analysis and optimisation of tool wear in dry machining of aluminium alloys," Wear, vol. 255, pp. 1359-1368.

Outwater, J.O., and Shaw, M.C., 1952, "Surface temperatures in grinding," Trans. ASME, vol. 74, pp. 73-86.

Ozisik, M.N., 1994, Finite Difference Methods in Heat Transfer, CRC Press.

Pak, B.C., and Cho, Y.I., 1998, ''Hydrodynamic and heat transfer study of dispersed fluids with submicron metallic oxide particles,'' Exp. Heat Transfer, vol. 11, pp. 151-170.

Patel, H.E., Das, S.K., Sundararajan, T., Nair, A.S., George, B., and Pradeep, T., 2003, "Thermal conductivities of naked and monolayer protected metal nano-particle based nano-fluids: manifestation of anomalous enhancement and chemical effects," Applied Physics Letters, vol. 83, no. 14, pp. 2931-2933.

Rahman, M., Senthil Kumar, A., and Salam, M. U., 2001, "Evaluation of minimal quantities of lubricant in end milling," International Journal of Advanced Manufacturing Technology, vol. 18, no. 4, pp. 235-241.

Rahman, M., Kumar, A.S., and Salam, M.U., 2002, "Experimental evaluation on the effect of minimal quantities of lubricant in milling," International Journal of Machine Tools and Manufacture, vol. 42, no. 5, pp. 539-547.

Reddy, N.S.K., and Rao, P.V., 2006, "Selection of an optimal parametric combination for achieving a better surface finish in dry milling using genetic algorithms," International Journal of Advanced Manufacturing Technology, vol. 28, pp. 463-473.

Rowe, W.B., Pettit, J.A., Boyle, A., and Moruzzi, J.L., 1988, "Avoidance of thermal damage in grinding," Annals of CIRP, vol. 37, pp. 327-330.

Rowe, W. B., Black, S.C.E., Mills, B., Qi, H. S., Morgan, M.N, 1995, "Experimental

investigation of heat transfer in grinding," Annals of the CIRP, vol. 44, pp. 329-332.

Rowe, W.B., Black, S.C.E., and Mills, B., 1996, "Temperature control in CBN grinding," Int. J. Advanced Manuf. Technology, vol. 12, pp. 387-392.

Sakagami, T., Madhavan, V., Harish, G., Krishnamurthy, K., Ju, Y., Farris, T.N. and Chandrasekar, S., 1990, "Full-field IR measurement of subsurface grinding temperatures," Proc. of SPIE, vol. 3361, pp. 234-245.

Shaw M.C., 1990, "A simplified approach to workpiece temperature in fine grinding," CIRP. Annals, vol. 39, pp. 345-347.

Shen, C.H., 1996, "The importance of diamond coated tools for agile manufacturing and dry machining," Surface and Coating Technology, vol. 86-87, pp. 672-677.

Shen, B, Shih, A.J., and Tung, S.C., 2008a, "Application of nanofluids in minimum quantity lubrication grinding," accepted for STLE (Society of Tribologists and Lubrication Engineers) Tribology Transactions.

Shen, B., Malshe, A.P., Kalita, P., and Shih, A.J., 2008b, "Performance and behavior of novel MoS_2 nanoparticles based grinding fluids in minimum quantity lubrication grinding" accepted for NAMRI/SME, vol 36.

Shen, B., Xiao, G., Guo, C., Malkin, S., and Shih, A.J., 2009, "Thermocouple fixating method for grinding temperature measurement," submitted to ASME Journal of Manufacturing Science and Engineering.

Shen, B., and Shih, A.J., 2009, "Minimum quantity lubrication (MQL) grinding using vitrified CBN wheels," submitted to NAMRI/SME, vol. 37.

Shih, A.J., Curry A.C., Scattergood, R.O., Yonushonis, T.M., Gust, D.J., Grant, M.B., McSpadden, S.B., and Watkins, Y., 2003, "Cost-effective grinding of zirconia using the dense vitreous bond silicon carbide wheel," Journal of Manufacturing Science and Engineering, vol. 125, pp. 297-303.

Silva, L.R., Bianchi, E.C., Catai, R.E., Fusse, R.Y., and Franca, T.V., 2005, "Study on the behavior of the minimum quantity lubricant - MQL technique under different lubricating and cooling conditions when grinding ABNT 4340 steel," Journal of the Brazilian Society of Mechanical Sciences and Engineering, vol. 27, no. 2, pp. 192-199.

Su, Y.L., Liu, T.H., Su, C.T., Yao, S.H., Kao, W.H., and Cheng, K.W., 2006, "Wear of

CrC-coated carbide tools in dry machining," Journal of Materials Processing Technology, vol. 171, pp. 108-117.

Sun, J., Wong, Y.S., Rahman, M., Wang, Z.G., Neo, K.S., Tan, C.H., and Onozuka, H., 2006, "Effects of coolant supply methods and cutting conditions on tool life in end milling titanium alloy," Machining Science and Technology, vol. 10, pp. 355-370.

Takazawa, K., 1966, "Effects of grinding variables on the surface of hardened steel," Bull. Japan Soc. Prec. Eng., vol. 2, pp. 14-21.

Takazawa, K., 1972, "Thermal aspects of the grinding operation," Industrial Diamond Review, pp. 143-149.

Tso, C.P., and Mahulikar, S.P., 2000, "Experimental verification of the role of Brinkman number in microchannels using local parameters," Internat. J. Heat Mass Transfer, vol. 4, pp. 1837–1849.

Ueda, K.Y., and Sugita, T., 1992, "Measurement of grinding temperature of ceramics using infrared radiation pyrometer with optical fiber," ASME J. Eng. Ind., vol. 114, pp. 317-21.

Ueda, T., 1986, "Measurement of grinding temperature using infrared radiation pyrometer with optical fiber," ASME J. Eng. Ind., vol. 108, pp. 241-247.

Upadhyaya, R.P., and Malkin, S., 2004, "Thermal aspects of grinding with electroplated CBN wheels," ASME J. Manuf. Sci. Eng., vol. 126, pp. 107-114.

Varghese, V., Guo, C., Malkin, S., and Xiao, G., 2000, "Energy partition for grinding of nodular cast iron with vitrified CBN wheels," Mach. Sci. Technol., vol. 4, pp. 197-208.

Verma, A., Malshe, A.P., Brown, W., Jiang, W., Adhvaryu, A., and McCluskey, P., 2006, "Exploring mechanical synthesis of inorganic nanoparticles of MoS_2 lubricant and its composite with organic medium for advanced manufacturing," 4th International Symposium on Nanomanufacturing (ISNM).

Verma, A., Jiang, W., Abu-Safe, H.H., and Malshe, A.P., 2007, "Tribological behavior of the deagglomerated active inorganic nanoparticles for advanced lubrication," accepted to Tribology Transactions.

Vos, B.H., 1955, "Measurements of thermal conductivity by non-steady-state method," Appl. Sci. Res., Sec. A, vol. 5, pp. 425 - 438.

Wagener, M., Murty, B.S., Gunther, B., 1997, "Preparation of metal nanosuspensions by high-pressure DC-sputtering on running liquids," Nanocrystalline and Nanocomposite Materials II, ed. S Komarnenl, JC Parker, HJ Wollenberger, Pittsburgh: Materials Research Society., pp. 149.

Wagener, M., Gunther, B., 1999, "Sputtering in liquids: a versatile process for the production of magnetic suspensions," J. Magn. Magn. Mater., vol., 201, no. 4.

Wakabayashi, T., Sato, H., and Inasaki, I., 1998, "Turning using extremely small amounts of cutting fluids," JSME International Journal, vol. 41, pp. 143-148.

Wang, X., Xu, X., and Choi, S.U.S., 1999, "Thermal conductivity of nanoparticle-fluid mixture," J. Thermophys. Heat Transfer, vol. 13, no. 4, pp. 474–480.

Wang, C.C., and Chen, C.K., 2002, "Three-dimensional inverse heat transfer analysis during the grinding process," Journal of Mechanical Engineering Science, vol. 216, pp. 199–214.

Wang, L., Qin, Y., Liu, Z.C., Ge, P.Q., and Gao, W., 2003, "Computer simulation of a workpiece temperature field during the grinding process," Journal of Engineering Manufacture, vol. 217, no. 7, pp. 953-959.

Wen, D., and Ding, Y., 2004a, "Experimental investigation into convective heat transfer of nanofluids at the entrance region under laminar flow conditions, International Journal of Heat and Mass Transfer, vol. 47, no. 24, pp. 5181-5188.

Wen, D., and Ding, Y., 2004b, "Effective thermal conductivity of aqueous suspensions of carbon nanotubes (carbon nanotube nanofluids)," Journal of Thermophysics and Heat Transfer, vol. 18, no. 4, pp. 481-485.

White, S., 2006, GM Summer intern report.

Wu, J.H., Phillips, B.S., Jiang, W., Sanders, J.H., Zabinski, J.S., and Malshe, A.P., 2006, "Bio-inspired surface engineering and tribology of MoS_2 overcoated CBN-TiN composite coating." Wear, vol. 261, pp. 592-599.

Xie, H., Wang, J., Xi, T., Liu, Y., Ai, F. and Wu, Q., 2002a, "Thermal conductivity enhancement of suspensions containing nanosized alumina particles," J. Appl. Phys., vol. 91, pp. 4568-4572.

Xie, H., Wang, J., Xi, T., and Liu, Y., 2002b, "Thermal conductivity of suspensions containing nanosized SiC particles," Int J Thermophys, vol. 23, no. 2, pp. 571-580.

Xie, H., Lee, H., You, W., and Choi, M., 2003, "Nanofluids containing multiwalled carbon nanotubes and their enhanced thermal properties," Journal of Applied Physics, vol. 94, no. 8, pp. 4967–4971

Xu, T., Zhang, J., and Xu, K., 1996, "The ball-bearing effect of diamond nanoparticles as an oil additive," Applied Physics, vol. 29, pp. 2932-2937.

Xu, X.P., and Malkin, S., 2001, "Comparison of methods to measure grinding temperatures," ASME J. Manuf. Sci. Eng., vol. 123, pp. 191-195.

Xu, X., Yu, Y., and Huang, H., 2003, "Mechanisms of abrasive wear in the grinding of titanium (TC4) and nickel (K417) alloys," Wear, vol. 255, pp. 1421-1426.

Xuan, Y., and Roetzel, W., 2000, "Conceptions for heat transfer correlation of nanofluids," International Journal of Heat and Mass Transfer, vol. 43, no. 19, pp. 3701-3707.

Xuan, Y., and Li, Q., 2000, "Heat transfer enhancement of nanofluids," Int. J. Heat & Flow, vol. 21, no. 1, pp. 58-64.

Xuan, Y., and Li, Q., 2003, "Investigation on convective heat transfer and flow features of nanofluids," Journal of Heat Transfer, vol. 125, no.1, pp. 151-155.

Yang, Y., Zhong Z.G., Grulke E.A., Anderson W.B. and Wu G., 2005, "Heat transfer properties of nanoparticle-in-fluid dispersion (nanofluids) in laminar flow," Int. J. Heat Mass Transfer, vol. 48. pp. 1107–1116.

Yatsuya, S., Tsukasaki, Y., Mihama, K., Uyeda, R., 1978, "Preparation of extremely fine particles by vacuum evaporation onto a running oil substrate," J. Cryst. Growth, vol. 45, pp. 490-494.

Yu, D., Warrington R.O., Barron, R., and Ameel, T., 1995, "An experimental and theoretical investigation of fluid flow and heat transfer in microtubes," Proceedings of ASME/JSME Thermal Engineering Joint Conf., Maui, HI, pp. 523–530.

Zhu, H.T., Lin, Y.S., and Yin, Y.S., 2004, "A novel one-step chemical method for preparation of copper nanofluids," Journal of Colloid and Interface Science, vol. 277, no. 1, pp. 100-103.

Zhou, L.P., and Wang, B.X., 2002, "Experimental research on the thermophysical properties of nanoparticle suspensions using the quasi-steady method," Annu. Proc. Chin. Eng. Thermophys, pp. 889-892.